

Materials Development and Spectroscopic Characterisation of Solid Oxide Cells



Jevgenija Manerova

The University of Sheffield

Faculty of Engineering

Department of Chemical and Biological Engineering

This dissertation is submitted in partial fulfilment of the requirements for the degree of
Doctor of Philosophy

October 2018

To my family and friends

Declaration

This dissertation is the result of my own work and includes nothing, which is the outcome of work done in collaboration except where specifically indicated in the text. It has not been previously submitted, in part or whole, to any university or institution for any degree, diploma, or other qualification.

Jevgenija Manerova

Abstract

Solid oxide cells (SOCs) are highly efficient electrochemical energy conversion devices capable of on-demand, reversible energy conversion: chemical energy into electricity and *vice versa*. Operating at intermediate to high temperatures, SOCs have a great potential for high conversion efficiencies using a wide variety of reactants, including carbon dioxide (CO₂) and low-grade fuels such as biogas.

An enhanced understanding of the electrochemical reactions occurring at the triple phase boundary (TPB) active sites of the electrodes and the cell degradation mechanisms is critical to the development of the robust, reversible SOCs. Nickel-based electrodes, commonly used in SOCs, are susceptible to carbon deposition and poisoning by contaminants, such as sulfur and silica, causing detrimental effect on the electrochemical performance of the SOCs.

The research aims of this work were threefold. First of all, an electrochemical reactor capable of simultaneous vibrational Raman spectroscopy, voltammetry and electrochemical spectroscopy measurements of operating SOCs was developed; creating a high temperature *operando* Raman spectroscopy research capability at the University of Sheffield.

Secondly, *in situ* formation of the carbon deposits on Ni-YSZ electrodes with applied negative bias exposed to a CO₂-CO atmosphere was studied using the reactor developed previously. The applied bias has shown to promote carbon deposition on the Ni-YSZ surface. The *post-mortem* analysis showed carbon nanofibers formation at the Ni-YSZ/electrolyte interface as well as presence of larger deposits with disordered carbon structure (D1/G ratio higher than 1.5) on the electrode surface at 700 °C and 50/50 CO₂/CO ratio.

Lastly, a novel concept of using mixed ionic-electronic conducting oxides as SOC electrodes, consisting of a samarium-doped ceria oxygen ion-conductive phase and an oxygen-deficient cobalt iron oxide phase, to extend the reaction sites from the traditional TPB, was investigated. Samples sintered in N₂ atmosphere showed increased electrical conductivity compared to the ones sintered in air.

Acknowledgements

First and foremost, I would like to thank my supervisors Dr Rachael Rothman and Professor Derek Sinclair for the opportunity to undertake this research project, their guidance, valuable scientific discussions, and the possibility to gain further experience by attending conferences and going on research trips.

I would like to express my sincere gratitude to Professor Sinclair for his support, guidance, and continuous encouragement throughout and towards the end of my PhD. I would like to thank him for sharing his knowledge, expertise and time, as well as patience and understanding.

I would like to extend my gratitude to Dr Dennis Cumming for his technical knowledge and help getting this project going.

I am grateful to the technical and academic staff at the Department of Chemical and Biological Engineering and Department of Materials Science and Engineering for their assistance and facilitation of my research project, especially, Stuart Richards for helping build my reactor, Andrew Mould for training and good humour, and Dr Nik Reeves-McLaren for help with Raman spectroscopy and X-ray diffraction experiments.

In addition, I would to thank Professor Rob Walker and Kyle Reeping for accommodating my visit to Montana State University and sharing their knowledge of rig development and *operando* optical spectroscopy.

I would also like to thank my 4CU colleagues and friends, and a very knowledgeable steering committee, for stimulating discussions and memorable experience. The financial support from the Engineering and Physical Sciences Research Council (EPSRC), Grant No EP/K001329/1, is gratefully acknowledged.

A very special thank you to my PhD friends (Ana, Tom, Matt, Pratik, Abi, Dharana, Ali, Steve and many others) for friendly atmosphere in the lab and in the office, many insightful discussions, relentless energy and never-ending optimism. In particular I would like to thank Laura for being there for me when I needed it most and Alison for keeping me a great company and kindly proof-reading my thesis.

Dr Corrine Howse, a brilliant project manager and a good friend, for her help, support, and influence in my career development.

I would like to thank my friends outside the University of Sheffield, especially Julija and Viktorija, for their support and patience during the last years. Most importantly, I am grateful to my mum, grandma and my family for motivation and continuous support of my journey in the UK. Lastly, I would like to thank my partner Arek for his love, support, and endless patience.

Jevgenija Manerova

Sheffield, April 2018

Contents

1	Introduction	1
1.1	Carbon Capture and Utilisation (CCU).....	3
1.2	Fuels from CO ₂	3
1.2.1	<i>Electrochemical Energy Conversion using Solid Oxide Cells</i>	5
1.3	Research Aims	7
1.4	Thesis Structure.....	8
2	Literature Review.....	10
2.1	Working principles Solid Oxide Cells	10
2.2	Thermodynamics.....	12
2.2.1	<i>Equilibrium potential</i>	14
2.2.2	<i>Thermoneutral Voltage</i>	16
2.3	Kinetics	16
2.3.1	<i>Activation polarisation</i>	17
2.3.2	<i>Ohmic losses</i>	17
2.3.3	<i>Concentration polarisation</i>	18
2.4	Electrochemical impedance spectroscopy.....	18
2.5	Raman spectroscopy.....	23
2.5.1	<i>Fundamentals</i>	23
2.6	Current uses of Raman spectroscopy in SOCs.....	26
2.7	Experimental reactor considerations	27
3	Experimental.....	31
3.1	Sample Preparation	31
3.1.1	<i>Solid State Powder Synthesis</i>	31
3.1.2	<i>Pellet Preparation</i>	32
3.1.3	<i>Solid Oxide Cell Fabrication</i>	32
3.2	Sample Characterisation.....	34
3.2.1	<i>Density measurements</i>	34
3.2.2	<i>X-ray Diffraction</i>	35
3.2.3	<i>Sample Preparation</i>	36
3.2.4	<i>Thermogravimetric Analysis</i>	37

3.2.5	<i>Thermoelectric Measurements</i>	37
3.2.6	<i>Raman spectroscopy</i>	39
3.2.7	<i>X-ray photoelectron spectroscopy</i>	40
3.2.8	<i>Scanning Electron Microscopy</i>	40
3.3	Electrochemical Testing	43
3.3.1	<i>Start-up Procedure</i>	45
3.3.2	<i>Solid Oxide Cell Measurements</i>	45
4	Experimental Apparatus Design and Commissioning	47
4.1	Design of the Test Apparatus	47
4.1.1	<i>General Dimensions</i>	49
4.1.2	<i>Optical Access</i>	50
4.1.3	<i>Gas and Electrical Connections</i>	51
4.1.4	<i>Temperature Control</i>	52
4.1.5	<i>Materials</i>	53
4.1.6	<i>Sealing of the SOC</i>	53
4.2	Full System Commissioning	54
4.2.1	<i>Gas leak testing</i>	56
4.2.2	<i>Temperature Monitoring</i>	56
4.3	Raman microscope setup for <i>in operando</i> experiments	57
4.4	Cell test methodology	58
4.5	Electrochemical data acquisition.....	58
4.5.1	<i>Inductance correction</i>	59
4.5.2	<i>Data quality measurement (Kramers-Kronig validation)</i>	62
5	<i>Operando</i> Raman spectroscopy characterisation of carbon deposition on Ni-YSZ electrode during CO₂ electrolysis	64
5.1	Cell preparation.....	64
5.2	Benchmarking of the cells in H ₂	65
5.3	<i>Operando</i> Raman spectroscopy monitoring of carbon deposition.....	67
5.4	<i>Ex situ</i> analysis of SOCs	70
5.4.1	<i>Ex situ Raman spectroscopy analysis of carbon deposits</i>	70
5.4.2	<i>Post-mortem SEM characterisation of Ni-YSZ electrodes</i>	74
5.5	Summary	78
6	Investigation into oxygen deficient CoFe₂O₄ -based ceramic electrode materials	79

6.1	Structural and morphological characterisation of CoFe ₂ O ₄ powder	80
6.1.1	<i>Thermal analysis</i>	84
6.2	CFO pellet sintering and characterisation	85
6.2.1	<i>X-ray Powder Diffraction</i>	86
6.2.2	<i>X-ray photoelectron spectroscopy</i>	93
6.2.3	<i>Raman spectroscopy</i>	96
6.2.4	<i>Scanning electron microscopy (SEM)</i>	100
6.3	Electrical properties	102
6.3.1	<i>Conductivity</i>	102
6.4	CFO-SDC ceramic membranes for SOC application.....	105
6.4.1	<i>Phase analysis</i>	106
6.4.2	<i>Thermal analysis</i>	107
6.4.3	<i>Electrical properties</i>	108
6.4.4	<i>SEM analysis</i>	108
6.4.5	<i>Activity for CO₂/CO reduction</i>	109
6.5	Summary	115
7	Conclusions and Future Work.....	117
7.1	Conclusions	117
7.2	Future work	119
7.3	Dissemination.....	120
7.3.1	<i>Conference Proceedings</i>	120
7.3.2	<i>Oral Presentations</i>	120
7.3.3	<i>Poster Presentations</i>	120
	Bibliography	122

List of Tables

Table 2-1. Electrical symbols and impedance of common elements: the resistor, capacitor and inductor.....	20
Table 2-2. Capacitance values and possible interpretation (Irvine et al., 2004).	22
Table 2-3. A summary of pros and cons of the reported designs.....	30
Table 3-1: List of ingredients of Hionic TM electrolyte substrates (Nexceris LLC, 2015).	33
Table 5-1. Resistance and capacitance values for cells 1 &2 in H ₂ at 700 °C.....	67
Table 5-2. Resistance and capacitance values before and after bias has been applied to the cell.....	69
Table 5-3. Positions of the Raman bands, FWHM, I _{D1} /I _G , and A _{D1} /A _G ratios for carbon deposits CD1, CD2, and CD3 fitted with Gaussian (G) and Lorentzian (L) functions.	74
Table 6-1. CFO crystallite size and lattice strain estimation using Scherrer's equation and Williamson-Hall plots.	89
Table 6-2. The structural parameters of CoFe ₂ O ₄ inverse spinel material obtained from Rietveld refinement of XRD pattern in Figure 6-11.....	91
Table 6-3. Crystallographic data obtained from Rietveld structural analysis of the powder XRD data of CFO crushed pellet samples.	93
Table 6-4. XPS binding energy positions and atomic percentages of Co and Fe for CFO samples.....	96
Table 6-5. Raman phonon modes of CoFe ₂ O ₄ sintered at different temperatures and atmospheres.....	99
Table 6-6. Summary of the resistances obtained by fitting CFO-SDC SDC CFO-SDC EIS data with equivalent circuit models.	114
Table 6-7. Summary of the capacitances obtained by fitting CFO-SDC SDC CFO-SDC EIS data with equivalent circuit models.	114

List of Figures

Figure 1-1. 2014 estimated shares of global anthropogenic greenhouse gases (Source: International Energy Agency (IEA)) [4].	2
Figure 1-2. A map of possible CO ₂ and H ₂ O dissociation pathways (Graves et al., 2011).	5
Figure 1-3. High temperature electrolysis routes for CO ₂ and/or H ₂ O splitting and fuel production using renewable energy sources.	6
Figure 2-1. Schematic diagram of a solid oxide cell operated as electrolysis cell (left) and as a fuel cell (right).	11
Figure 2-2. Schematic drawing of a triple phase boundary in the SOC fuel electrode (courtesy of Dr D. J. Cumming).	12
Figure 2-3. Thermodynamics of H ₂ O and CO ₂ dissociation reactions at atmospheric pressure as a function of temperature obtained from HSC® Chemistry software. The abrupt changes in ΔH , ΔG and $T\Delta S$ at 100°C are due to vaporization of liquid water into steam.	13
Figure 2-4. Thermodynamics of water-gas shift reaction (data from HSC® Chemistry).	14
Figure 2-5. Temperature influence on the standard potential of the H ₂ O and CO ₂ electrolysis cells (data from HSC® Chemistry).	15
Figure 2-6. Theoretical and actual performance of the solid oxide fuel cell.	17
Figure 2-7. Impedance Nyquist plots of a resistor and capacitor (RC) connected in series (A), parallel (B) and resistor in series with a parallel R-C element (C).	21
Figure 2-8. An idealised EIS spectrum of SOC showing from grain, grain boundary and electrode resistance contributions (Tuller et al., 2009).	22
Figure 2-9. Principles of Rayleigh and Raman scattering. E is the energy of a photon, h is Planck's constant, ν is the excitation frequency and $\Delta \nu$ is the frequency change.	24

Figure 2-10. (A) Photograph of a Raman high temperature reaction chamber, HVC-MRA-5, made by Harrick Scientific Products (Harrick Scientific Products Inc, 2012), (B) Brightman (Imperial College London) (Brightman et al., 2012b) and (C) Pomfret (Montana State University) (Pomfret et al., 2008b).....	29
Figure 3-1: A flow chart of solid state powder synthesis adopted from Xiang et al. (2014).	32
Figure 3-2: Schematic of electrolyte-supported SOC fabrication.....	34
Figure 3-3. Bragg’s law reflection.	36
Figure 3-4: Schematic diagram of X-ray diffractometer.	36
Figure 3-5: Measurement setup of the Netzsch SBA 458 Nemesis® (NETZSCH, n.d.).	37
Figure 3-6: A simplified schematic of a Raman microscope.	39
Figure 3-7: Electron beam interaction with the bulk of the sample.....	42
Figure 3-8: Schematic diagram of an electron microscope with SE and X-ray detectors.	42
Figure 3-9: Solid oxide cell test station with optical access for Raman microscope.	44
Figure 3-10: Cyclic voltammetry experimental setup.....	46
Figure 4-1. Schematic drawing of the test apparatus (Manerova et al., 2015).	48
Figure 4-2. Schematic drawing of the detailed cross-section view of the cell housing (bottom) (Manerova et al., 2015).	49
Figure 4-3. Three-tier extrusion on the base unit.....	50
Figure 4-4. Air cooling of microscope objective using coiled copper accessory.	51
Figure 4-5. A side view of the reactor showing gas (left) and electrical (right) connections (GI – gas in, GO – gas out, B1 & B2 – bottom pins, and T1 & T2 – top pins).	52
Figure 4-6. Step-by-step rig assembly procedure.	55
Figure 4-7. Typical temperature recordings of the objective, furnace and cell during <i>operando</i> measurements.	57
Figure 4-8. Experimental setup for spectroelectrochemical characterisation of SOCs.	57

Figure 4-9. A plot of resistance and inductance versus frequency for 600 °C closed circuit experiment (on heating).	59
Figure 4-10. A plot of resistance versus temperature for closed circuit experiment.	60
Figure 4-11. A plot of inductance versus temperature for closed circuit experiment....	60
Figure 4-12. Bode plot of Z'' vs frequency for uncorrected and two inductance-corrected data (top) and the corresponding DRT (bottom).....	61
Figure 4-13. Nyquist plot of impedance data with two induction corrections (L) applied.	62
Figure 4-14. Examples of original spectrum, fitted (a) and residual (b) pattern of the Kramers-Kronig test performed on the impedance spectrum of the cell operated at 700 °C in H ₂	63
Figure 5-1. Nyquist (top) and Bode (bottom) plots of EIS data of cell 1 and 2 in H ₂ at 700 °C.	65
Figure 5-2. Current-voltage characteristics and power density of cells 1 and 2 in H ₂ at 700 °C.	66
Figure 5-3. Equivalent circuit model used to fit EIS data in Figure 5-1.....	66
Figure 5-4. Carbon D and G peak intensities obtained from Raman spectra collected at 700 °C in 50/50 CO ₂ /CO and 100 mA cm ⁻² negative bias for cell 1 (left) and 2 (right). The intensities were obtained by integrating both peaks.....	68
Figure 5-5. <i>Operando</i> Raman measurements taken at different time intervals, showing carbon growth kinetics at 700 °C in 50/50 CO ₂ /CO and 100 mA cm ⁻² negative bias.	68
Figure 5-6. Nyquist (top) and Bode (bottom) plots of EIS data of cell 1 (blue) and 2 (red) in before and after CO ₂ electrolysis at 700 °C.	69
Figure 5-7. Raman microscope image of carbon deposit CD1.	71
Figure 5-8. Deconvoluted Raman spectrum of CD1 carbon deposit.	71
Figure 5-9. Raman microscope image of carbon deposit CD2.	72
Figure 5-10. Deconvoluted Raman spectrum of CD2 carbon deposit.	72
Figure 5-11. Raman microscope image of carbon rod deposit CD3.....	73
Figure 5-12. Deconvoluted Raman spectrum of CD3 carbon rod deposit.....	73

Figure 5-13. Scanning electron (SE) and backscattered electron (BSE) images of different carbon deposits at X2.4k magnification.....	75
Figure 5-14. SEM image of carbon rod formed on Ni-YSZ surface (including approximate diameter measurements).	75
Figure 5-15. SEM images of Ni-YSZ surface after 3h CO ₂ electrolysis under 100 mA cm ⁻² bias at X15k (left) and X40k(right) magnification (cell 1).....	76
Figure 5-16. SEM images of Ni-YSZ at the electrode/electrolyte interface after 3h CO ₂ electrolysis operation under 100 mA cm ⁻² bias at X20k (left) and X40k(right) magnification (cell 1).	77
Figure 5-17. SEM images of Ni-YSZ at the electrode/electrolyte interface after 5h CO ₂ electrolysis operation under 100 mA cm ⁻² bias at X20k (top left), X40k(top right) and X80k magnification (cell 2).	77
Figure 6-1. XRD patterns of (1) α-Fe ₂ O ₃ and (2) Co ₃ O ₄ starting materials.....	80
Figure 6-2. Fe-Co-O ₂ oxide phase diagram at atmospheric <i>p</i> O ₂ . Adapted from FactSage™ (2010).	81
Figure 6-3. XRD pattern of synthesised CoFe ₂ O ₄ material.	82
Figure 6-4. Particle size distribution of CFO powders calcined at 900 °C for 2 h.....	83
Figure 6-5. SEM images of CFO powder calcined at 900 °C for 2h at (a) 5,000, (b) 20,000, (c) 40,000 and (d) 80,000 magnification.....	84
Figure 6-6. TGA curves for CFO powder under air and nitrogen atmospheres.	85
Figure 6-7. The effect of sintering temperature on the theoretical density of the CFO pellets.	86
Figure 6-8. XRD patterns of CFO calcined powder and crushed pellets sintered at 1200, 1300 and 1400°C in air.	87
Figure 6-9. XRD patterns of CFO calcined powder and crushed pellets sintered at 1200, 1300 and 1400°C under a flow of N ₂ . Extra peaks marked by the asterisks indicate secondary phase.	87
Figure 6-10. Comparison of XRD patterns of CFO 1400°C N ₂ against CoO, Fe _{0.1} Co _{0.9} O and Fe _{0.5} Co _{0.5} O patterns from ICDD PDF-4+ database.....	88
Figure 6-11. Rietveld refinement profile of the powder XRD pattern obtained for CoFe ₂ O ₄ synthesised via solid state reaction.	90

Figure 6-12. XPS spectra of CoFe_2O_4 sintered at 1200 °C for 2 hours in air in different regions: (a) survey, (b) Co 2p, (c) Fe 2p and (d) O 1s.	95
Figure 6-13. Raman spectra of CoFe_2O_4 sintered at different temperatures and atmospheres.....	98
Figure 6-14. SEM images of CFO sintered at 1200°C for 2h in air at x5,000 (a) and x20,000 (b) magnification.....	101
Figure 6-15. SEM images of CFO sintered at 1300°C for 2h in air at x5,000 (a) and x20,000 (b) magnification.....	101
Figure 6-16. SEM images of CFO sintered at 1400°C for 2h in air at x5,000 (a) and x20,000 (b) magnification.....	101
Figure 6-17. SEM images of CFO sintered at 1300°C for 2h under flow of N_2 at x5,000 (a) and x20,000 (b) magnification.....	102
Figure 6-18. SEM images of CFO sintered at 1300°C for 2h under flow of N_2 at x5,000 (a) and x20,000 (b) magnification with additional features appearing after thermal etching.....	102
Figure 6-19. Plots of electrical conductivity (a) and Seebeck coefficient (b) against temperature for CFO samples measured in Ar.....	103
Figure 6-20. The temperature dependence of the DC electrical conductivities for CFO samples under different sintering atmospheres.....	104
Figure 6-21. XRD spectra of 50/50 wt. % CFO-SDC powder calcined at different temperatures.....	106
Figure 6-22. XRD spectra of 50/50 wt. % CFO/SDC precursor calcined at 1200 °C.	107
Figure 6-23. TGA curves for CFO powder and SDC nanopowder in N_2	107
Figure 6-24. The Arrhenius plot of 50/50 wt. % CFO-SDC samples sintered in N_2 ...	108
Figure 6-25. (a) SEM micrograph of 50/50 wt. % CFO/SDC sample sintered at 1300 °C in N_2 for 2 h and overlapped with elemental maps of Fe(b), Co(c), O(d), Ce(e) and Sm(f).	109
Figure 6-26. Potential sweep on the CFO-SDC SDC CFO-SDC symmetric cell at 850 °C in 50% CO_2/CO . The sweep was repeated 3 times and showed good reproducibility.	110

Figure 6-27 Comparison of the electrochemical performance the CFO-SDC SDC CFO-SDC symmetric SOC in terms of the ASR in fuel cell and electrolysis modes, and 50/50 (a) and 70/30 (b) CO ₂ /CO atmospheres.	110
Figure 6-28. Comparison of the electrochemical performance the CFO-SDC SDC CFO-SDC symmetric SOC in terms of the ASR in 50/50 and 70/30 CO ₂ /CO atmospheres, and fuel cell (a) and electrolysis (b) testing modes.	111
Figure 6-29. Impedance spectra of the CFO-SDC/CFO symmetrical cell tested in 50/50 CO ₂ /CO atmosphere in the temperature range 500–850 °C.	112
Figure 6-30. Impedance spectra of the CFO-SDC/CFO symmetrical cell tested in 50/50 CO ₂ /CO atmosphere in the temperature range 500–850 °C.	113
Figure 6-31. The Arrhenius plot of CFO-SDC SDC symmetric cell in analysed in CO ₂ /CO atmospheres.	115

List of Abbreviations and Acronyms

Symbols

A	Area
a_i	Activity of species i
C	Capacitance
E	Energy
E_a	Activation Energy
E_{th}	Thermoneutral cell voltage
F	Faraday constant
f	Frequency
h	Planck's constant
i	Current
I	Intensity
j	Current density
L	Inductance
P	Gas partial pressure
R	Resistance
T	Temperature
V	Voltage
Z	Impedance
α	Polarizability
ΔG	Gibbs free energy change
ΔH	Enthalpy change
ΔS	Entropy change
ϵ	Strain
η	Overpotential
θ	Incident angle
λ	Wavelength
μ	Induced dipole
ρ	Density
σ	Conductivity

τ	Time constant
ν	Frequency (Raman spectroscopy)
φ	Phase shift
ω	Angular frequency
Z'	Real part of the impedance
Z''	imaginary part of the impedance

Abbreviations

AC	Alternating current
ADIS	Analysis of differences in impedance spectra
ASR	Area-specific resistance
CFO	CoFe_2O_4
CNT	Carbon nanotube
CPE	Constant phase element
CV	Cyclic voltammetry
DFT	Density functional theory
EDS	Energy-dispersive X-ray spectroscopy
EIS	Electrochemical impedance spectroscopy
FRA	Frequency response analyser
GDC	Gadolinium-doped ceria
GHG	Greenhouse gas
IR	Infrared
KK	Kramers-Kronig
LSCF	Lanthanum strontium cobalt ferrite
LSF	Lanthanum strontium ferrite
LSGM	Lanthanum strontium gadolinium manganite
LSM	Lanthanum strontium manganese oxide
LSV	Linear sweep voltammetry
MIEC	Mixed ionic-electronic conductor
OCV	Open circuit voltage
PEM	Polymer electrolyte membrane
RS	Raman spectroscopy
RWGS	Reverse water-gas shift

SDC	Samaria-doped ceria
SEM	Scanning electron microscopy
SOC	Solid oxide cell
SOFC	Solid oxide fuel cell
TEC	Thermal expansion coefficient
TPB	Triple phase boundary
UV	Ultraviolet
WGS	Water-gas shift
XPS	X-ray photoelectron spectroscopy
XRD	X-ray diffraction
YSZ	Yttria-stabilised zirconia
CCS	Carbon capture and storage
SOEC	Solid oxide electrolysis cell
i-V	Polarisation curve
IT	Intermediate temperature

1 Introduction

Currently fossil fuels provide the majority of the world's energy needs, resulting in increasing levels of greenhouse gases (GHGs), such as carbon dioxide (CO₂), methane (CH₄), water vapour and nitrogen oxides (NO_x) released during the combustion processes. GHG is a gas in the atmosphere that absorbs and emits infrared radiation, causing a warming process also known as greenhouse effect. Although CO₂ makes up only 0.04% of the atmosphere it has a significant impact on climate dynamics (Bindoff et al., 2013). Even at such a low concentration, CO₂ absorbs infrared radiation and enhances the greenhouse effect, posing a serious environmental threat and a leading cause of global climate change (Davis et al., 2010). Although both natural and anthropogenic CO₂ are present in the atmosphere, human activity, such as burning of fossil fuels, farming, deforestation, and industrial processes is by far the largest contributor to the observed increase in atmospheric CO₂ levels. Man-made CO₂ emissions into the atmosphere are approximately 36 billion tonnes per year (2015 statistics (EDGAR, 2016) are more than a hundred times larger than the maximum amount of the estimated volcanic CO₂ flux (Farmer and Cook, 2013). Among the many human activities, the use of energy accounts for an immense 68% of all estimated GHG emissions as shown in Figure 1-1.

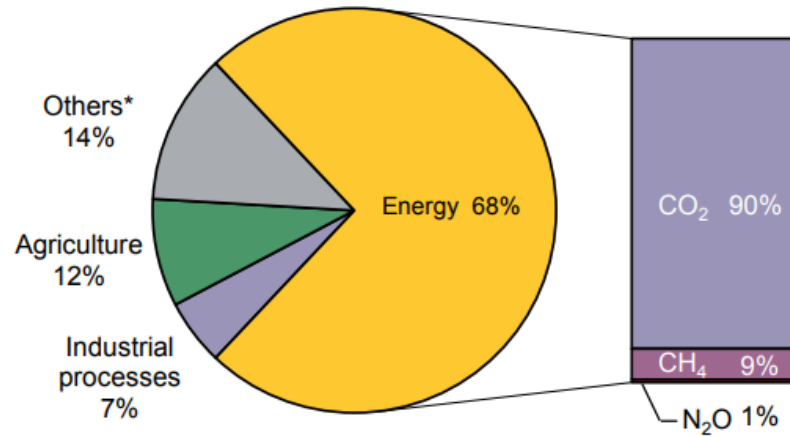


Figure 1-1. 2014 estimated shares of global anthropogenic greenhouse gases (Source: International Energy Agency (IEA)) [4].

Although water vapour is the most abundant GHG, it has a very short atmospheric lifetime and, therefore, is not considered a high risk. Despite the fact that CO₂ potency is considerably lower compared to other GHG, its continuous accumulation and heat trapping abilities raise concerns. The Global Warming Potential (GWP) of CH₄ and N₂O are estimated to be at least 28 and 265 times higher over a 100-year period compared to that of CO₂ (GWP = 1), respectively (EPA, 2016). In 2017, according to the observations collected by the U.S. National Oceanic and Atmospheric Administration, the atmospheric CO₂ concentration reached 404 ppm; that is 120 ppm higher than before pre-industrial times (NOAAA, 2017).

The increasing atmospheric concentrations of CO₂ will inevitably have negative implications on the environment and global ecology. A particular concern is the rise in ocean temperatures and acidification affecting marine ecosystems (Hall-Spencer et al., 2008).

Carbon Capture and Sequestration (CCS) mitigation of large scale CO₂ release, such as industrial power plants, directly at the emission sources and storing it in geological formations, has been suggested. However, high costs associated with capturing and compressing CO₂ make it not economically feasible incentives and regulatory mechanisms are required. In fact, in 2015 UK's government withdrew £1 billion of funding from the competition to pioneer this technology development due to concerns over future costs to consumers, leading to its cancellation (BBC, 2015). Furthermore, there are unknown environmental and ecological impacts associated with storing CO₂

deep under water that can arise from uncontrolled releases, such as leaks and faulty equipment across the plant and transport pipeline.

At the UN climate change conference in Paris (COP21) at the end of 2015 the EU pledged to reduce emissions by at least 40% by 2030 to achieve a long-term goal of reducing the global average temperature to below 2°C above the pre-industrial levels; the first-ever universal, legally binding global climate deal (European Commission, 2016). Instead of storing the captured CO₂ underground, it can be used as a valuable feedstock to produce chemicals and fuels in a process called carbon capture and utilization (CCU). CCU can be deployed in addition to CCS as a part of a more feasible short-term implementation strategy to achieve ambitious targets of carbon reduction.

1.1 Carbon Capture and Utilisation (CCU)

CCU is aimed at recycling CO₂ into useful products such as synthetic fuels and valuable chemicals (Aresta, 2010, Styring et al., 2014). It is commercially attractive because it regards CO₂ as a chemical feedstock rather than a liability, in contrast to the alternative CCS mitigation scenario. Although converting carbon dioxide into chemicals will not reduce the anthropogenic CO₂ emissions drastically due to mismatch between the amount of CO₂ produced globally (estimated 20 gigatonnes of carbon dioxide per annum) and need for chemicals (<100 megatonnes per annum), it could still be a key enabling technology in cutting emissions and influencing the use of renewables and promoting recycling behaviour towards waste reduction.

One area where CCU technology could make a substantial difference in reducing anthropogenic CO₂ emissions is the electrochemical conversion of CO₂ into synthetic hydrocarbon fuels to create a closed-loop carbon-neutral fuel cycle (Styring et al., 2014).

1.2 Fuels from CO₂

Although, in recent years, there has been increased development of electric propulsion systems, conventional hydrocarbon fuels will continue to be needed as it will take decades to transform the existing infrastructure to accommodate carbon-free energy carriers, such as compressed hydrogen, batteries, and supercapacitors. The transportation industry, particularly marine and airlines, will continue to rely on high energy density fuels. In the meantime, however, more sustainable alternatives should be used to produce synthetic

liquid fuels, slowly moving away from fossil and biomass feedstocks (European Expert Group, 2011, Metzger et al., 2013).

There is a natural carbon cycle in the atmosphere that has been significantly affected by the humans burning carbon-containing fuels for energy. To avoid further GHGs accumulation and to reduce the risk of catastrophic climate change, the closed carbon cycle approach is necessary (Styring et al., 2014). To reduce anthropogenic CO₂ emissions, the electrochemical reduction should be powered by renewable energy sources such as wind, solar and hydropower and/or nuclear energy. In the long run the shift to negative carbon production is needed and can only be achieved by a combined technological approach in using CO₂ as raw material for large-scale industrial processes.

One of the many ways of utilising CO₂ is to electrochemically convert it into fuels and value-added chemicals by reacting it with H₂. Capturing CO₂ from air and large industrial plants would create a closed carbon cycle. The CO₂ fuels produced in a carbon-neutral manner can be stored as chemicals, easing the delivery to the end-consumer and providing balancing capacity for supply and demand of intermittent renewable energy during peak and off-peak times.

CO₂ can be electrochemically dissociated into carbon monoxide (CO) or simultaneously electrolysed with steam to produce syngas, a mixture of hydrogen and carbon monoxide (H₂ + CO) as well as methane (CH₄), ethylene (C₂H₄), formic acid (HCOOH), methanol (CH₃OH) and ethanol (C₂H₅OH), depending on the catalyst and cell parameters used. Syngas can be used as a precursor for the Fischer-Tropsch process (or similar catalytic fuel synthesis) to produce long chain, synthetically-derived hydrocarbon fuels that can be directly and conveniently utilized in current infrastructure.

Graves et al. (2011) reviewed different CO₂ recycling processes including electrolysis, photoelectrolysis and thermochemical cycles forming a comprehensive summary of the available CO₂ and H₂O dissociation pathways, as presented in Figure 1-2. The two sources of the feedstock CO₂ are atmospheric air and stationary sources such as heavy industry. The CO₂ capture technologies are typically based on chemical absorption, adsorption processes, or membrane separation (Yu et al., 2012, Yang et al., 2008). There are different sources of energy can be used for power: solar, nuclear, wind, hydro and geothermal.

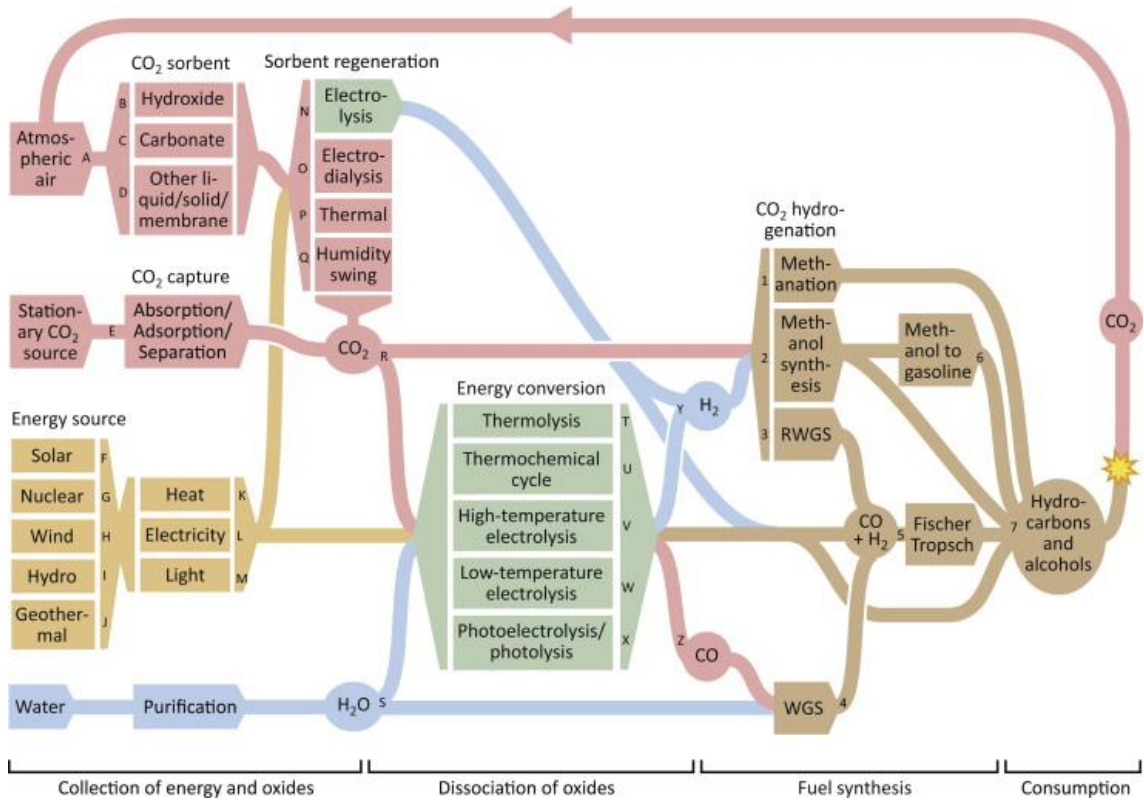


Figure 1-2. A map of possible CO₂ and H₂O dissociation pathways (Graves et al., 2011).

High temperature Solid Oxide Cell (SOC) technology is a suitable contender for efficient and sustainable utilisation of CO₂ (Wachsman et al., 2012). It has the highest potential efficiency for conversion of fuel to electricity and vice versa, as well as the ability to operate on any hydrocarbon fuel, hydrogen or biomass. SOCs find particular use in stationary, distributed power generation and combined heat and power (CHP) applications. The waste heat utilisation alongside the operating SOC stack enables a total efficiency close to 90% (Huang and Goodenough, 2009).

1.2.1 Electrochemical Energy Conversion using Solid Oxide Cells

The biggest advantage of SOC technology over other similar energy conversion methods is its versatility. SOCs are fuel flexible, capable of operating on both conventional liquid fuels and alternative fuels like hydrogen or biofuel. Depending on the fuel and cell geometry and materials, the operating temperature of an SOC can be reduced. Most important, however, is the ability to operate in reverse, expending or producing energy on-demand providing a mechanism for storing renewable electricity when it could otherwise not be used. Figure 1-3 shows three common electrolysis routes for CO₂ and

H₂O: H₂O electrolysis used for CO₂ hydrogenation, simultaneous H₂O and CO₂ co-electrolysis and CO₂ electrolysis.

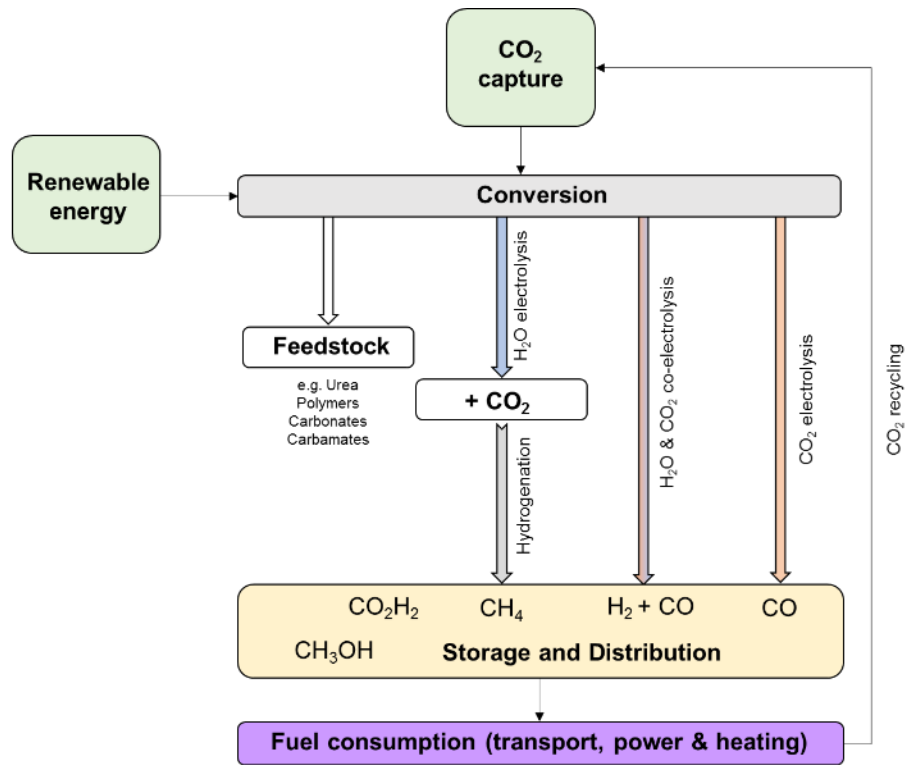


Figure 1-3. High temperature electrolysis routes for CO₂ and/or H₂O splitting and fuel production using renewable energy sources.

Understanding co-electrolysis of steam and CO₂ is complicated by the competing water-gas shift reaction, however, with an increased amount of effort directed at understanding the electrochemical performance of SOCs through experimental and modelling work, significant progress has been made. Now the focus has shifted towards lowering the operating temperature whilst continuing to improve SOC power density (Wachsman et al., 2012). Lower operating temperatures will decrease the operating costs, speed up the start-up procedure, facilitate the use of other metal catalysts, and open new opportunities for material and component selection.

However, lowering the operating temperature can also pose the risk of carbon deposition during CO₂ electrolysis and deactivation of active catalytic sites. Currently, only a handful of research groups (e.g. Montana State University (USA) (Pomfret et al., 2008b) and Imperial College London (UK) (Duboviks et al., 2015, Brightman et al., 2012b)) have used vibrational spectroscopy alongside traditional electrochemical measurements to study carbon deposition to gain an understanding of the reaction mechanism(s), aiding the development of impurity-tolerant SOC electrode materials.

SOC technology is still under development, however, in the last decade an immense amount of progress has been made, and the technology is slowly becoming commercially available. First SOFC stacks have already been introduced to Microsoft data centres (SOLIDpower, 2017) and UK-based Ceres Power and Cummins Inc. are developing a novel, modular 5 kW SOFC system that is scalable up to 100 kW, for use in data centres at first and further application to other markets such as commercial combined heat and power (CHP) and electric vehicles (Elsevier, 2016).

1.3 Research Aims

The research aims of this thesis are fourfold. Firstly, there was a need for designing, fabricating and commissioning a reactor and portable test station for simultaneous electrochemical and spectroscopic analysis of SOCs. It was the first attempt to build this kind of reactor in-house which was required to be versatile and robust at high temperatures under highly reducing and/or oxidising atmospheres. The main attractiveness of the reactor was the ability to easily modify the setup to be used with different vibrational spectroscopy techniques, expanding the capabilities of the research group. As with any new product development the extensive commissioning process and continuous improvement of the design were required.

Secondly, the in-house development of SOCs components and assemblies was investigated. This aimed at reducing the overall cost of cells by applying different fabrication methods (e.g. tape casting, screen printing or infiltration) and sintering profiles, allowing for greater selection of materials and control of microstructure and cell geometries.

Thirdly, and most importantly, this work aimed to capture and understand the electrochemical processes occurring during real-time operation of SOC was investigated. Particularly, under the conditions that were borderline susceptible to carbon deposition, which can adversely affect the performance of the cell. *Operando* Raman spectroscopy provides additional information about the chemical transformation occurring on the surfaces of the fuel electrode during CO₂ electrolysis as well as an insight to the degree of structural disorder of carbon deposits. The specimens are analysed *post-mortem* using Scanning Electron Microscopy (SEM) to reveal microstructural degradation that occurred during cell operation.

Lastly, a significant part of the thesis is dedicated to development of novel ceramics based on mixed ionic-electronic conductors to electrodes for intermediate to high temperature range of solid oxide cells SOCs.

1.4 Thesis Structure

Chapter 2 introduces the fundamental principles of SOC operation and the material requirements for different operating temperatures. The fundamentals of the key analysis techniques, electrochemical impedance spectroscopy (EIS) and Raman spectroscopy (RS) are also discussed in this chapter. The basic reaction mechanisms and thermodynamics are outlined to provide the background required for later discussion and interpretation of the results. It is followed by a literature review, presenting the latest developments in knowledge on CO₂ conversion using SOC and the use of vibrational spectroscopies to identify deleterious phase transformations and carbon formations during cell operation. The review also covers novel material development for SOC applications.

Chapter 3 describes the experimental methods and procedures for material processing, pellet and SOC sample fabrication, testing and analysis; as well as different techniques used to analyse material properties, sample characteristics, and electrochemical performance (including data quality).

Chapter 4 outlines the development and commissioning of the electrochemical reactor for *operando* measurements of SOCs, and the importance of data correction for inductive artefacts from the equipment and other surroundings.

Chapter 5 presents the *operando* experimental results collected during CO₂ electrolysis – the electrochemical performance of cells and Raman spectroscopy measurements. The *ex situ* investigations and data analysis are followed by a chapter discussion and conclusions.

Chapter 6 features novel materials development for SOCs based on mixed ionic-electronic conductors. X-ray diffraction (XRD) and 4-point DC conductivity measurements are used to characterise the materials phase and electrical conductivity, respectively. Different analysis techniques are employed to investigate the material properties.

Finally, in Chapter 7 the overall conclusions and recommendations for further work are presented.

2 Literature Review

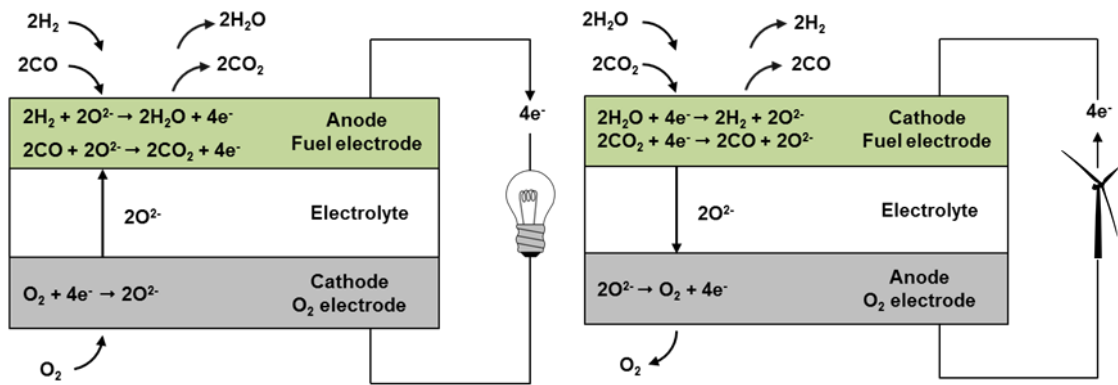
High temperature Solid Oxide Cells (SOCs) has recently attracted great interest for future power generation due to their high potential efficiency, low emissions, and fuel flexibility. This chapter will introduce state-of-the-art SOC technology including the operating principles, general requirements, electrochemical reactions, and thermodynamics. This will be followed by the literature review of the current research activities in the SOCs field.

As previously mentioned, SOCs are reversible devices and can be operated in electrolysis and/or fuel cell modes. Although the work in this dissertation mainly focuses on electrolysis operation, for clarity, both concepts will be discussed.

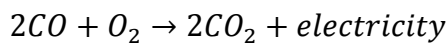
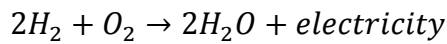
2.1 Working principles Solid Oxide Cells

A SOC is a solid-state electrochemical device comprising of two porous electrodes separated by a dense, ion-conducting electrolyte. In fuel cell mode, the SOC oxidises the feed and produces electricity, whereas in electrolysis mode, the electricity is utilised and the feed is reduced, as shown in Figure 2-1. In both scenarios, the oxygen ions are transported from the cathode to the anode across the solid oxide electrolyte. The SOCs are manufactured in different geometries (e.g. planar, tubular and flat tubular) and configurations (e.g. fuel electrode, electrolyte or metal-supported). Depending on the configuration of the cell, the thickness of the electrolyte ranges between 5 and 250 μm . The minimum electrolyte thickness in the electrolyte-supported cells is usually $\sim 150 \mu\text{m}$ (Joo and Choi, 2008), hence the operating temperature is often higher to compensate for

the high ohmic loss (Will et al., 2000). The electrodes contain both metallic and ceramic components, also referred to as a cermet, to ensure good contact of ions, electrons and reacting chemical species, necessary for electrochemical reactions to occur. A region of contact between these three phases is known as a triple phase boundary (TPB) and spread from the electrode/electrolyte interface into the electrode volume as shown in Figure 2-2. It illustrates the percolating network of active and inactive TPB sites due to lack of connectivity in the electronic and ionic phases of Ni-YSZ electrode. The length of TPB is clearly affected by the structure and composition and is typically concentrated within 10 μm from the electrolyte (Gorte and Vohs, 2003, Brown et al., 2000).



Net cell reactions:



Net cell reactions:

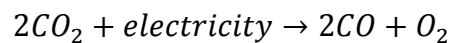
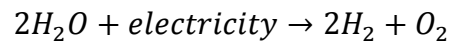


Figure 2-1. Schematic diagram of a solid oxide cell operated as electrolysis cell (left) and as a fuel cell (right).

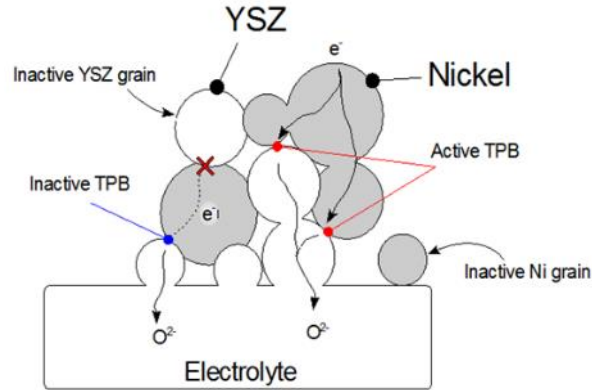
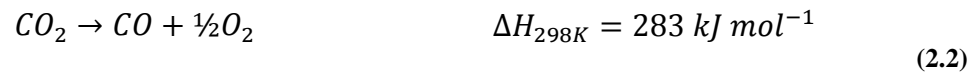
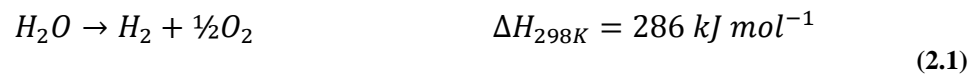


Figure 2-2. Schematic drawing of a triple phase boundary in the SOC fuel electrode (courtesy of Dr D. J. Cumming).

2.2 Thermodynamics

The dissociation of CO_2 , H_2O or a mixture of both is an endothermic reaction. The reactions and their associated enthalpies are shown in equations (2.1 and (2.2).



The energy change of each reaction is given by:

$$\Delta H = \Delta G + T\Delta S \quad (2.3)$$

where ΔH is the enthalpy change of the reaction (total thermal energy available); T is the absolute temperature; ΔS is the molar entropy change; and ΔG is the Gibbs free energy. The term $T\Delta S$ represents the heat demand to split the water or CO_2 . The thermodynamic data for these reactions is presented in Figure 2-3. In both cases, ΔG , the electric energy demand for the dissociation reaction, decreases with temperature, reducing the useful electrical work requirement. The heat demand ($T\Delta S$) gradually increases with temperature, resulting in only a slight increase in thermal energy demand, ΔH . H_2O and CO_2 splitting processes cannot proceed below 286 kJ mol^{-1} and 283 kJ mol^{-1} without external energy source, respectively. The overall feasibility of the reaction depends on

the sign of ΔG . If ΔG is positive, like here, the process is non-spontaneous and requires an input of energy.

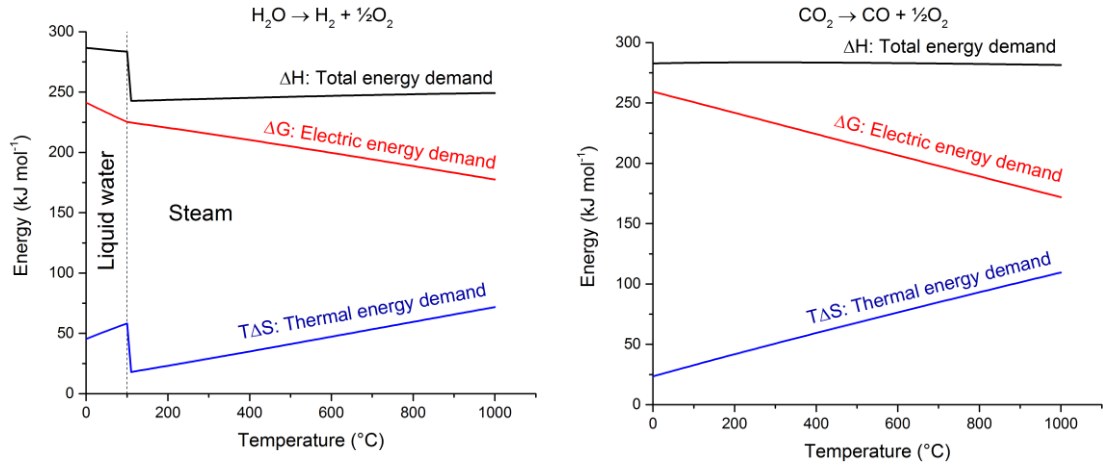


Figure 2-3. Thermodynamics of H₂O and CO₂ dissociation reactions at atmospheric pressure as a function of temperature obtained from HSC® Chemistry software. The abrupt changes in ΔH , ΔG and $T\Delta S$ at 100°C are due to vaporization of liquid water into steam.

From a thermodynamic perspective, it is advantageous to operate at high temperature due to the energy requirements for H₂O and/or CO₂ electrolysis as both of the reactions are endothermic. The necessary heat can be obtained from solar concentrators or waste heat from combined heat and power stations or nuclear power plants (Singh et al., 2009). Furthermore, the reaction kinetics increases at high temperatures, leading to decreased internal resistance of the cell and therefore increased efficiency (Elder et al., 2015).

The H₂O electrolysis for H₂ production has been studied extensively and compared to CO₂ electrolysis. It is easy to separate products from unconverted reactants as water can be simply condensed to liquid, CO produced during CO₂ electrolysis, however, would require gas phase separation. Alternatively, H₂ can be used to reduce CO₂ to CO in a co-electrolysis process via the water-gas shift (RWGS) reaction (equation (2.4)). This requires temperature above 816 °C as below this temperature the water-gas shift (WGS) reaction, CO reduction of water, is more favourable. Figure 2-4 shows the thermodynamics for the WGS and RWGS reactions.



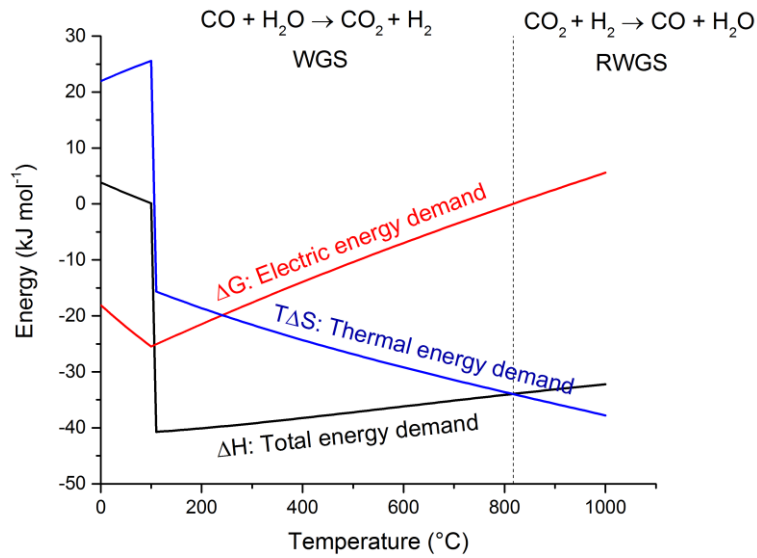


Figure 2-4. Thermodynamics of water-gas shift reaction (data from HSC® Chemistry).

2.2.1 Equilibrium potential

The net reaction for CO₂ electrolysis in SOC is given by:



The Gibbs free energy change, ΔG , for the above reaction can be expressed as follows:

$$\Delta G = \Delta G^\circ + RT \ln \left(\frac{a_{\text{CO}} \cdot a_{\text{O}_2}^{1/2}}{a_{\text{CO}_2}} \right) \quad (2.6)$$

where ΔG° is the standard molar Gibbs free energy change at the temperature T ; R is the gas constant ($8.3147 \text{ J K}^{-1} \text{ mol}^{-1}$) and a_{CO_2} , a_{CO} and a_{O_2} are the activities of the reactants and products for the reaction (2.6).

The activities of the reactants and products can also be given as partial pressures for an ideal gas:

$$a_{\text{CO}_2} = \frac{P_{\text{CO}_2}}{P_{\text{CO}_2}^0}, \quad a_{\text{CO}} = \frac{P_{\text{CO}}}{P_{\text{CO}}^0} \quad \text{and} \quad a_{\text{O}_2} = \frac{P_{\text{O}_2}}{P_{\text{O}_2}^0} \quad (2.7)$$

The reaction can then be written as:

$$\Delta G = \Delta G^\circ + RT \ln \left(\frac{P_{\text{CO}} \cdot P_{\text{O}_2}^{1/2}}{P_{\text{CO}_2}} \right) \quad (2.8)$$

The reversible potential of the cell, E , can be calculated from standard free energy change:

$$E = -\frac{\Delta G}{nF} \quad (2.9)$$

where F is Faraday constant ($96,487 \text{ C mol}^{-1}$) and n is the number of electrons participating in the reaction. In the case of CO_2 electrolysis, $n=2$. If the reactants and products are at standard temperature and pressure (STP) conditions, the equation can be represented as

$$E^0 = -\frac{\Delta G^0}{nF} \quad (2.10)$$

The variations of standard potential of the cell with temperature for H_2O and CO_2 reactions are shown in Figure 2-5. The relationship between the ideal standard potential for the SOC, E^0 , and the ideal equilibrium potential, E , at the operating temperature and partial pressures of the reactants and products is given by Nernst equation (2.11).

$$E = E^0 - \left(\frac{RT}{2F}\right) \ln\left(\frac{P_{\text{CO}} \cdot P_{\text{O}_2}^{1/2}}{P_{\text{CO}_2}}\right) \quad (2.11)$$

The Nernst potential is the reversible potential of the cell, also known as open circuit voltage (OCV).

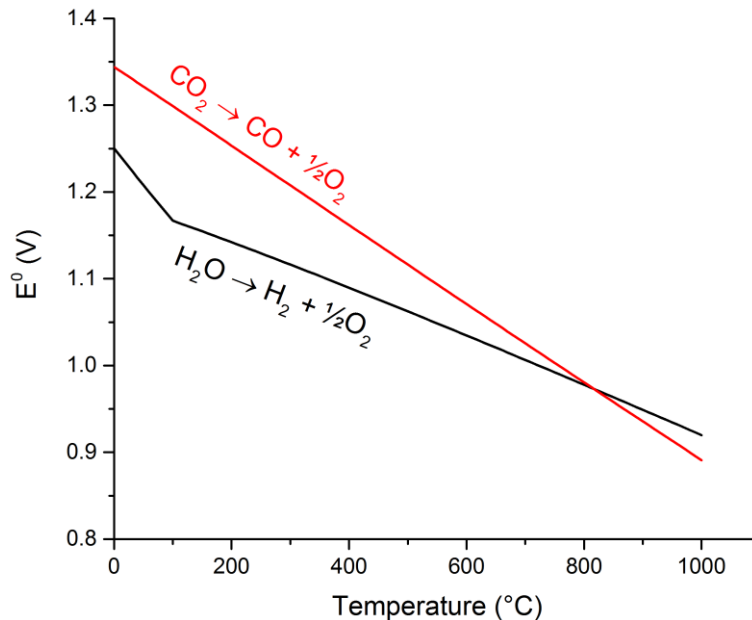


Figure 2-5. Temperature influence on the standard potential of the H_2O and CO_2 electrolysis cells (data from HSC® Chemistry).

2.2.2 Thermoneutral Voltage

There is a thermal disparity between fuel cell and electrolysis operation modes: heat is an important input for electrolysis (typically endothermic or close to thermoneutral) and a by-product of the fuel cell (typically exothermic). The thermoneutral voltage (E_{th}) is defined by equation (2.12) and is the voltage needed for electrolysis reactions to occur without additional supply of heat or electricity.

$$E_{tn} = \frac{\Delta H}{nF} \quad (2.12)$$

For electrolysis reactions in equations (2.1) and (2.2), $E_{th} > E$. To operate below E_{th} , the heat must be applied to the cell from an external source. In practice, excess heat above the E_{th} requirements is often needed to account for the heat lost from the system to the surroundings.

2.3 Kinetics

The ideal and actual performance of the SOC are different, mostly due to the irreversible losses (Kaur, 2015) depicted in Figure 2-6 (cell voltage scanned downwards, producing current – fuel cell operation). The voltage losses are generally known as polarisation or overpotential; both of these terms are used interchangeably in literature. There are three primary sources of polarisation in a SOC device: activation polarisation, η_{act} , ohmic polarisation, η_{ohm} , and gas concentration polarisation, η_{conc} . The polarisation losses are functions of an applied current (i) hence the measured cell voltage is always lower than its ideal potential in a fuel cell mode and larger during electrolysis operation. The total voltage, V , of the SOC is:

$$V = E - \eta_{act} - \eta_{ohm} - \eta_{conc} \quad (2.13)$$

The activation and concentration polarisation tend to have non-linear responses and are dominant at low and high current densities, respectively. The ohmic loss, on the other hand, linearly increases with the current density. Cell voltage loss can also originate from leakages from current leakages through the electrolyte, particularly for novel electrolytes, and imperfect seals.

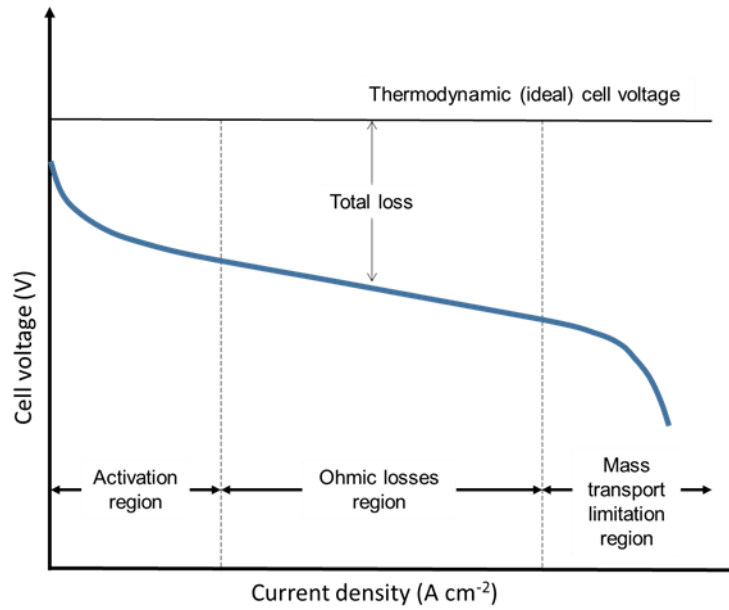


Figure 2-6. Theoretical and actual performance of the solid oxide fuel cell.

2.3.1 Activation polarisation

The activation polarisation represents the losses associated with the charge transfer polarisation. It is the voltage drop needed to overcome the activation barrier for the electrochemical reaction to take place. The activation polarisation is directly proportional to the increase in a current flow and can be expressed as the Tafel equation:

$$\eta_{act} = \frac{RT}{\alpha nF} \ln \left(\frac{i}{i_0} \right) \quad (2.14)$$

where α is the charge transfer coefficient, i is the current density and i_0 is the exchange current density. The activation polarisation is the rate-determining step; describing the charge transfer reaction at the triple phase boundary. There are a great number of factors that can affect the electrochemical reaction and lead to activation losses; these include adsorption, dissociation, surface diffusion, and electron transfer. The activation losses can be mitigated by increasing the operating temperature, changing the material properties (better electrocatalyst), microstructure, atmosphere and/or current (Elder et al., 2015).

2.3.2 Ohmic losses

The ohmic polarisation is predominantly caused by the ionic resistivity of the electrolyte. Other contributions come from lack of electronic conductivity in the electrode and various

contact resistances, such as electrical contacts, wires and interconnects. The ohmic overpotential is directly proportional to the applied current and has a linear response derived from Ohm's law ($V = IR$):

$$\eta_{ohm} = iR \quad (2.15)$$

where R is the total resistance of the SOC.

Choosing a good ionic conductor as an electrolyte, making it as thin as possible and operating at elevated temperature will decrease the ohmic losses.

2.3.3 Concentration polarisation

The diffusion or concentration polarisation is most prominent at high current densities when the reactant gas struggles to reach the active reaction sites close to electrode/electrolyte interface. However, these losses tend to occur over the entire range of the current density. The coarser the electrode microstructure, the easier it is for the gas to diffuse into the electrode and access the TPB thus the smaller η_{conc} . The concentration losses can be expressed as:

$$\eta_{conc} = \frac{RT}{nF} \ln \left(1 - \frac{i}{i_0} \right) \quad (2.16)$$

During SOC operation the major contributor to the concentration polarisation is the mass transport of the gaseous species through the porous electrode and slow removal of products from the reaction sites (Stolten, 2010). Other processes affecting the concentration polarisation are diffusivity of the reactants, the partial pressures of the gases and the applied current density.

2.4 Electrochemical impedance spectroscopy

Electrochemical impedance spectroscopy (EIS) is a dynamic technique where a sinusoidal voltage or current perturbation is applied to the cell over a wide range of frequencies and the amplitude and phase shift of the resulting current or voltage response is measured and used to construct an impedance spectrum.

Electrochemical reactions involve the transfer of electrons between a chemical species and an electrode surface. Different processes occur during the reaction, these typically

include: adsorption of electroactive chemical species onto electrode surfaces, electrolyte resistance, mass transfer from the bulk and charge transfer at electrode surfaces (Yuan et al., 2009).

Each of these reaction processes can be represented by an electrical component or an equivalent circuit. The three most common components to make up an electric circuit are a resistor, a capacitor, and an inductor.

An ideal resistor follows Ohm's law at all current and voltage levels and its impedance consists only of a real part, which is equal to its resistance, R . The resistance does not depend on frequency and the current and voltage signals of an ideal resistor are always in phase with each other (Gamry, 2015).

In contrast, a capacitor and an inductor have only an imaginary component and will vary with frequency. In a pure capacitive circuit (with only a capacitor and AC power source), the current leads the voltage by 90° (the phase shift between the voltage and current). Similarly, in a pure inductive circuit, current lags voltage by 90° . These definitions, however, are idealisations; there are no such things as a pure resistor, capacitor or inductor (Serway and Vuille, 2011). For instance, a resistor will often contain unwanted parasitic capacitance or inductance.

The sinusoidal voltage of varying frequency applied across the circuit can be expressed as:

$$V_t = V_0 \sin(\omega t) \quad (2.17)$$

where V_t is the instantaneous voltage at time t , V_0 is the amplitude of the applied signal and ω is the angular frequency given by $\omega = 2\pi f$ in radians per second (f is frequency expressed in Hertz).

The measured current response signal (I_t) of a linear system is shifted in phase (φ) and has a different amplitude (I_0):

$$V_t = V_0 \sin(\omega t) \quad (2.18)$$

$$I_t = I_0 \sin(\omega t + \theta) \quad (2.19)$$

Using Ohm's law the impedance of the system can be expressed as:


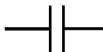

$$Z = \frac{V_t}{I_t} = \frac{V_0 \sin(\omega t)}{I_0 \sin(\omega t + \theta)} = |Z| \frac{\sin(\omega t)}{\sin(\omega t + \theta)} \quad (2.20)$$

or as a complex number, Z^* , as shown below:

$$Z^* = Z' - jZ'' \quad (2.21)$$

The complex impedance of the most common elements and their commonly adopted symbols are given in Table 2-1. Like resistors, capacitors and inductors are characterised by their capacitance, C , and inductance, L .

Table 2-1. Electrical symbols and impedance of common elements: the resistor, capacitor and inductor.

Element (Units)	Complex Impedance	Symbol
Resistor (Ω)	$Z_R = R$	
Capacitor (F)	$Z_C = \frac{1}{j\omega C}$	
Inductor (H)	$Z_L = j\omega L$	

The individual electrical components can be connected in series and/or in parallel to produce more complex equivalent circuits (Gamry, 2015). The equivalent impedance of the elements joined in series is straightforward – the impedances add up:

$$Z_{eq} = Z_1 + Z_2 + \dots + Z_n \quad (2.22)$$

The impedance of elements connected in parallel is calculated by summing up the reciprocals of the individual impedances (Gamry, 2015):

$$\frac{1}{Z_{eq}} = \frac{1}{Z_1} + \frac{1}{Z_2} + \dots + \frac{1}{Z_n} \quad (2.23)$$

EIS data are often represented as a complex impedance plane plot (Nyquist plot) also known as a Cole-Cole plot. The magnitude and direction of the impedance vector of a particular frequency is represented by a series of points (Ribeiro et al., 2015). The

abscissa of the Nyquist plot represents the real part of impedance, Z' , and the ordinate represents the imaginary part, Z'' , from the complex impedance given in equation (2.20). Examples of Nyquist plots for elements connected in series and parallel as well as both (R-C element) are illustrated in Figure 2-7.

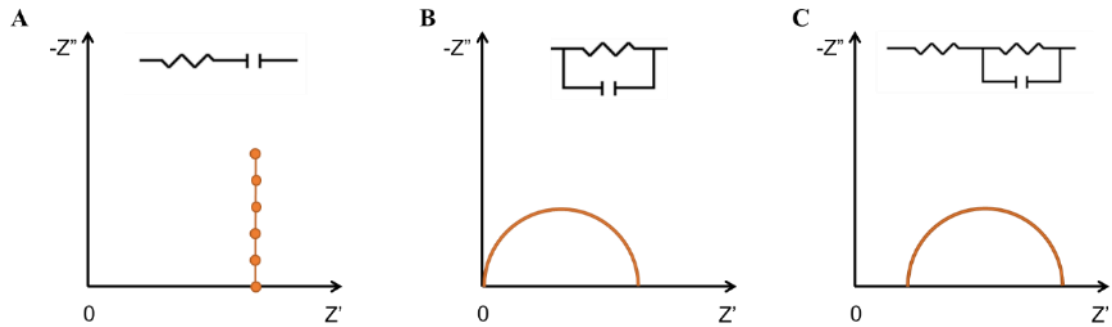


Figure 2-7. Impedance Nyquist plots of a resistor and capacitor (RC) connected in series (A), parallel (B) and resistor in series with a parallel R-C element (C).

When the resistor and capacitor are connected in series (Figure 2-7A), the overall impedance response has both real and imaginary components. The impedance of the capacitor will be shifted to the right by the amount equal to resistance and will decrease with increasing frequency. In the case of Figure 2-7B, where the resistor and capacitor are in parallel, the sum of the impedance responses will give rise to a semi-circle in the complex Z^* plane (West, 1987). If a series resistor is added to the latter, the impedance response will shift to the right, as shown in Figure 2-7C. The maximum of the semi-circle of the parallel R-C element equals $0.5R$ (R is the diameter of the circle) and corresponds to $\omega RC = 1$, where $RC = \tau$ (relaxation time). An idealised example of an EIS spectrum of a SOC modelled with simple resistor-capacitor (R-C) circuits connected in parallel is shown in Figure 2-8. Each R-C component is assigned to a different process (bulk, grain and electrode) occurring within the cell. The assumption is made that the time constants of these R-C circuits differ significantly and the values of the capacitance decrease with increasing frequency. Large capacitances are typically associated with the electrode processes, while intermediate-to-low capacitance values correspond to grain boundaries and bulk components. Irvine et al. (2004) put together a summary of capacitance values and their possible interpretation that can be found in Table 2-1.

Table 2-2. Capacitance values and possible interpretation (Irvine et al., 2004).

Capacitance (F)	Phenomenon Responsible
10^{-12}	Bulk
10^{-11}	Minor, second phase
10^{-11} - 10^{-8}	Grain boundary
10^{-10} - 10^{-9}	Bulk ferroelectric
10^{-9} - 10^{-7}	Surface layer
10^{-7} - 10^{-5}	Sample-electrode interface
10^{-4}	Electrochemical reactions

An idealised example of an EIS spectrum of a SOC can be modelled with simple resistor-capacitor (R-C) circuit connected in parallel to form a semi-circle in the Nyquist plot as shown in Figure 2-8.

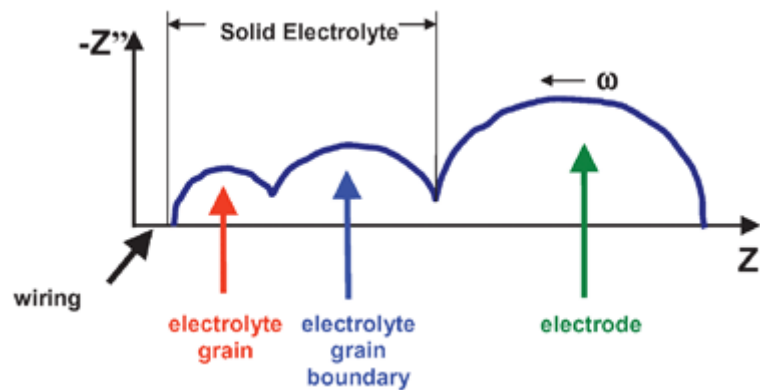


Figure 2-8. An idealised EIS spectrum of SOC showing from grain, grain boundary and electrode resistance contributions (Tuller et al., 2009).

Another element that is often used to fit the impedance data is constant phase element (CPE or Q). The impedance of a constant phase element can be expressed as:

$$Z_{CPE} = \frac{1}{Q(j\omega)^n} \quad (2.24)$$

where Q is the CPE parameter and n is the CPE exponent with value $0 < n < 1$. If n is 1, then the element behaves as a capacitor with capacitance, Q . However, when the exponent is less than 1, the element behaves as an imperfect or “leaky” capacitor. In a parallel R-CPE element, the value of n determines the semi-circle depression (Diard et al., 2013).

2.5 Raman spectroscopy

The theoretical predictions of the inelastic scattering of light date back to 1923 (Smekal, 1923) however, it was in 1928 that the first experimental observations were reported by Indian physicists C. V. Raman and K. S. Krishnan (Raman and Krishnan, 1928) in liquids and independently G. Landsberg and L. Mandelstam in solids (Landsberg, 1928). The inelastic scattering is often called Raman scattering (or the Raman effect) after one of its discoverers.

When photons are scattered by an atom, molecule or crystal, most of the photons will scatter elastically (Rayleigh scattering), resulting in the scattered photon of the same energy, frequency (ν_0) and wavelength as the incident photons. Only a small fraction of photons (approximately 1 in 10^7) will scatter inelastically and will carry the specific information about the vibrational modes in a sample.

In the last few decades with the advances in optoelectronics and development of compact, high-power lasers and sophisticated detectors and optical filters Raman spectroscopy (RS) has become widely used in many research fields.

2.5.1 Fundamentals

RS is an optical vibrational spectroscopy technique based on the inelastic scattering of monochromatic light, typically from a laser in the visible, near-IR or near-UV range, by matter. Although, the present work focuses on Raman scattering in solid states¹, the classical theory of the Raman effect is referred to a molecule.

When the laser light impinges upon a molecule, it interacts with the electron clouds as well as the bonds of the atoms in the molecule, exciting it from the ground state to a virtual energy state. The molecule then relaxes by the emission of photons. If the energy of the photon is the same as that of the exciting radiation then it has undergone an elastic Rayleigh scattering. The principles of Rayleigh and Raman scattering are illustrated in Figure 2-9.

¹ Raman spectroscopy of solids involves the excitation of an electron by the incoming photon causing photon-electron and electron-lattice interactions.

Inelastic Raman scattering occurs when there is an energy transfer between the photon and the molecule, resulting in the shift in wavelength that provides the chemical and structural information, also known as Raman shift. It is often expressed in wavenumbers as it is linearly related to photon energy and makes Raman spectrum independent of the excitation wavelength. However, the intensity of Raman scattering depends on the reciprocal of the fourth power of the excitation wavelength (McCreery, 2005). The Raman shift can be obtained and converted into a wavenumber, the dimension of reciprocal length (cm^{-1}) as below:

$$\bar{\nu}(\text{cm}^{-1}) = \left(\frac{1}{\lambda_0} - \frac{1}{\lambda_1} \right) \times \frac{(10^7 \text{nm})}{(\text{cm})} \quad (2.25)$$

where $\bar{\nu}$ is the Raman shift, λ_0 is the laser excitation wavelength and λ_1 is the Raman spectrum wavelength.

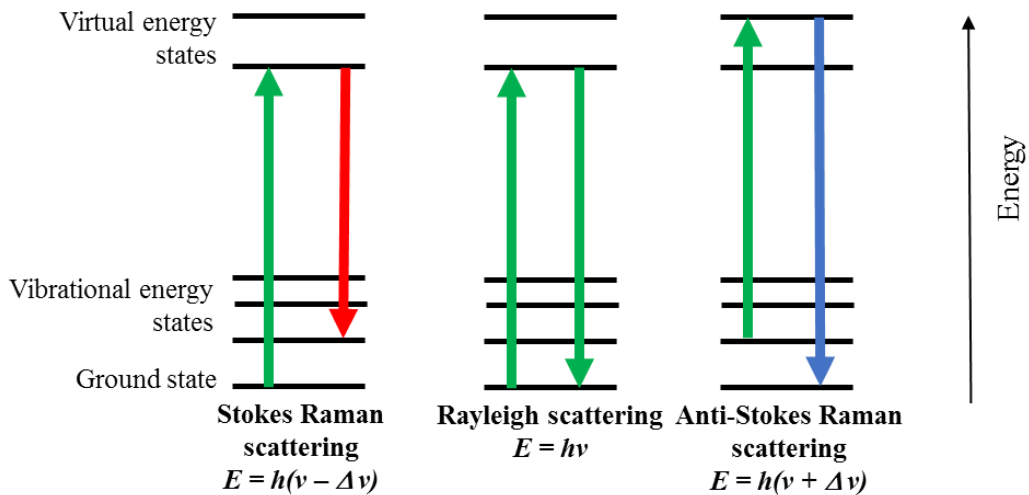


Figure 2-9. Principles of Rayleigh and Raman scattering. E is the energy of a photon, h is Planck's constant, ν is the excitation frequency and $\Delta\nu$ is the frequency change.

The photons will either lose energy to the molecule (Stokes scattering) or gain energy if the atoms in the molecule were already in a vibrationally excited state (Anti-Stokes scattering). The latter process will have a lower intensity compared to Stokes because at ambient temperature most of the atoms are in the ground state as opposed to the higher energy vibrational state. At a given temperature the population of the Stokes and Anti-Stokes components follow the Boltzmann distribution:

$$N \propto e^{-\frac{E}{k_B T}} \quad (2.26)$$

The Raman scattering occurs only when there is change in the molecular polarizability, α , (deformation of the electron cloud) with respect to the vibrational coordinate, q :

$$\frac{\partial \alpha}{\partial q} \neq 0 \quad (2.27)$$

The oscillating electric field of the incident radiation, \vec{E} , induces the polarisation, \vec{p} , in the molecule:

$$\vec{p} = \alpha \vec{E} \quad (2.28)$$

The incident electric field has a sinusoidal form and governed by the electromagnetic frequency of the laser, ν_0 , and the amplitude of the electric field, \vec{E}_0 :

$$\vec{E} = \vec{E}_0 \cos 2\pi \nu_0 t \quad (2.29)$$

According to the principles of quantum mechanics only certain vibrational frequencies and atomic displacements are allowed; the fundamental vibrations in a non-linear molecule are $3N-6$ and $3N-5$ for linear molecules.

Raman spectroscopy is often considered to be complimentary technique to the infrared spectroscopy (IR). The selection rules determine which vibrations will be Raman active; these are summarized below (Ferraro et al., 2003):

- For a vibration to be IR-active, there must be a change in the electric dipole moment, whereas for a Raman-active vibration the change in polarizability during the vibration is necessary.
- The vibration can be IR-active, Raman-active, or both; generally, symmetric vibrations cause largest changes in polarizability, resulting in strong Raman scattering.
- The asymmetric and bending vibrational modes tend to be strong in IR spectroscopy.
- The mutual exclusion rule dictates that no normal modes are both IR and Raman-active if a molecule possesses a centre of symmetry.

Generally, the polar bonds provide intense IR absorption bands whereas the nonpolar bonds, such as C-C, C=C, S-S, N=N, and others, are commonly observed in Raman

spectrum (Reichenbacher and Popp, 2012), making Raman spectroscopy an ideal technique for characterisation of carbonaceous deposits.

2.6 Current uses of Raman spectroscopy in SOCs

Since the introduction of lasers, Raman spectroscopy has been picking up pace. It is non-invasive and can provide information about molecular and structural composition, secondary structures and crystallinity. Below are some of the examples of using Raman spectroscopy for SOCs.

- Carbon deposition.

In-situ and *operando* Raman spectroscopy has been used extensively to study carbon deposition on the surfaces of SOCs fuel electrodes (Kirtley et al., 2013, Pomfret et al., 2008a, Eigenbrodt et al., 2011, Pomfret et al., 2006, Pomfret et al., 2010b, Pomfret et al., 2012). Nickel is often used in combination with an ionic conductor to form a cermet since it is inexpensive and has high catalytic activity (Rossmeisl and Bessler, 2008). However, nickel is a catalyst to a number of unfavourable side reactions, such as Bosch (2.30), Boudouard (2.31) and the thermal decomposition of methane (2.32) to form hydrogen. All three reactions result in carbon formation on the fuel electrode.



Both ordered (G) and disordered (D) graphite formations have been observed via Raman spectroscopy during operation on hydrocarbon fuels (Eigenbrodt et al., 2011, Pomfret et al., 2012). The fundamental G-band is the signature of graphitic sp²-bonded carbon atoms, whereas the D-band is associated with the presence of defects or impurities within the honeycomb network (Maher et al., 2013). The ratio of G and D formation was affected by the total exposure time, cell potential and fuel atmosphere composition (Pomfret et al., 2008a).

Operando Raman spectroscopy is particularly powerful when studying novel electrode materials and their tolerance towards carbon formation. For example, gadolinium-doped ceria (GDC) has been observed to suppress carbon formation in CO₂/CO gaseous environments (Maher et al., 2010).

- Sulfur poisoning.

The effects of H₂S poisoning on Ni-YSZ cermets have been studied extensively under various operating conditions (Zha et al., 2007, Cheng et al., 2011). Sulphur species, present in fossil fuels, readily adsorb onto the Ni surface, blocking active reaction sites and causing cell performance to gradually deteriorate. The extent of degradation is dependent on the concentration of the contaminant, cell voltage and temperature (Zha et al., 2007). Raman spectroscopy has been employed to observe the formation of Ni₃S₂ species, however, at temperatures above 565 °C, Ni₃S₂ undergoes a transition from a low-temperature rhombohedral phase to the high temperature cubic phase and the Raman spectrum becomes less defined (Cheng et al., 2007).

Moreover, lanthanum strontium manganite (LSM) and lanthanum strontium cobalt ferrite (LSCF) air electrodes are susceptible to sulphur poisoning by SO₂-containing air, causing the formation of SrSO₄, which is Raman active (Wang et al., 2015, Liu et al., 2011).

- Chromium poisoning.

Chromia-forming alloys are commonly used as SOC stack interconnects and can form volatile Cr-species under IT-SOC operating conditions which react with air electrode materials (Jiang et al., 2002). Under cathodic polarisation, LSM is susceptible to the formation of Cr₂O₃ and (Cr,Mn)₃O₄ spinel at the electrode/electrolyte interface region and on the electrolyte surface (Jiang et al., 2000). In the case of LSCF, Cr deposition occurs predominantly on the surface of the electrode, forming SrCrO₄ spinel and segregated SrO (Wei et al., 2015).

2.7 Experimental reactor considerations

Traditionally, the electrochemical performance of fuel cells is monitored by the means of electrochemical impedance spectroscopy and cyclic voltammetry. These dynamic techniques provide powerful insight into the various electrical losses and reaction kinetics but lack the information about mechanical and chemical degradation. For a comprehensive study, the microstructure is evaluated *post mortem* using a combination

of SEM/EDS and other surface analysis techniques such as X-ray photoelectron spectroscopy (XPS), Auger electron spectroscopy (AES) and secondary ion mass spectroscopy (SIMS). However, secondary processes and reactions are likely to occur on cooling, affecting the final condition of the sample (e.g. structural and phase transformations, oxidation reactions).

Recently, Raman spectroscopy has been used as a tool for *in situ* characterisation of operational SOCs (Eigenbrodt et al., 2011, Kirtley et al., 2014, Pomfret et al., 2006, Pomfret et al., 2010a, Duboviks et al., 2014, Maher et al., 2013). The technique is particularly sensitive to carbon formations, often observed on nickel-containing cermets but can also be used to study metal oxide redox kinetics, sulphur and chromium poisoning and measure the residual stress (Onuki et al., 2013, Onodera et al., 2013, Nagai et al., 2011).

Typical operating temperatures of SOCs range from 600 °C to as high as 1000 °C (Nehrir and Wang, 2009) and therefore, considerably limit the material selection for constructing the experimental setup. Off-the-shelf SOC test assemblies are typically limited to electrical connections only, therefore, to measure molecular vibrations significant design modifications are needed. Alternatively, custom made testing reactors can be fabricated to accommodate *operando* measurements.

In the literature, two different types of reactor design have been reported up to now: a miniaturised heated stage that fits under the microscope (Blinn et al., 2012, Brightman et al., 2012a) and a much larger assembly consisting of an alumina tube inside a closed-end quartz tube positioned inside a tube furnace with custom built optics (Pomfret et al., 2010a). All three examples are illustrated in Figure 2-10.

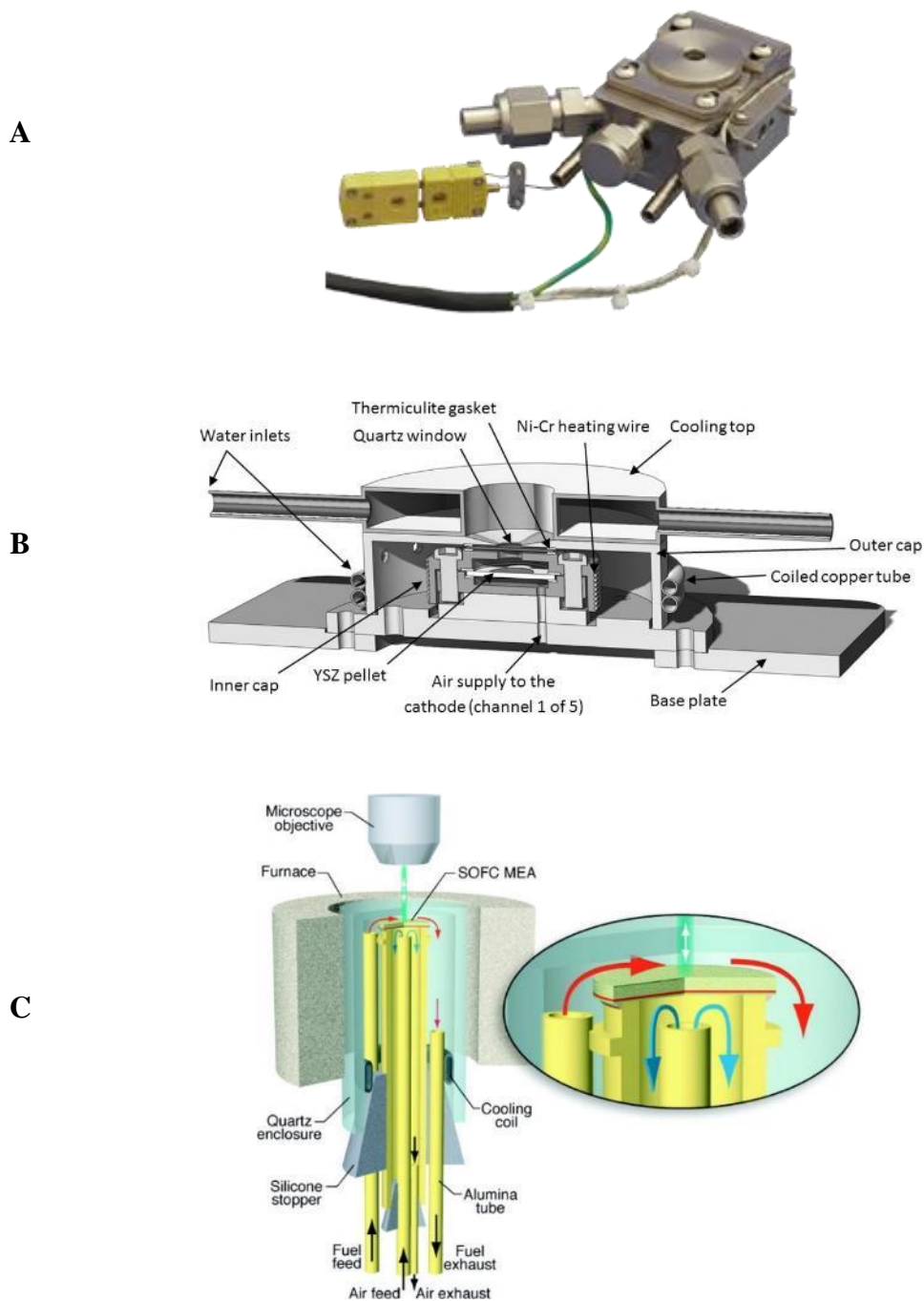


Figure 2-10. (A) Photograph of a Raman high temperature reaction chamber, HVC-MRA-5, made by Harrick Scientific Products (Harrick Scientific Products Inc, 2012), (B) Brightman (Imperial College London) (Brightman et al., 2012b) and (C) Pomfret (Montana State University) (Pomfret et al., 2008b).

Besides featuring simultaneous electrochemical and optical measurements, and fully controllable dual atmosphere, both bespoke designs have their own strengths and experimental challenges as listed in Table 2-3.

Table 2-3. A summary of pros and cons of the reported designs.

	Miniaturised Stage	Large-scale rig
Pros	<ul style="list-style-type: none"> Compact design 2D mapping capabilities Rapid cooling Accommodates various sample sizes 	<ul style="list-style-type: none"> Higher operational temperature Easy part replacement Chemically resistant materials
Cons	<ul style="list-style-type: none"> Height limited to <10 cm Temperature stability above 650 °C Extensive water cooling of the components Cramped design to accommodate all connections 	<ul style="list-style-type: none"> Custom optics Single sampling position Slow heating/cooling profile

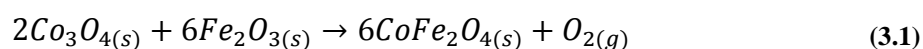
3 Experimental

This chapter outlines the material synthesis and sample preparation, experimental measurement setup and operating parameters used for electrochemical and spectroscopic characterisation, the equipment used to perform these measurements and the examples of data analysis. In this work two types of samples were tested: solid oxide cells (SOCs) and pressed powder pellets.

3.1 Sample Preparation

3.1.1 Solid State Powder Synthesis

CoFe₂O₄ was synthesised using the conventional solid-state route to produce a 20 g batch, as shown in a flowchart in Figure 3-1. The precursor powders of Co₃O₄ (Alfa Aesar, 99.7%) and Fe₂O₃ (Sigma-Aldrich, ≥ 99%) were dried at 600 °C for 8 hours and cooled down to 200 °C before being transferred to a vacuum desiccator to prevent moisture absorption on cool down. The oxide powders were weighed out in stoichiometric ratios using a high accuracy analytical balance (Precisa Instruments AG, 0.1 mg), according to reaction (3.1) and ball milled together using yttria-stabilised zirconia (YSZ) grinding media in isopropanol (IPA) for 6 hours.



The slurry was dried in an oven at 85 °C to evaporate the solvent before being sieved through a 250 µm sieve and calcined in a zirconia crucible at 900 °C for 2 hours in a static

air atmosphere. This process was repeated three times to achieve homogeneous, agglomerate-free, single-phase cobalt ferrite powder.

Both precursor and as-prepared powders were analysed by X-ray powder diffraction (D2 Phaser, Bruker AXS) using Cu K α ($\lambda=1.5406 \text{ \AA}$) to ensure the single phase formation of CoFe₂O₄.

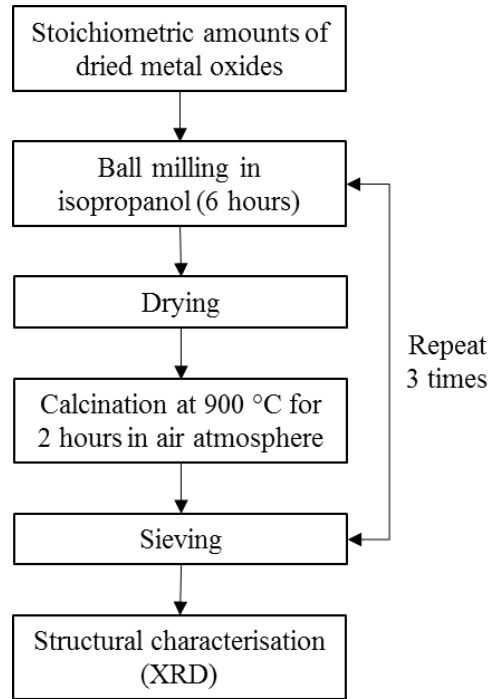


Figure 3-1: A flow chart of solid state powder synthesis adopted from Xiang et al. (2014).

3.1.2 Pellet Preparation

A laboratory uniaxial hydraulic press (Specac, UK) was used to form pellet compacts. The powder samples were compiled in two different geometries in preparation for sintering and testing: 10 mm ϕ cylinders and 20 x 4.5 mm cuboid-shape bars. 0.3 ton pressure was applied onto the pellet die for 1 minute.

3.1.3 Solid Oxide Cell Fabrication

A typical SOC has three components: an electrolyte, a fuel electrode, and an air electrode. 20 mm ϕ HionicTM button substrates (FuelCellMaterials, USA) were used as electrolytes for the cell preparation (Lot #: BB112). The approximate composition of the substrates is listed in Table 3-1. The specific composition remains proprietary information of the manufacturer.

Table 3-1: List of ingredients of Hionic™ electrolyte substrates (Nexceris LLC, 2015).

Chemical Name	Percentage Weight (%)
Zirconium Oxide	85-96
Scandium Oxide	4-14
Cerium Oxide	0-3
Hafnium Oxide	1-2
Aluminium Oxide	0-1

These state-of-the-art substrates benefit from higher conductivity and enhanced mechanical strength compared to other conventional electrolytes like yttria- or scandia-stabilised zirconia (fuelcellmaterials.com, 2007). The thickness of the electrolytes ranges between 0.13-0.17 mm. Such thin electrolytes are obtained by a technique called tape casting (also known as doctor blading) that was originally used for manufacturing thick film tape materials for electronic applications (Singhal and Kendall, 2003). Today it is used extensively to produce thick ceramic tapes from ceramic slurry that is then dried, laminated and sintered to produce a final substrate product.

NiO-YSZ ink (FuelCellMaterials, USA) was used for SOC's fuel electrodes. The ink formulation contains 66 wt% of NiO and 34 wt% of $Y_2O_3-ZrO_2$, and the total solid loading did not exceed 77 wt%.

LSM-YSZ and LSM inks for the oxygen electrode were prepared in-house from commercial powders (FuelCellMaterials, USA). The ceramic slurry contained the following components mixed together using a high speed mixer (SpeedMixer™, DAC 800 FVZ):

- Ceramic powder: LSM or LSM-YSZ (50-50 wt%)
- Dispersant: Triton™ X-114
- Binder: Ethyl cellulose
- Solvents: Texanol™ ester alcohol, isopropanol
- Screen Printing

A simple and economical screen printing technology can be applied to planar SOCs to fabricate films of different thicknesses. There are three main steps to cell fabrication using screen printing: (i) covering the pattern on the screen with the ink, (ii) applying tangential stress on the ink using a squeegee and (iii) passing ink through the aperture of

the screen mesh. The SOCs are fabricated in two sintering steps as shown in Figure 3-2. Firstly, a 10 mm \varnothing NiO-YSZ cathode is screen printed onto the surface of the electrolyte, dried at 100 °C for 10 min and sintered at 1350 °C for 2 hours in static air. This is followed by deposition of the LSM-YSZ anode and LSM current collector, then drying and sintering at 1150 °C for 2 hours. The cells are printed one at a time to ensure accurate alignment of the cathode and anode layers.

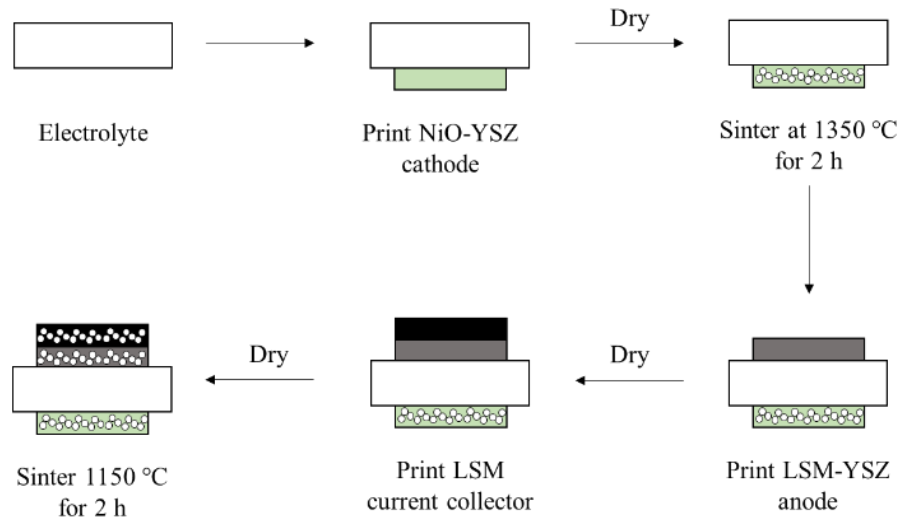


Figure 3-2: Schematic of electrolyte-supported SOC fabrication.

Fonseca et al. (2006) studied the effect of sintering time on the electrical conductivity of Ni-YSZ cermets and showed an optimum electrical conductivity σ ($T = 400$ °C) for up to 2 hours of sintering. Therefore, 2 hours sintering time was chosen for SOC electrodes.

3.2 Sample Characterisation

3.2.1 Density measurements

The density of the pellets was measured using an analytical balance (Mettler-Toledo AG, MS104S) and compared to the theoretical density reported in the literature. The density of the solid was calculated using formula in the equation (3.2).

$$\rho = \frac{A}{A - B} (\rho_o - \rho_L) + \rho_L \quad (3.2)$$

where:

ρ = density of the sample,

A = weight of the sample in air,

B = weight of the sample in the auxiliary liquid,

ρ_o = density of the auxiliary liquid,

ρ_L = density of air (0.0012 g/cm³).

3.2.2 X-ray Diffraction

Powder X-ray diffraction (XRD) was used to obtain the diffraction patterns of the powders and ceramics used in this project. All crystalline materials have a unique diffraction pattern that can be identified using a crystallographic database. This allows for the phase purity, composition, and presence of impurities in crystalline solids to be identified. The lattice parameters of a unit cell associated with a crystal structure can be determined using the Rietveld refinement method (Smith et al., 2013).

The position of diffraction peaks is determined by the distance between parallel planes of atoms. Equation (3.3) expresses the relationship between the wavelength of the incident X-ray, incident angle and the spacing between the crystal lattice planes of atoms, also known as Bragg's law. The geometric derivation of Bragg's law is illustrated in Figure 3-3.

$$n\lambda = 2d \sin\theta \quad (3.3)$$

where:

θ is the angle of incident X-ray,

n is an integer (order of diffraction),

λ is the wavelength of the radiation used,

d is the spacing between atomic layers.

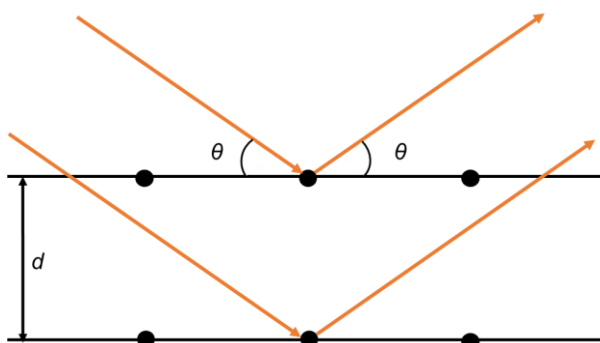


Figure 3-3. Bragg's law reflection.

A typical powder sample contains tens of thousands of randomly arranged crystallites in every possible orientation, hence the incident monochromatic X-ray beam is diffracted at all possible Bragg angles. The detector moves around the sample in a circle to collect the diffraction pattern at different 2θ angles, as shown in Figure 3-4.

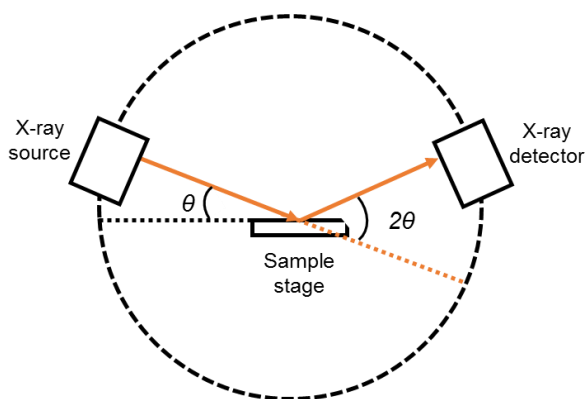


Figure 3-4: Schematic diagram of X-ray diffractometer.

3.2.3 Sample Preparation

To confirm the phase purity of the samples, a desktop X-ray diffraction tool (D2 Phaser, Bruker) was used to perform an initial measurement. The measurements were collected in the range of $10 - 100^\circ$ (2θ) using Cu $K\alpha$ radiation ($\lambda = 1.54056 \text{ \AA}$) with a 0.02° step size and a scan time of 0.1 s. The resulting patterns were analysed using the PDF-4+ database.

For lattice parameter refinement and quantitative information about the phase of material, a STOE-STADI PSD diffractometer (Mo $K\alpha$, $\lambda = 0.70926 \text{ \AA}$) was used. The samples were prepared by grinding up small amounts of CoFe_2O_4 and Si (as an internal standard) using a pestle and mortar. The mixed powders were placed onto the acetate disc with a drop of PVA glue used to hold the loose powders. The resulting disc was then dried using

a heat gun to speed up the drying process. The discs were scanned for 4 hours in 2θ range of 5 to 45° . The internal Si standard was used to calibrate the data to the known peak positions of Si using the STOE WinXPow software. Rietveld refinement was performed to obtain lattice parameters, crystallite size and strain, and in some cases the amount of secondary phase within a sample.

3.2.4 Thermogravimetric Analysis

Thermogravimetric analysis (TGA) was used to measure the amount of weight change of the sample as a function of temperature and isothermally, as a function of time. The samples were heated and cooled at a constant rate of $5^\circ\text{C}/\text{min}$ in a controlled atmosphere under a flow of nitrogen or air. Once the temperature set point was reached, the samples were allowed to dwell for 2 – 4 hours and slowly cooled down.

In this work a TA Instruments STA Q600 simultaneous thermal analyser was used to collect the weight change (TGA) and true differential heat flow (DSC) information on the same sample. Approximately 50 mg of sample was analysed in a platinum crucible to prevent adverse reaction of cobalt iron oxide with an alumina crucible.

3.2.5 Thermoelectric Measurements

The electrical conductivity, σ , and Seebeck coefficient, S , of the CoFe_2O_4 bar samples were determined simultaneously for the temperature range of $50 - 700^\circ\text{C}$ using a SBA 458 Nemesis® thermal analyser (NETZSCH-Gerätebau GmbH, Germany).

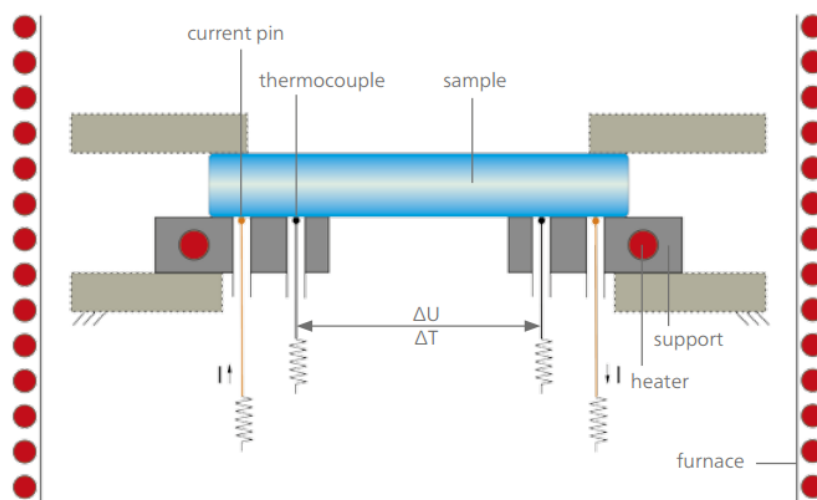


Figure 3-5: Measurement setup of the Netzsch SBA 458 Nemesis® (NETZSCH, n.d.).

The electrical conductivity of the sample is determined by a 4-point method using two current pins and two thermocouples positioned on the sample edges as shown in Figure 3-5. The current is supplied through the two outer probes resulting in the voltage drop between the two inner probes. The electrical resistance, R , is calculated from voltage, V , and current, I , using Ohm's law:

$$R = \frac{V}{I} \quad (3.4)$$

The resistance of the sample depends on its length, l , cross-sectional area, A , and resistivity, ρ . Resistivity is an intrinsic property of the material and can be calculated using the formula in (3.5):

$$\rho = R \frac{A}{l} \quad (3.5)$$

Electrical conductivity is the reciprocal of resistivity and follows (3.6):

$$\sigma = \frac{1}{\rho} \quad (3.6)$$

The Seebeck effect is best described as an electrical potential difference produced by a temperature difference between a pair of points of an electrically conducting sample. A thermal gradient is applied to the sample in both directions by two micro heaters creating hot and cold 'junctions'. The electrons on the hot side have more kinetic energy causing them to migrate towards colder side of the sample, therefore creating a charge gradient. The measure of the magnitude of the thermoelectric voltage in response to a temperature gradient across the sample is called the Seebeck coefficient. The Seebeck coefficient of a material is defined as:

$$S = \frac{\Delta V}{\Delta T} \quad (3.7)$$

Depending on the charge carriers the Seebeck coefficient values can be positive or negative. If the carriers are positively charged (electron holes), the material is a p-type conductor with a positive value for Seebeck coefficient. Conversely, if the carriers are negatively charged (electrons), the material is an n-type conductor and the Seebeck coefficient will be negative.

During the measurement, both electrical conductivity and Seebeck coefficient are measured at room temperature to ensure good contacts between the sample and the measuring probes. The temperature is then raised to 50 °C at 2 °C/min; the measurements

are then performed at intervals of 50 °C on heating and at 100 °C intervals on cooling to check for the reproducibility of the results.

3.2.6 Raman spectroscopy

The theoretical background of Raman spectroscopy is covered in Chapter 2. The Raman spectroscopy measurements were performed using an inVia™ Raman microscope (Renishaw Plc., UK). An argon ion laser was used as an excitation source (514 nm, 20 mW). A schematic diagram of the components present in a typical Raman microspectrometer is shown in Figure 3-6. The laser beam travels towards the sample through the microscope directed by mirrors. When the laser excitation interacts with the sample both Raman and Rayleigh scattering are collected by the microscope lens travelling towards charge-coupled device (CCD) detector. The notch filter blocks the Rayleigh scattering (same wavelength as the laser line) focusing the filtered Raman scattering onto a diffraction grating that splits the beam into its constituent wavelengths that are then picked up by the detector and processed by the computer.

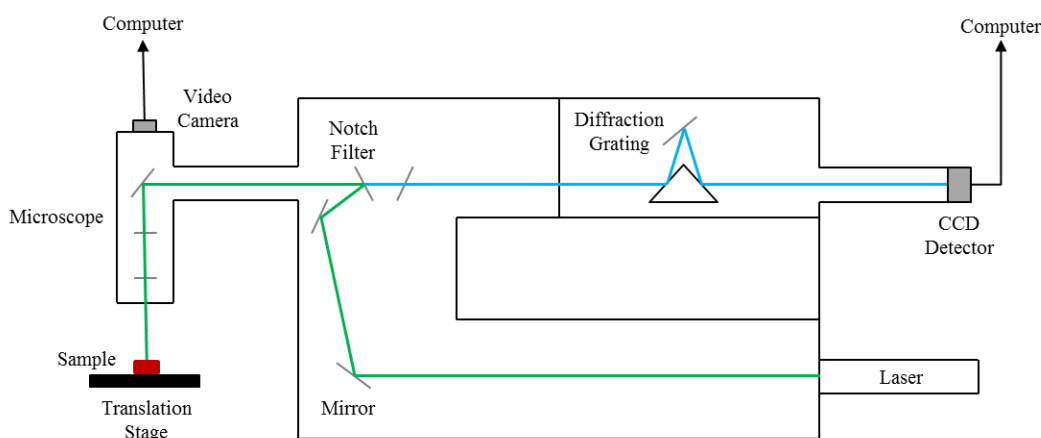


Figure 3-6: A simplified schematic of a Raman microscope.

A number of objectives were used to focus and collect Raman spectra from the surface of a sample. For *in situ* and *operando* measurements a 20X long working distance objective (20 mm working distance, 0.42 numerical aperture) was used. The longer focal length of the objective protects it from the high operating temperatures of SOCs; however, the lower numerical aperture value means that less signal is collected. The room temperature Raman spectra were collected at close proximity, using a 50X microscope objective (0.38 mm working distance, 0.75 numerical aperture). Such measurements are often referred

to as *ex situ* or post-mortem. The 50X objective gave a laser spot of approximately 1 μm diameter. To obtain high intensity Raman spectra with low background noise and clearly defined peaks, the exposure time was increased between 10 – 60 s.

The inVia™ system has two grating scan types: static and extended (SychroScan). Static scan covers a range of approximately 300 cm^{-1} either side of the centre (depending on the laser wavelength and grating used) and is quick to perform. The spectra can be collected in as little as 1 s, making it ideal to study the kinetics of reactions. Extended scans, on the other hand, allow a wider wavenumber range to be covered but take longer to obtain. Apart from the *operando* studies, where 20 s static scans were used to monitor carbon formation on the surface of a nickel electrode, extended scans were performed to inspect the full range of Raman shift for changes or abnormalities. The exposure time was normally between 10 and 30 s, unless stated otherwise. Wire 3.4 software was used to collect and analyse the Raman spectra.

3.2.7 X-ray photoelectron spectroscopy

The powdered samples were all mounted by pushing the loose powders into indium foil, which was itself then adhered to the sample holder. The polished pellet samples were supported on double sided carbon tape on the sample holder.

The analyses were carried out using a Kratos Supra instrument with the monochromatic aluminium source, with two analysis points per sample. Survey scans were collected between 1200 to 0 eV binding energy, at 160 eV pass energy and 1 eV intervals. High-resolution O 1s, C 1s, N 1s, Fe 2p and Co 2p spectra were collected over an appropriate energy range at 20 eV pass energy and 0.1 eV intervals. Charge neutralisation was used for all samples. The analysis area was 700 μm by 300 μm .

The data collected was calibrated in intensity using a transmission function characteristic of the instrument (determined using software from NPL) to make the values instrument independent. The XPS spectra were deconvoluted using CasaXPS software.

3.2.8 Scanning Electron Microscopy

Scanning electron microscopy (SEM) is a high resolution surface technique used for the topographical, microstructural and bulk composition analysis of the sample. SEM is based on scanning a fine beam of electrons over the specimen surface and detecting the emitted signal. When the high energy electrons hit the sample, a number of signals is emitted, namely, secondary electrons, backscattered electrons and X-rays, see Figure 3-7:

- Secondary electrons are emitted by the atoms near the specimen surface that are excited by the incident beam and gain enough energy to detach from the surface.
- Backscattered electrons are high energy electrons that are emitted by an elastic collision of an incident electron with the sample atoms. The advantage of the backscattered electrons is that they are sensitive to the atomic mass of the atomic nuclei they have collided with and scattered from. Heavier elements are more efficient at backscattering and, therefore, appear brighter on a backscattered electron image. Similarly, lighter elements will appear darker.
- X-rays are generated when the electron beam interacts with the atoms in the sample causing shell transitions. The characteristic energy of the generated X-rays can be used for qualitative and quantitative analysis of the elemental composition of the specimen.

A schematic diagram of a typical SEM is shown in Figure 3-8. The filament of the electron gun at the top of the microscope generates a beam of electrons in a vacuum chamber. The beam is focused through a number of condensers and objective lenses set parallel to each other onto the sample. The electrons are collected by the scanning electron (SE) or back-scattered electron (BSE) detector that transforms them into a signal that is then digitized to produce an image.

Unlike other microscopes, the image magnification in SEM depends on the excitation of the scan coils and not the power of the objective lens. To change the magnification, the size of the raster area on the sample needs to be changed. The size of the monitor raster pattern remains constant. The magnification is increased by reducing the size of the area scanned.

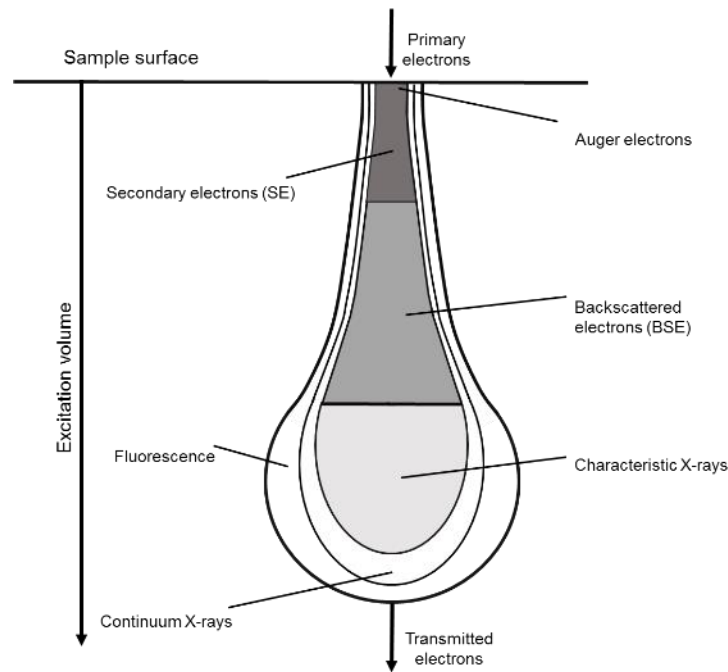


Figure 3-7: Electron beam interaction with the bulk of the sample.

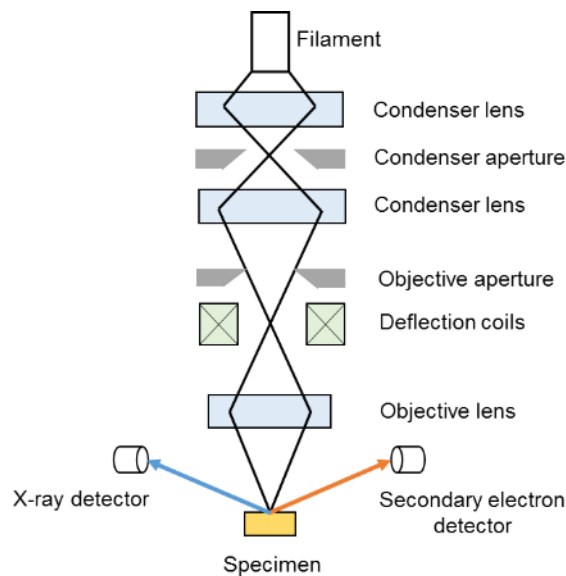


Figure 3-8: Schematic diagram of an electron microscope with SE and X-ray detectors.

3.2.8.1 Sample Preparation

The sample preparation differs considerably depending on the type and geometry of the material under study.

(i) *Powder samples* were prepared by placing a carbon tape on the sample stub and dipping it in powder. The loose powder was swept away by spraying with compressed air. The last two steps were repeated until a desired coverage was achieved.

(ii) *Sintered bar samples* were polished manually by grinding the surface on a range of silicon carbide papers for approximately 3 minutes starting from grit P600 and going up to grit P2500. The sample surface was cleaned with water and acetone after each polishing step. A 1 μm diamond emulsion was added to the final round of polishing. The samples were then etched at 90% of the sintering temperature for 30 minutes to reveal the microstructure.

(iii) *For SOC*s, after operation, the SOC electrodes are electrically conductive and will give an SEM image. The cell was broken in half to reveal the cross-section and mounted onto a stub using silver paste. For better quality imaging, a thin layer of gold was applied by sputter coating. When elemental analysis was carried out alongside imaging, using energy dispersive X-ray spectroscopy (EDS), carbon coating was used instead of gold.

3.3 Electrochemical Testing

A diagram of a test station used for *in situ* and *operando*² testing of SOC_s is shown in Figure 3-9. The setup allows flexible control over the operating temperature, humidity levels, and flow rates of the gases. The test conditions can have a dramatic effect on the overall performance of a cell and its lifetime, therefore, where possible, steady state must be reached and the test conditions noted. For SOC, steady state refers to when the current/voltage reading does not change with time. Often, to ensure that the steady state is reached, the system is left to equilibrate for a period of time with a set temperature and gas composition whilst monitoring the open-circuit voltage (OCV).

² *Operando* testing refers to simultaneous *in situ* electrochemical and Raman spectroscopy measurements.

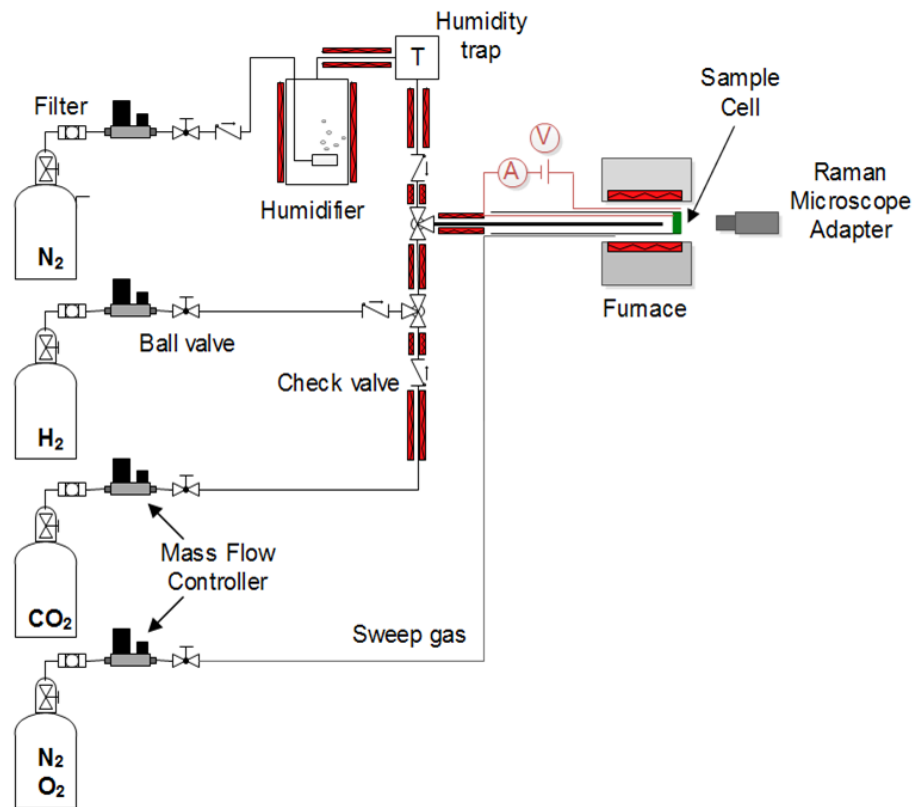


Figure 3-9: Solid oxide cell test station with optical access for Raman microscope.

The following instruments are part of the SOC test station:

- Bronkhorst® EL-Flow Select Series mass flow controllers for nitrogen, hydrogen, carbon dioxide, carbon monoxide and synthetic air (a 20% mixture of oxygen in nitrogen) with $\pm 0.5\%$ reading error of the actual flow plus $\pm 0.1\%$ full-scale flow error.
- Elite Thermal Systems Ltd tube furnace (TSU11/50/250) with a Eurotherm 2416 proportional-integral-derivative (PID) controller and a RS232 digital communication module to transmit and receive data from iTools Engineering Studio software.
- TC-08 Data Logger (Pico Technology, UK) used to record the temperature from a K-type thermocouple placed on the outside of the operating SOC. The temperature accuracy of data logger is $\pm 0.2\%$ of reading and $\pm 0.5\text{ }^\circ\text{C}$ of full scale error.
- Modulab® ECS electrochemical interface and frequency response analyser (Solartron Analytical, UK) with internal XM Booster 2A for ultra-low, micro-ohm impedance testing.

- Electrochemical testing apparatus built at the University of Sheffield, Department of Chemical and Biological Engineering. The design of the apparatus is covered in detail in Chapter 4.

One of the requirements for the testing station was to be easily transportable between laboratories, as the Raman spectrometer used for *operando* work is part of multi-user facility. Therefore, all the equipment was arranged on a 3-tier trolley.

3.3.1 Start-up Procedure

Following the assembly of the test housing, the electrochemical apparatus was placed inside the tube furnace and insulated on both sides to reduce the heat loss to the surroundings. The cell was heated up to 700 °C at 5 °C/min to promote the melting of the glass coating of the hybrid gasket and create a seal created between an alumina support tube, Thermiculite® 866LS and the cell. Slower heating rates minimise the thermomechanically induced stress to the cell and the reactor as a whole and therefore are always more favourable; however, due to time constraints and short testing runs a ramp rate of 5 °C/min was chosen. A flow of 50 ml/min of N₂ over the outside chamber of the reactor was used during heat up to displace the atmospheric oxygen and to prevent steam formation during the reduction step.

Once the temperature is stable, a 50 ml/min flow of H₂ gas is introduced to the cell to reduce the NiO to metallic nickel. The cell is reduced for 30 minutes before synthetic air is flown to the SOEC anode. Open-circuit voltage is monitored whilst the cell is reducing. The initial performance of the cell is assessed by the means of galvanostatic impedance measurement and linear i-V characteristics in fuel cell mode. The operating temperature adjustments are made by heating or cooling the cell down at 1 °C/min to avoid thermal shocks that can lead to cracks in the electrode and failure of the cell.

3.3.2 Solid Oxide Cell Measurements

The cell measurements are performed under ambient pressure operation. One of the main advantages of the SOCs is the fuel flexibility. In this work the references are made to three types of experimental conditions:

- Hydrogen fuel: mixture of H₂ and N₂
- CO₂ electrolysis: mixture of CO₂, CO and N₂

The experimental apparatus described in Chapter 4 was used for SOC characterisation. The rig has a two-electrode configuration used to collect electrochemical impedance,

current-voltage and cyclic voltammetry measurements. The theoretical background of these techniques is discussed in Chapter 2.

A frequency sweep range from 1 MHz to 10 mHz and a current amplitude of 5 mA rms were used to collect the impedance spectra. All EIS measurements were carried out at open-circuit conditions unless otherwise stated.

Cyclic voltammetry was recorded at a 100 mV/s scan rate with 0.5 and 1.5 V vertex levels probing both fuel cell and electrolysis operation modes. Schematic representation of CV experiment is shown in Figure 3-10.

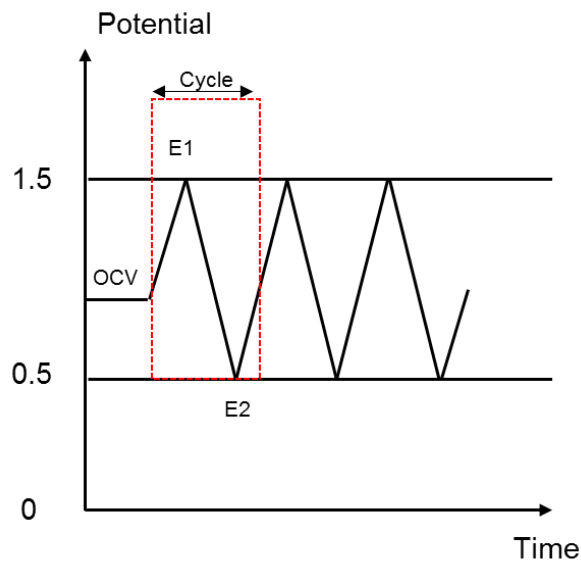


Figure 3-10: Cyclic voltammetry experimental setup.

4 Experimental Apparatus Design and Commissioning

This chapter describes the development of a high temperature spectroelectrochemical system for an extensive analysis of SOC electrode surfaces in real time and under actual operating conditions.

Having looked at the pros and cons of the different SOCs rig designs, summarised in Section 2.7. The larger design offered more opportunities for modifications as and when needed as well as use of off-the-shelf materials to build the assembly. The future aspirations of using the reactor for high temperature co-electrolysis of steam and carbon dioxide meant that the components must be stable to thermal cycling and not react with the gaseous reagents. For this work the development of a large-scale reactor was chosen. This decision was influenced by previous experience of using a commercially purchased versatile ProboStat™ electrochemical cell testing system (NorECs Norwegian Electro Ceramics AS).

4.1 Design of the Test Apparatus

The strategy for the new *operando* Raman spectroscopy apparatus development was to use a combination of already established requirements and advantages of the previously mentioned reactors, namely the stable high temperature operation and two-dimensional surface mapping.

Further specifications for the reactor components that needed to be taken into consideration were:

- General dimensions
- Optical access for Raman spectroscopy
- Gas inlet and outlet ports
- Electrical connections
- Temperature control
- Materials
- Sealing of SOC

The 3D CAD drawing of the initial design is presented in Figure 4-1 and Figure 4-2.

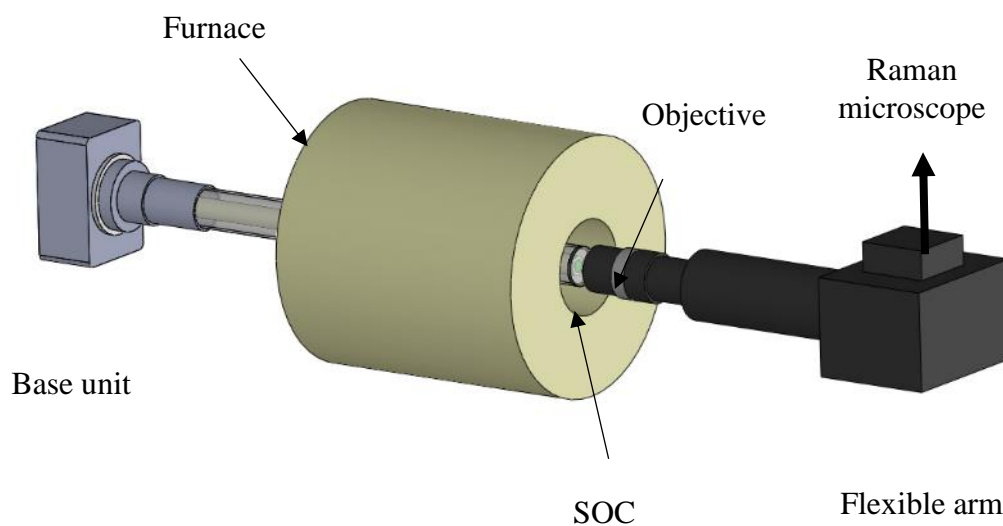


Figure 4-1. Schematic drawing of the test apparatus (Manerova et al., 2015).

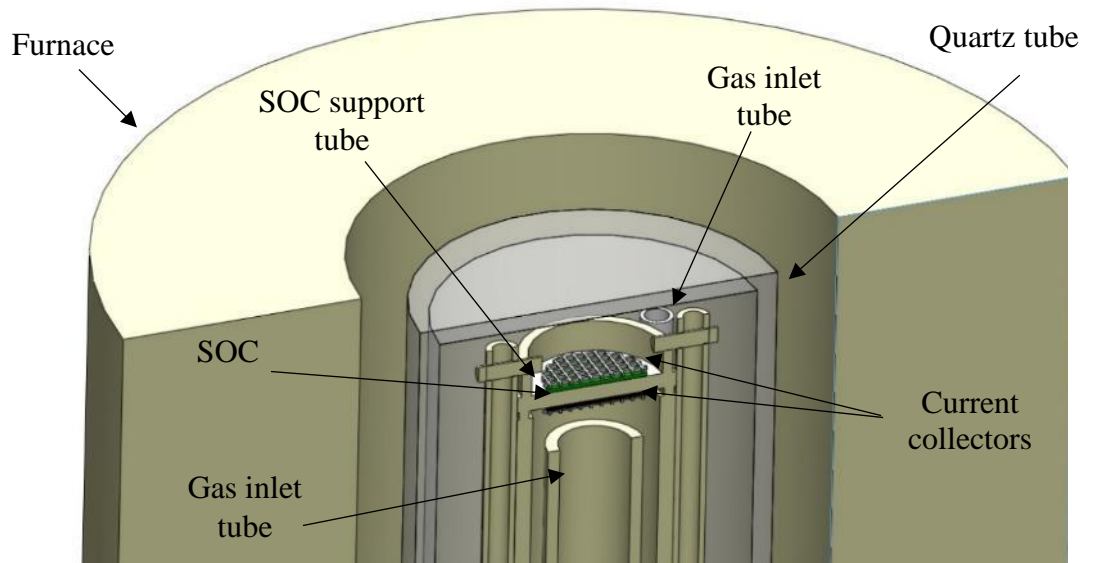


Figure 4-2. Schematic drawing of the detailed cross-section view of the cell housing (bottom)
(Manerova et al., 2015).

4.1.1 General Dimensions

Planar solid oxide cells are usually square, rectangular or circular. Laboratory scale experiments are often carried out on the latter with a diameter of 25 mm or less. In this work 20 mm diameter circular-planar cell were used.

The base unit was designed around a cuboid stainless steel box with 140x100x70 mm dimensions to accommodate gas ports, electrical connections for thermocouple and cell measurements. One of the main advantages of the base unit is the configuration of the electrical connections that prevents the wires from touching each other and other parts of the reactor as well as improving the integrity of the EIS and IV measurements. A heating rope was wrapped around the gas lines and connected to a switch for an added option to heat up the gases on their way to the cell to avoid condensation inside the base unit.

Conventional SOCs require two gas chambers for fuel and oxidant to be supplied separately to the respective electrode. A three-tier extrusion in the shape of a pedestal was used for this purpose as shown in Figure 4-3. There are 6 gold-plated pins and 4 gas ports spread across two levels. Both levels of the pedestal have gas inlet and outlet ports and 2 pins for electrical measurements; however, the lower level has an additional 2 pins for a K-type thermocouple. All of them come out on the sides of the base unit as BNC connectors, thermocouple socket and Swagelok® quick-connect brass couplings.

A cell would sit on a 20 mm outer diameter (OD) alumina tube screwed onto the top of the pedestal using a metal collar glued to it. The temperature of the base unit would not exceed 120 °C, so a wider range of materials can be used. The total length of the reactor is 650 mm, similar to the Probostat™.



Figure 4-3. Three-tier extrusion on the base unit.

A second chamber is created using a flat bottom quartz tube (40 mm OD) with two nitrile O-rings and a stainless steel collar that threads onto the pedestal creating a gas-tight seal as well as holding the tube in place.

It is important for the furnace to be non-inductively wired to prevent interference during electrochemical measurements. Such a tube furnace with a 50 mm bore diameter and a 350 mm single heated zone was used in this work (Elite Thermal Systems Ltd.).

4.1.2 Optical Access

The second most important consideration for the design of this reactor was optical access to collect *in situ* Raman spectroscopy measurements. The Raman microspectrometer used for this work is described in Section 3.2.6. The machine was equipped with a sample stage moving in X, Y and Z directions. A flexible microscope coupling arm was used to redirect the laser beam horizontally and was attached to the XYZ stage using a custom-made accessory, allowing for adjustment of the focus and position on the sample.

Although long distance objectives were used, the space between the sample surface and the microscope objective was less than 25 mm. Therefore, cooling of the objective was vital. Cooling can be achieved using two mechanisms: convection (air cooling) or conduction (water/antifreeze). The convection method was used in this work by employing a coiled copper tube with holes to let the air out, see Figure 4-4.

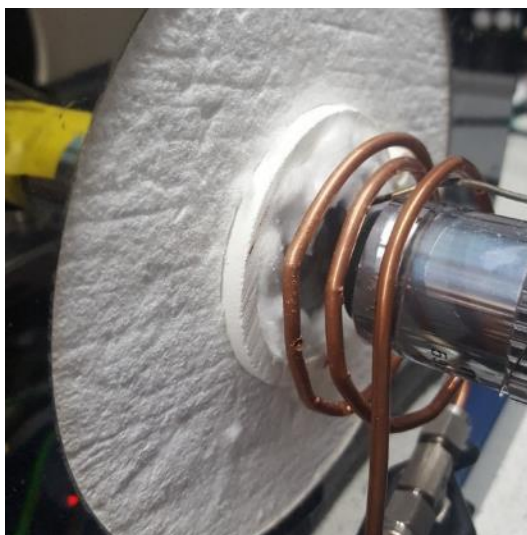


Figure 4-4. Air cooling of microscope objective using coiled copper accessory.

4.1.3 Gas and Electrical Connections

Conventional fuel cell setups have two chambers to keep the oxidant and fuel gases separate, therefore, each chamber contains gas inlet and outlet ports. 1/8" stainless steel tubing was used to connect the ports to female Swagelock® quick-connect fittings on the side of the base unit. The male stem parts with stop valves were secured onto the 1/4" flexible tubing coming from the mass flow controllers or going to the vent to prevent gas flow escaping into the room.

The opposite vertical plane contained a K-type thermocouple socket and the on/off switch heating up the core of the base unit using rope heaters. The positive and negative thermocouple wiring had designated gold-plated feedthroughs on the bottom of the pedestal. Four more feedthroughs were used for electrical measurements, to connect to the leads of electrochemical testing equipment through the base unit's exterior BNC (Bayonet Neill–Concelman) connectors. Platinum wires (0.5 mm \varnothing), connected to the

cell at one end and a female socket at the other end, and were plugged into the feedthroughs making the whole setup robust towards constant reassembly process.

Platinum mesh pressed onto a single platinum wire using a benchtop hydraulic press was used for current collection on both sides of the cell. Prolonged heating and cooling cycles, harsh environments, and reassembly processes resulted in the mesh breaking off at the top, so later gold current collector meshes were screen printed directly onto fuel cell electrodes. For comparison purposes, the electrical connections were also fabricated using gold wire.



Figure 4-5. A side view of the reactor showing gas (left) and electrical (right) connections (GI – gas in, GO – gas out, B1 & B2 – bottom pins, and T1 & T2 – top pins).

4.1.4 Temperature Control

The furnace was equipped with a Proportional-Integral-Derivative (PID) controller for greater control over heating/cooling rates to preserve the reactor components and SOC itself. Rapid temperature changes, combined with the effects of thermal expansion across all the components could induce significant microstructural changes and even cracks inside the multi-layered device. For this reason the heating rate was never greater than 5°C/min. Once the maximum temperature was reached slight temperature adjustments were performed at the rate of 1°C/min. A K-type thermocouple, positioned on the edge of the cell, was used to monitor and record the cell temperature throughout the experiment.

The position of the reactor inside the furnace is important for temperature control. There is greater heat loss when the reactor is positioned at the end of the furnace and exposed

to air to allow optical access. Ceramic fibre insulation was used to cover the gaps between the tube bore and the quartz tube to preserve as much heat as possible. The temperature was adjusted according to the thermocouple readout to ensure the operating temperature was reached.

4.1.5 Materials

The choice of materials suitable for the test apparatus was limited by the high temperature of operation of SOCs and highly reducing and highly oxidising gas compositions. It was important to select materials that would not react with the gases and interfere with the spectroscopic measurements by poisoning the electrochemical cell (Cumming et al., 2015). Stainless steel and polyether ether ketone (PEEK) thermoplastic polymer were chosen as the main components for the base unit. PEEK has excellent mechanical and chemical resistance properties at elevated temperatures and is both thermally and electrically insulating. The components in the heated zone were fabricated from alumina, quartz, and precious metals (platinum or gold). Another factor that needed to be taken into account was the thermal expansion coefficient of the components located in the 'hot-zone'. The coefficient of thermal expansion of the alumina and quartz (fused silica) are $8.4 \times 10^{-6}/^{\circ}\text{C}$ and $0.55 \times 10^{-6}/^{\circ}\text{C}$, respectively, hence alumina needed extra space to allow for expansion without putting stress and eventually breaking the quartz outer tube .

4.1.6 Sealing of the SOC

Originally, Kerafol® KeraGlas ST K02 (Keramische Folien GmbH) glass sealing tape was used to form a seal between the SOC electrolyte and the alumina tube. The tape worked well in the vertical rig position and a good seal was achieved. Unfortunately, when the reactor was operated in a horizontal position, the cell would slide down the tube as the glass melted.

After numerous attempts to fix the issue, an alternative sealant was found. Vermiculite compression gaskets, Thermiculite® 866 and 886LS, (Flexitallic, UK) were tested and provided a good seal and easy removal. The 866LS was the preferred choice; the main difference between the two is addition of glass powder to 866LS. As the glass powder melts ($\sim 700^{\circ}\text{C}$), a conformable and viscous layer is formed between the gasket and the alumina surface, allowing for a seal to be created even when the compressive loading is not too high.

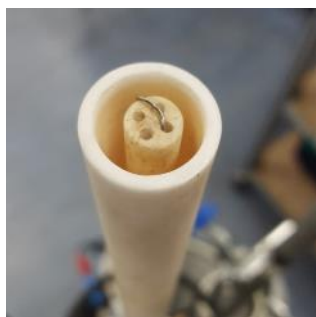
4.2 Full System Commissioning

The assembly of all the components described earlier is straightforward, however, each component needs to be connected in the correct order (see Figure 4-6). Ceramic tubes are used to seal the cell on as well as to direct gas from the base unit to the active electrode.

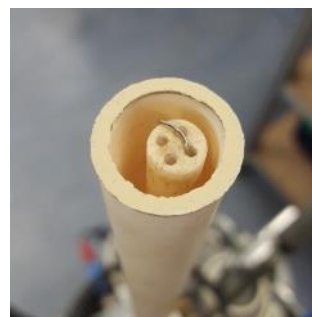
Since all of the experiments in this study focused on the fuel electrode, the air is delivered to the electrode along the 4-bore alumina tube and fuel mixture through the quartz tube just outside the cell.

Precious metal wires and mesh, in this case platinum, were used to measure electrochemical performance of the SOC. Unlike Pomfret's reactor, where the cell is mounted onto a support tube using alumina paste (Pomfret et al., 2006), this reactor relies on applied pressure to seal the sample and ensure good electrical connection between the current collector wires and the electrodes.

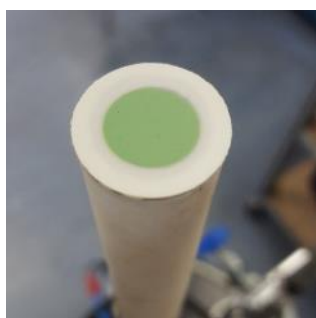
Extra care was be taken when loading the cell; on heating up all of the components expand, so to avoid breaking the cell, the bottom Pt wire was barely touching the cell on assembly. The setup was completed with a quartz outer tube and a metal collar securing everything in place.



Step 1 – Assemble 4-bore gas inlet tube with current collector wire inside alumina support tube.



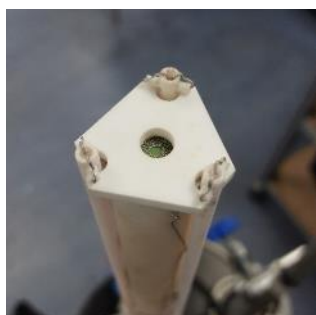
Step 2 – Position a mica seal on the support tube rim.



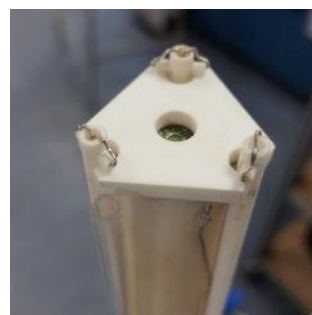
Step 3 – Place a cell onto a mica seal.



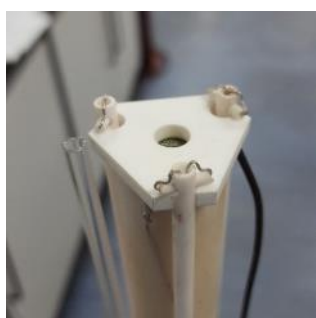
Step 4 – Place a current collector with a mesh on top of the cell.



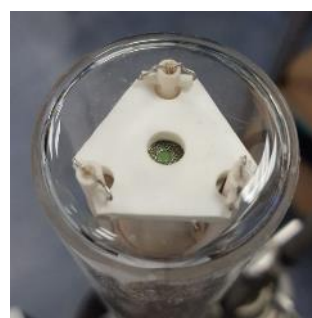
Step 5 – Place the spring-loaded triangular top plate and hook up the springs underneath the top pedestal.



Step 6 – Add quartz gas inlet tube.



Step 7 – Add thermocouple and secure connections in place.



Step 8 – Close the reactor with a quartz tube and screw on a collar to hold the tube and create a seal.

Figure 4-6. Step-by-step rig assembly procedure.

4.2.1 Gas leak testing

The gas-tightness of the rig was tested using high-pressure compressed air and gas leak detector spray. All fixings of the rig, where gas could escape, were checked and proved to be leak-free. The potentially vulnerable location for gas leak was the quartz outer tube; two rubber O-rings were placed onto the tube and lowered down to the base unit. The seal was formed by sliding the outer tube flange down the quartz outer tube and tightening it onto the threaded base unit part by rotating the flange.

Gas leak testing was also performed on gas lines coming from the cylinders to the MFCs and to the rig each time the setup was modified. Carbon monoxide detectors were placed next to the cylinder and the reactor to alert in case there was a leak and an oxygen monitoring device was installed in the laboratory.

4.2.2 Temperature Monitoring

The heat is inevitably lost from the furnace and the reactor during operation. To reduce these losses, high temperature glass wool insulation material was used on each side of the tube furnace as well as on the rig's outer tube. Closer to the base unit, where the temperature was considerably lower, aluminium foil was used to secure the wool and provide extra thermal insulation.

The temperatures of the cell and the microscope objective were continuously monitored throughout the experiment using thermocouples located close to the hottest part of the component. The objective temperature did rise above 50 °C but did not exceed 100 °C. It was allowed to cool down slowly to avoid thermal shock and cracking of the objective lens. The temperature profiles of the objective, furnace, and SOC are shown in Figure 4-7.

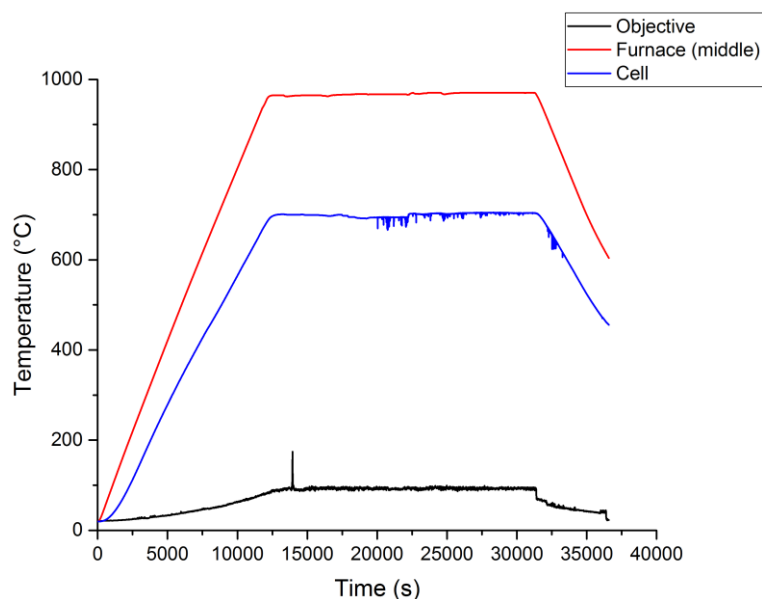


Figure 4-7. Typical temperature recordings of the objective, furnace and cell during *operando* measurements.

4.3 Raman microscope setup for *in operando* experiments

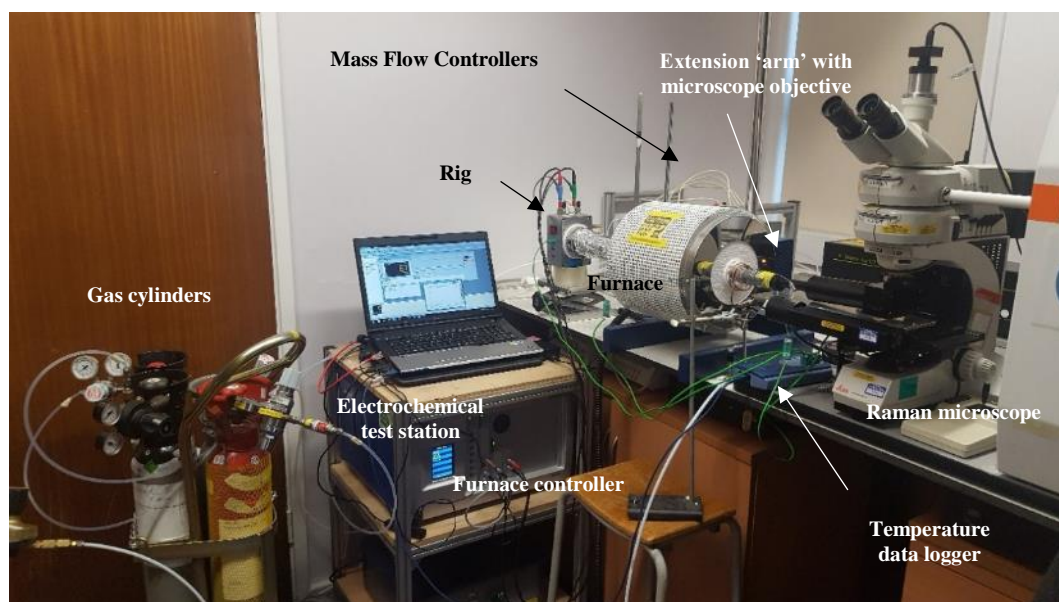


Figure 4-8. Experimental setup for spectroelectrochemical characterisation of SOCs.

A number of different components and equipment are required to work simultaneously for spectroelectrochemical *operando* SOC measurements. The whole setup of the test bench for SOCs (excluding steam generator and compressed air cylinder) is shown in Figure 4-8.

4.4 Cell test methodology

Where possible, the same initial cell performance characterisation should be performed. A typical experimental protocol is described below:

1. Once the cell is assembled, focus Raman microscope objective on the surface of the material under investigation.
2. Heat up the reactor at 5 °C/min in N₂ until the operating temperature is reached. Make sure to switch on the air cooling of the objective.
3. When the temperature is reached and stable, re-focus the objective as the cell will expand on heating and the Raman microscope will be out of focus.
4. Reduce the cell if necessary, monitoring Raman spectra, re-focus the objective. Monitor OCV and let the cell stabilise for 15-30 minutes.
5. Measure EIS and I-V curves.
6. Adjust gas composition, stabilise and measure the ‘initial’ EIS and I-V characteristics.
7. Apply current/voltage for a certain period of time. Collect Raman Spectra simultaneously, adjust the focus when needed.
8. Measure the ‘final’ EIS and I-V characteristics.
9. Cool down the setup in N₂.

The next steps relate to the data analysis:

1. Correct the data for inductance artefacts.
2. Correct the impedance and I-V data for cell geometry (for SOC – electrode area $A=\pi r^2$; pellet – *geometric factor* $(GF)=d/A$, where d =sample thickness (cm) and A =electrode area (cm²)).
3. Use K-K transforms to validate the data.
4. Plot the data in different formalisms and fit to an equivalent circuit.
5. Remove the background from the Raman spectra if necessary and de-convolute the Raman peaks.

4.5 Electrochemical data acquisition

Electrochemical impedance spectroscopy (EIS) is a powerful, non-destructive technique for characterisation bulk material, surfaces, and electrochemical systems. It is also a very

sensitive technique, therefore, experimental EIS results are often affected by parasitic inductance effects. These effects originate not only from the sample under study but also the test rig and cables connected to the electrochemical interface. Although the parasitic inductance affects are more pronounced at higher frequencies, they can have significant effect on the middle and low frequency range (Raikova et al., 2009). The inductance errors can have a strong influence on the accuracy of the EIS data and hence need to be taken into account.

4.5.1 Inductance correction

To correct for inductance effects, a closed circuit experiment between two Pt wires and Pt mesh was carried out at different temperatures, in the frequency range 1 MHz to 0.1 Hz. There was a significant amount of noise in the lower frequency region of the imaginary component (Figure 4-9), so the average values for resistance and inductance values were extracted across the linear regions (approximately 1 kHz – 10 Hz for resistance and 100 kHz – 10 kHz for inductance) from Z' and Z'' data, respectively. Inductors are purely reactive components, and they influence only the reactive, imaginary part of the impedance.

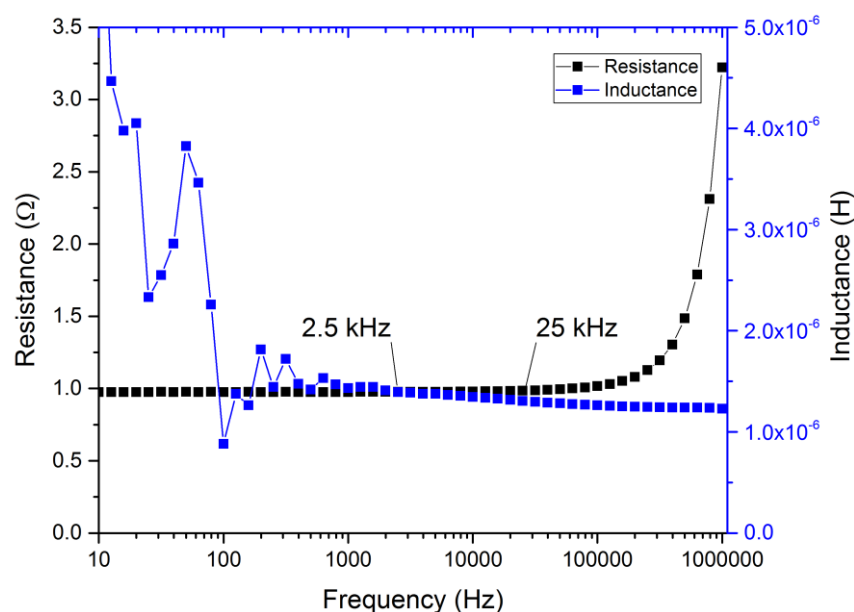


Figure 4-9. A plot of resistance and inductance versus frequency for 600 °C closed circuit experiment (on heating).

The experiment was carried across the operating temperature region (600 – 900 °C) on both heating and cooling cycles. To have a real representation of the scale of the errors,

the rig was re-assembled prior to testing. Figure 4-10 and Figure 4-11 show the average resistance and inductance versus temperature for the closed circuit experiments. The average error for the resistance values across the temperature range were 0.56% on heating and 0.41% on cooling. The inductance errors were consistently larger, likely due to noisier data, 1.94% on both heating and on cooling.

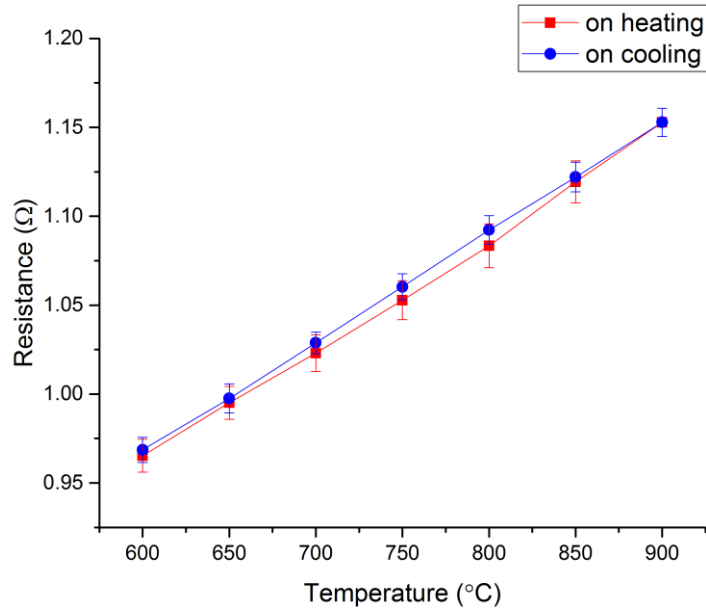


Figure 4-10. A plot of resistance versus temperature for closed circuit experiment.

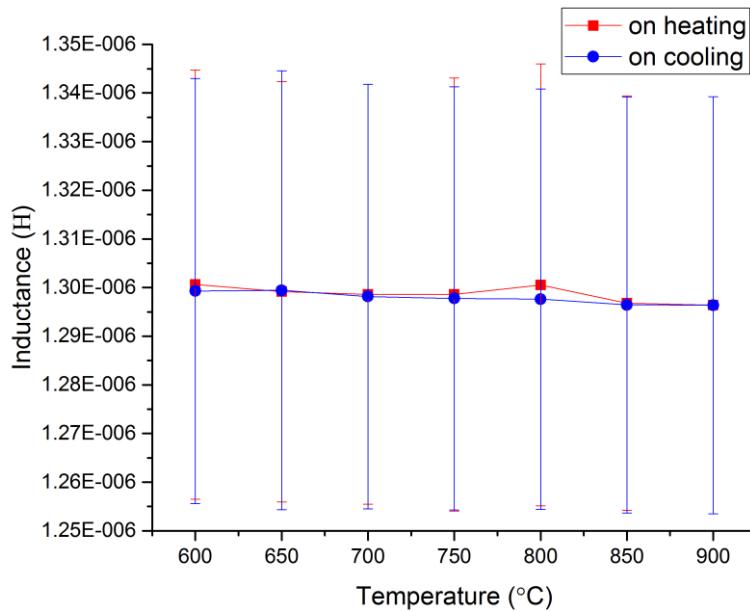


Figure 4-11. A plot of inductance versus temperature for closed circuit experiment.

For data comparison, the manually calculated inductance error was compared to the values extracted from the online software DRT Tools (Wan et al., 2015). The associated

inductance was $1.298\text{E-}06$ H and $1.07\text{E-}06$ H, respectively. Figure 4-12 illustrates the experimental data on a Bode plot and corresponding distribution of relaxations times. At a first glance, the Bode plot is not significantly affected by the correction, however, DRT comparison shows the decrease in magnitude of DRT peaks at lower frequencies. These effects are even more pronounced at higher temperatures as the test sample resistance decreases. Where the data are not corrected for inductance errors, the series resistance, R_s , is underestimated and the polarization resistance, R_p , is overestimated (Thompson et al., 2015).

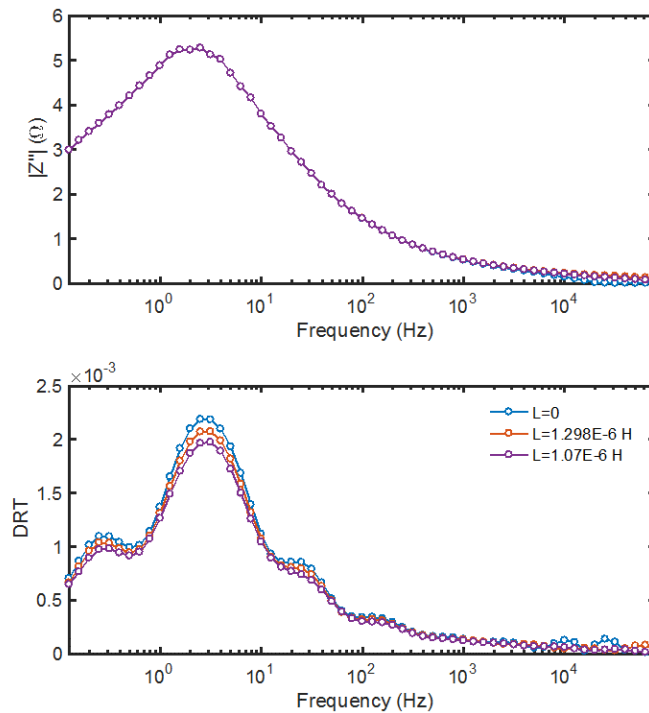


Figure 4-12. Bode plot of Z'' vs frequency for uncorrected and two inductance-corrected data (top) and the corresponding DRT (bottom)³.

³ The DRT analysis was done by A. R. Thompson using her own programme code written in MATLAB.

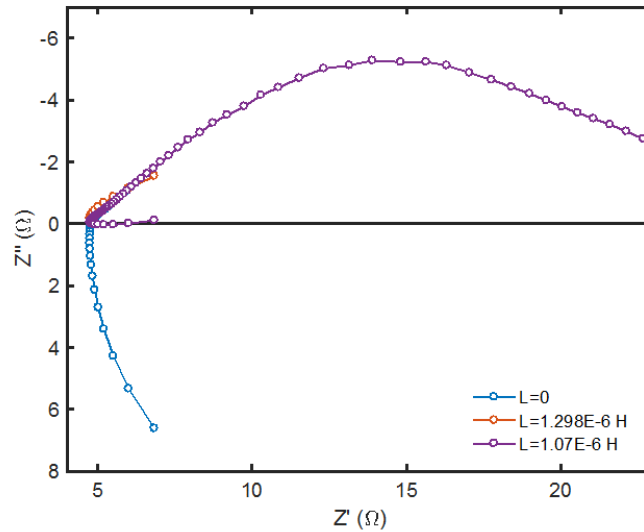


Figure 4-13. Nyquist plot of impedance data with two induction corrections (L) applied.

A Nyquist plot shows the uncorrected data ($L=0$) and two inductance-corrected spectra, see Figure 4-13. When the experimentally measured inductance value ($L=1.298\text{E-}06$ H) is subtracted from the raw data, the Z'' points of the inductive tail do not cross the axis, meaning that the data are overcorrected. The value obtained from DRT Tools software ($L=1.07\text{E-}06$ H), however, generated a much better fit hence they were used for the inductance correction.

4.5.2 Data quality measurement (Kramers-Kronig validation)

For an accurate interpretation of impedance data, the experimental data must be of high quality and error-free. In practice, however, small changes often occur during measurements, such as electrode poisoning, changes in the surface conditions or noise in the system. These changes in the experimental environment are easily detected by Kramers-Kronig (K-K) transforms described in Section 2.4.

Linear Kramers-Kronig Validity Test (LIN-KK Tool) (version 1.3 (16.12.2015)) written by the researchers at Karlsruhe Institute of Technology as a MATLAB® code was used to calculate the residual patterns (Boukamp, 1995, Schönleber et al., 2014, Schönleber, 2014).

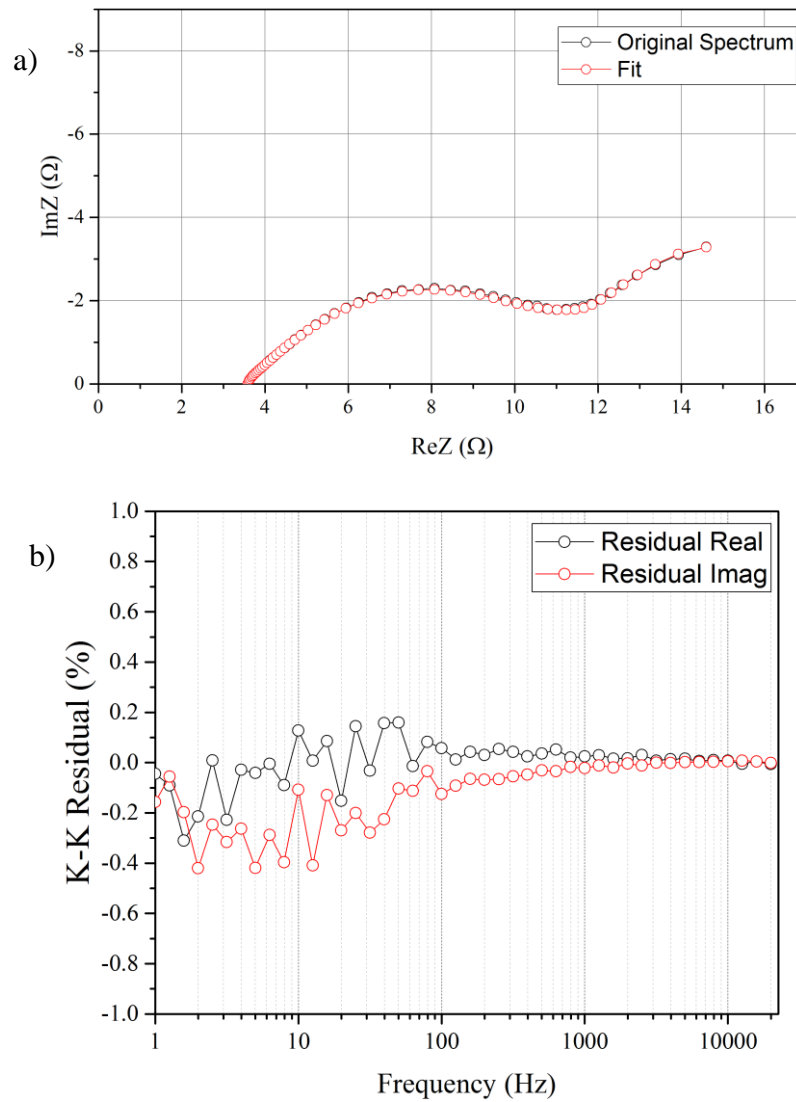


Figure 4-14. Examples of original spectrum, fitted (a) and residual (b) pattern of the Kramers-Kronig test performed on the impedance spectrum of the cell operated at 700 °C in H₂.

Figure 4-14 shows an example K-K validation of the impedance spectrum for the SOC at 700 °C. The impedance data were fitted without any inductive region data ($\text{Im} > 0$) to exclude unavoidable inductive effects from the calculations. The residual error patterns of the real and imaginary components of the EIS showed relative small errors that typically did not exceed $\pm 0.5\%$ with low levels of noise at lower frequencies, obeying the Kramers-Kronig transformation. This means that the data is of good quality and can be used for further analysis, such as DRT if necessary.

5 *Operando* Raman spectroscopy characterisation of carbon deposition on Ni-YSZ electrode during CO₂ electrolysis

This chapter outlines the *operando* Raman spectroscopy testing of the planar Ni-YSZ|YScSZ|LSM-YSZ/LSM solid oxide cells. The samples were characterised at 700 °C in 50/50 CO₂/CO oxidant/reductant ratio and under 100 mA cm⁻² negative bias (electrolysis conditions). Carbon formation kinetics on the surfaces of Ni-YSZ cermet is presented alongside the electrochemical measurements. The effect of carbon deposition on the Ni-YSZ electrode is analysed post mortem using a combination of scanning electron microscopy and Raman spectroscopy.

5.1 Cell preparation

The cells used for this study used YScSZ electrolyte purchased from Kerafol - Ceramic tapes GmbH. The electrolytes were tape casted as one sheet, sintered to 100 nm thick and laser cut to size. Ni-YSZ and LSM-YSZ electrodes and LSM current collector were

screen-printed in house to a green thickness of ca. 20 μm and sintered in air. The exact conditions are described in Section 3.1.3. A thin gold current collector mesh was deposited on the Ni-YSZ and cured at 800 °C for 2h prior to testing.

5.2 Benchmarking of the cells in H₂

Prior to testing the cell in the desired atmosphere, NiO needs to be reduced to metallic nickel to be able to conduct electrons. Cell 1 and 2 were benchmarked against each other in H₂ (50 H₂ / 50N₂) at 700 °C. Figure 5-1 shows the Nyquist and Bode plots of the EIS data for cells 1 and 2.

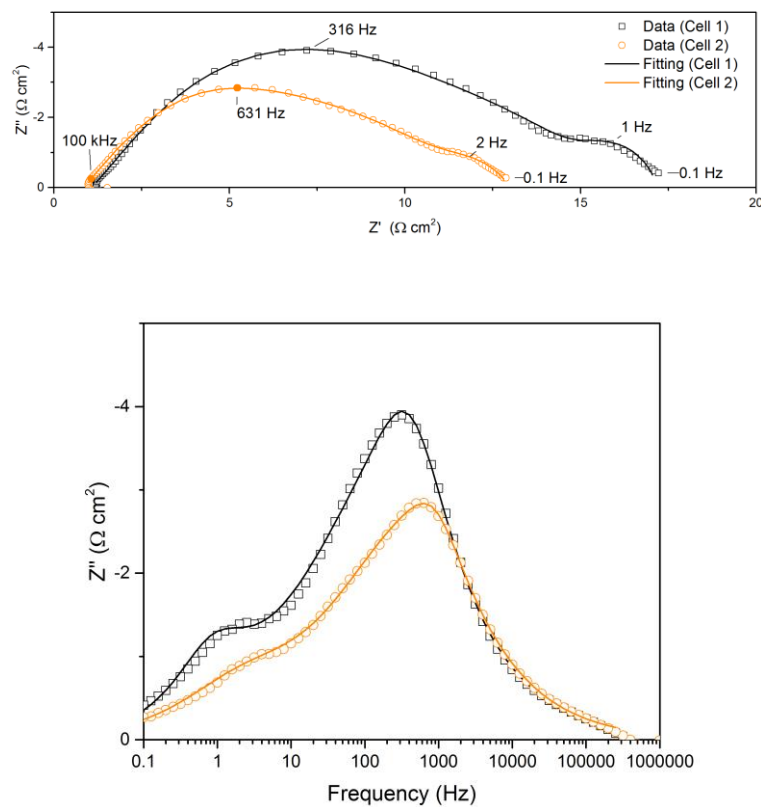


Figure 5-1. Nyquist (top) and Bode (bottom) plots of EIS data of cell 1 and 2 in H₂ at 700 °C.

Both cells had similar ohmic resistances (R_{ohm}), however, the polarisation resistance (R_p) of cell 1 was approximately 4 $\Omega \text{ cm}^2$ larger. This was also reflected on the i-V and power density measurements in Figure 5-2.

The EIS data was fitted with an equivalent circuit model, with a series resistor representing SOC's electrolyte (R_0) and three resistor circuits connected to constant

phase element component (CPE) in parallel (R1-CPE1, R2-CPE2 and R3-CPE3). The overall model used for fitting is shown in Figure 5-3.

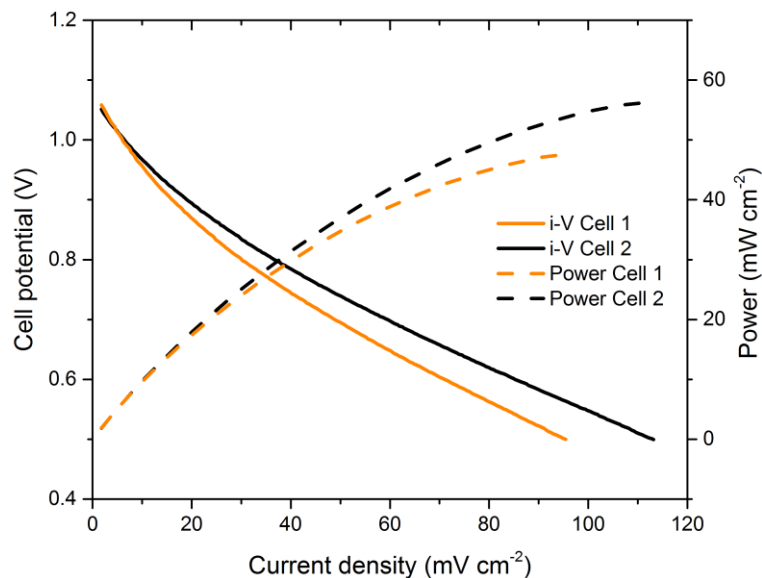


Figure 5-2. Current-voltage characteristics and power density of cells 1 and 2 in H₂ at 700 °C.

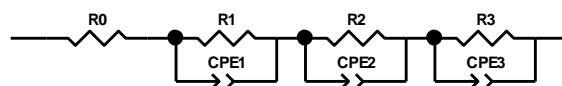


Figure 5-3. Equivalent circuit model used to fit EIS data in Figure 5-1.

The resistance and capacitance values (approximate⁴) for each of the components are summarised in Table 5-1.

⁴ A semi-circle arc was fitted mathematically to obtain the f_{max} values to calculate the capacitance from the associated resistances with $\pm 10\%$ error in values.

According to the capacitance values assignment in Table 2-2, R1-CPE1 and R2-CP2 correspond to the sample-electrode interface and potentially an electrochemical reaction for R3-CPE3.

Table 5-1. Resistance and capacitance values for cells 1 & 2 in H₂ at 700 °C.

	R0	R1	C1	R2	C2	R3	C3
	(Ω cm ²)	(Ω cm ²)	(F cm ⁻²)	(Ω cm ²)	(F cm ⁻²)	(Ω cm ²)	(F cm ⁻²)
Cell 1	0.967	0.768	2.02E-05	9.91	2.96E-05	3.55	7.79E-03
Cell 2	1.16	1.54	2.06E-05	13.26	4.08E-05	6.04	4.06E-03

5.3 Operando Raman spectroscopy monitoring of carbon deposition

Following the benchmark, the gas composition was changed to 50/50 ratio of CO₂/CO and allowed to stabilise. EIS data were measured before and after applying 100 mA cm⁻² negative bias to the cell and monitoring carbon formation kinetics on the surface of Ni-YSZ electrode. Raman spectra were collected at 20 s intervals in the region of 1150 – 1700 cm⁻¹ for 3 and 5 h for cell 1 and 2, respectively.

These measurements were collected using the reactor described in the previous chapter. The Raman spectra showed two peaks characteristic to the two main carbon peaks of D (1350 cm⁻¹) and G (1590 cm⁻¹).

The carbon deposition was observed shortly after the bias was applied and continued to increase in signal until approximately 1 hour of operation. The intensity stayed almost unchanged. The intensity of the Raman data relies on the sample analysed to be in focus at all times, however, at high temperatures there are small surface transformations happening all the time; e.g. structural due to localised cooling or heating of the cell. This was achieved by manually adjusting the focus on the microscope when required. Both cells showed similar amount of carbon growth on the fuel electrode surface as shown in Figure 5-4.

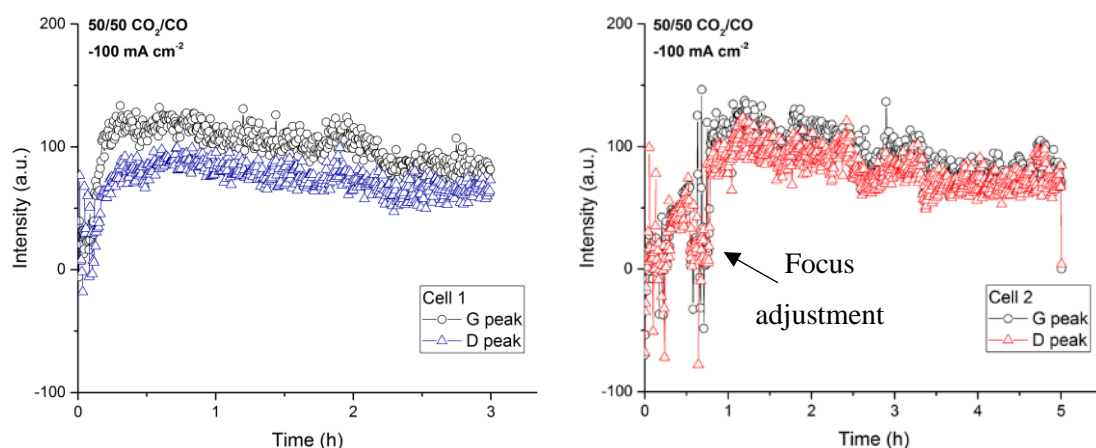


Figure 5-4. Carbon D and G peak intensities obtained from Raman spectra collected at 700 °C in 50/50 CO₂/CO and 100 mA cm⁻² negative bias for cell 1 (left) and 2 (right). The intensities were obtained by integrating both peaks.

Raman spectra of D and G peak region extracted at regular 35 min intervals are presented in Figure 5-5. It can be seen that the onset of carbon formation was sooner for the cell 1 compared to cell 2. However, this may not be the actual truth, mainly because Raman measurement is collected at one spot at each time, so carbon could have been forming elsewhere on the electrode.

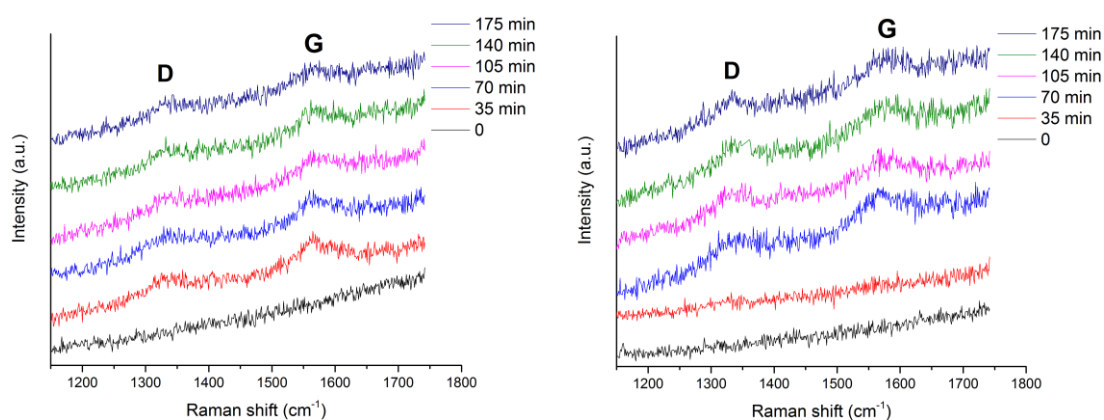


Figure 5-5. Operando Raman measurements taken at different time intervals, showing carbon growth kinetics at 700 °C in 50/50 CO₂/CO and 100 mA cm⁻² negative bias.

The EIS data for 50/50 CO₂/CO atmospheres are shown in Figure 5-6 before and after 100 mA cm⁻² of current was applied to the cells. Both showed decrease in the polarisation resistance.

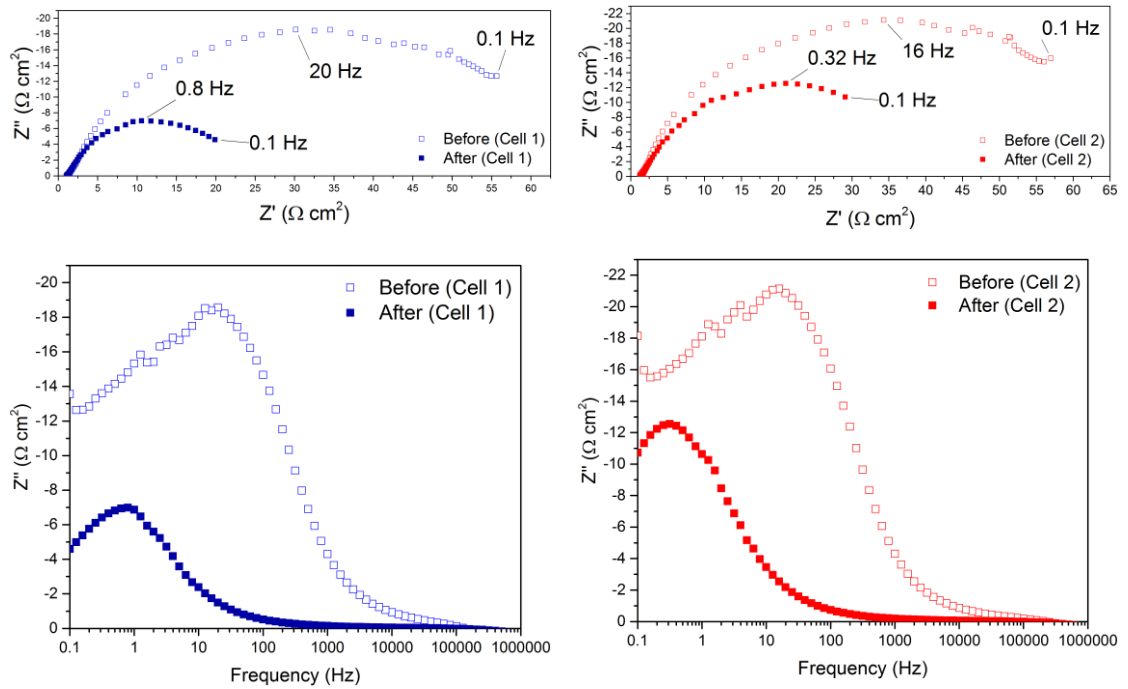


Figure 5-6. Nyquist (top) and Bode (bottom) plots of EIS data of cell 1 (blue) and 2 (red) in before and after CO₂ electrolysis at 700 °C.

Unlike the data collected in highly reducing atmosphere, the CO₂/CO can only be fitted with arc to obtain the overall resistance and capacitance values. These are shown in table below:

Table 5-2. Resistance and capacitance values before and after bias has been applied to the cell.

		R0	R2	C2
		($\Omega \text{ cm}^2$)	($\Omega \text{ cm}^2$)	(F cm^{-2})
Cell 1	Before	1.01	64.86	1.55E-04
	After	1.12	22.25	1.16E-02
Cell 2	Before	0.868	69.04	1.43E-04
	After	1.49	38.776	1.15E-02

The resistance of the cell 1 decreases from 64.86 to 22.24 $\Omega \text{ cm}^2$, while the capacitance increases significantly: from 1.55E-04 to 1.16E-02 F cm^{-2} . Similar increases in R and C values were observed for cell 2. Again, large capacitances suggest that the R2-CPE2 corresponds to the electrochemical processes of the SOC electrode.

Both cells 1 and 2 show a shift in frequency after the operation, suggesting that the reaction mechanism is different to the one before (Figure 5-6, Bode plots).

Researchers have previously reported the activation of the LSM electrode by applied potential, resulting the large reduction of the polarisation resistance (Haider and McIntosh, 2009). This activation process can be explained by the removal of SrO species from LSM surface and the reduction of Mg ions with oxygen vacancies (Jiang, 2007).

5.4 *Ex situ* analysis of SOCs

5.4.1 *Ex situ* Raman spectroscopy analysis of carbon deposits

Carbon deposits formed on the surface of Ni-YSZ electrode were analysed *post-mortem* using Raman spectroscopy method described in section 3.2.6. The most common forms of carbon observed were shapeless lumps or rods. Examples of these are presented in Figure 5-7, Figure 5-9 and Figure 5-11. The collected Raman spectra further revealed the differences in carbon deposits.

The Raman spectrum carbon of consists of first (1000 – 1800 cm⁻¹) and second-order (2500 – 3100 cm⁻¹) regions. This work, however, focused on the analysis of the first-order region only.

The majority of carbonaceous materials have two distinctive peaks appearing at around 1350 cm⁻¹ (D peak) and 1590 cm⁻¹ (G peak) in the first-order Raman spectrum. G peak is a stretching mode of E_{2g} symmetry at sp² site of graphite, whereas D is ascribed to structural disorder (Seong and Boehman, 2013). Disordered and amorphous carbons have three additional Raman bands at around 1200 cm⁻¹ (D4), 1500 cm⁻¹ (D3), and 1620 cm⁻¹ (D2) that relate to sp³-defects and impurities (Sadezky et al., 2005).

There have been many studies investigating the best peak decomposition methodology for treating Raman data (Ferrari and Robertson, 2000, Kouketsu et al., 2013, Seong and Boehman, 2013). However, there is still no clear consensus on peak-fitting procedure, particularly for lower grade carbonaceous material, such as amorphous carbon.

OriginPro software was used to fit 4 Lorentzian and 1 Gaussian (4L1G) curves to the five characteristic Raman bands similar to the method suggested by Seong and Boehman (2013). Other functions were trialled: pure Gaussian, Voigt, and pseudo-Voigt, mix of Lorentzian and pseudo-Voigt, however, 4L1G gave the best curve-fitted spectra. In all

cases G band was fixed at 1590 cm⁻¹ and Gaussian function was used to fit D3 band. Asterisks next to the band name mean that the position of that band was fixed. Additional X band (~1100 cm⁻¹) and A band (~1420 cm⁻¹) were also fitted to graphs in Figure 5-10 and Figure 5-12. No valid explanation has been found for the two bands to author's knowledge.

The ratio between the D1 and G peak intensities can provide valuable information about the degree of structural disorder in carbon. Upon carbonization, intensity ratios I_{D1}/I_G increase, whereas I_{D1}/I_G decrease during graphitization (Bernard et al., 2010). If the D1/G intensity ratio is higher than 1.0 (G band is lower than the D1) the carbon is less structured and contains containing sp³ lattice defects.

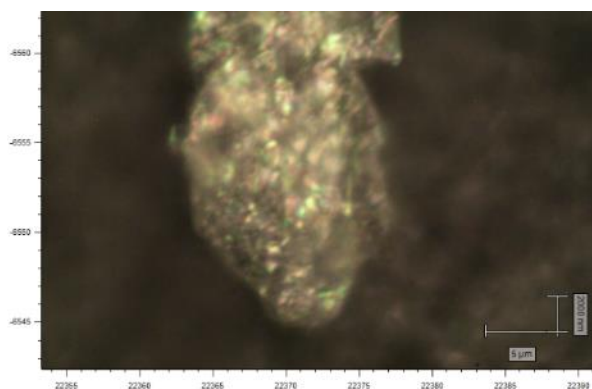


Figure 5-7. Raman microscope image of carbon deposit CD1.

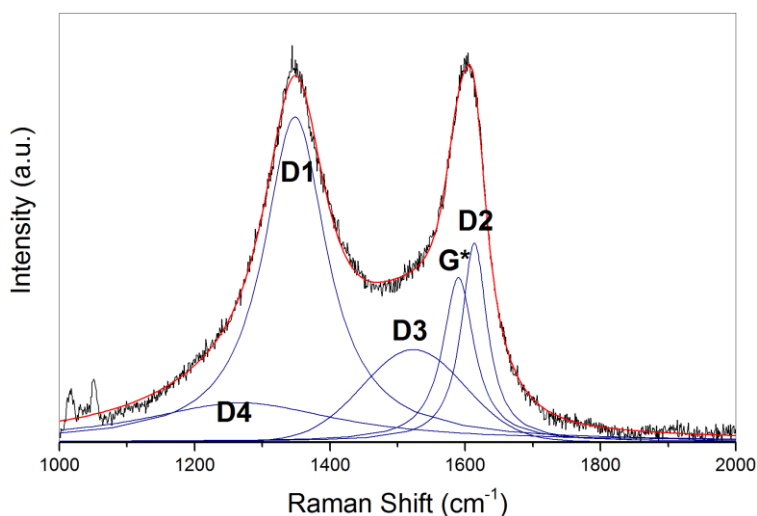


Figure 5-8. Deconvoluted Raman spectrum of CD1 carbon deposit.

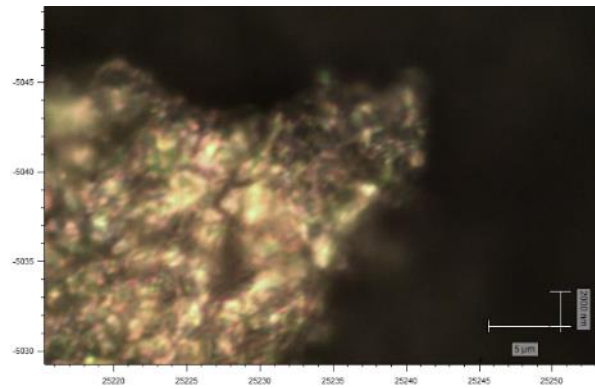


Figure 5-9. Raman microscope image of carbon deposit CD2.

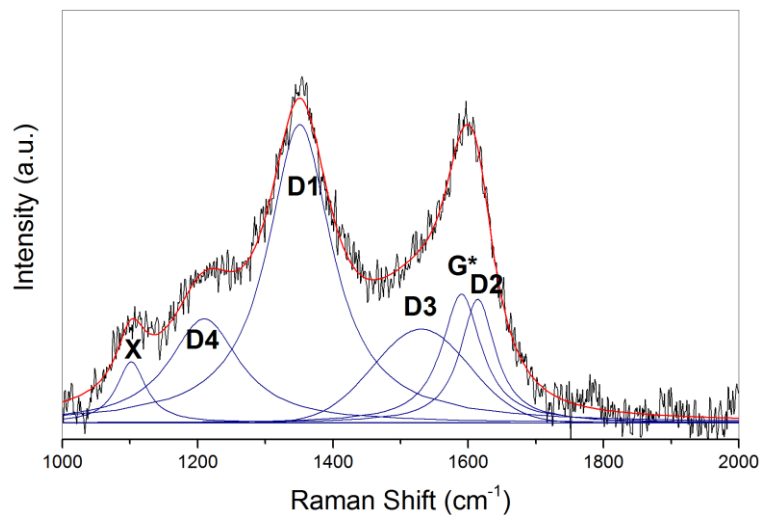


Figure 5-10. Deconvoluted Raman spectrum of CD2 carbon deposit.

An additional peak, X, around 1100 cm⁻¹ was detected during the deconvolution of CD2 Raman spectrum (Figure 5-10). An increase in FWHM of the D4 peak was also observed (Table 5-3); this peak is commonly associated with presence of C-C and C=C stretching vibrations (Ferrari and Robertson, 2000). From the data in Figure 5-10, it was unclear if peak X came from the carbonaceous material itself or from the Ni-YSZ or other surface impurity.

Similarly, Raman spectrum of CD3 (Figure 5-12) has a small band X present at 1091 cm⁻¹. In order to fit the X band that has a small peak area, D4 was fixed. In this spectrum a band was present in the region of approximately 1300 – 1550 cm⁻¹. A band in the same region was also observed by Gómez Sanz (2014) on the surface of zeolite catalyst after *n*-butane cracking.

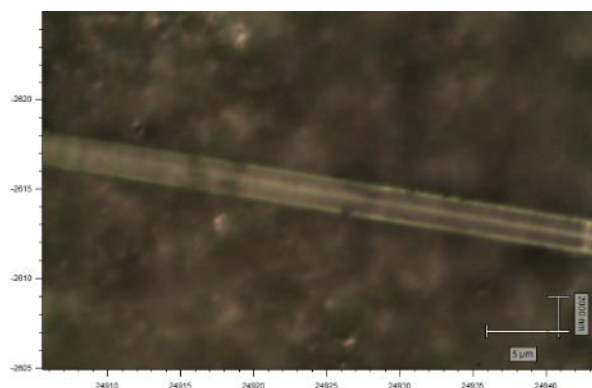


Figure 5-11. Raman microscope image of carbon rod deposit CD3.

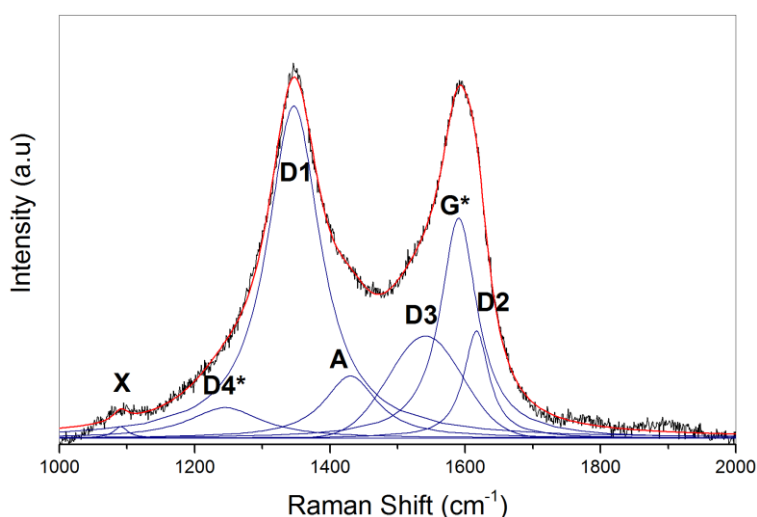


Figure 5-12. Deconvoluted Raman spectrum of CD3 carbon rod deposit.

The Raman curve-fitting parameters of carbonaceous materials CD1, CD2, and CD3 are summarised in Table 5-3. The height ratio of D1 to G (I_{D1}/I_G) and the area ratio of D1 to G (A_{D1}/A_G) were also calculated. I_{D1}/I_G ratios of 1.98 ± 0.3 , 2.32 ± 0.2 , and 1.51 ± 0.3 were obtained for samples CD1, CD2, and CD3, respectively. All of these values are higher than 1, suggesting formation of sp^3 -type defects in the sp^2 graphitic network. Presence of vacancies, grain boundaries and impurities are often what causes the disorder (Sadezky et al., 2005).

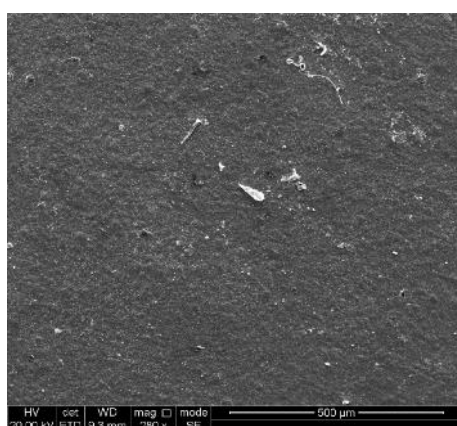
Table 5-3. Positions of the Raman bands, FWHM, I_{D1}/I_G, and A_{D1}/A_G ratios for carbon deposits CD1, CD2, and CD3 fitted with Gaussian (G) and Lorentzian (L) functions.

		CD1	CD2	CD3
X (L)	Position (cm ⁻¹)	-	1102	1091
	FWHM	-	53	26
D4 (L)	Position (cm ⁻¹)	1268	1210	1245
	FWHM	348	127	131
D1 (L)	Position (cm ⁻¹)	1348	1351	1347
	FWHM	113	115	95
A (L)	Position (cm ⁻¹)	-	-	1430
	FWHM	-	-	95
D3 (G)	Position (cm ⁻¹)	1497	1531	1541
	FWHM	178	168	129
G (L)	Position (cm ⁻¹)	1590	1590	1590
	FWHM	56	71	66
D2 (L)	Position (cm ⁻¹)	1613	1614	1616
	FWHM	46	63	45
Ratios				
	I_{D1}/I_G	1.98±0.3	2.32±0.2	1.51±0.3
	A_{D1}/A_G	3.84±0.4	3.62±0.5	2.17±0.4

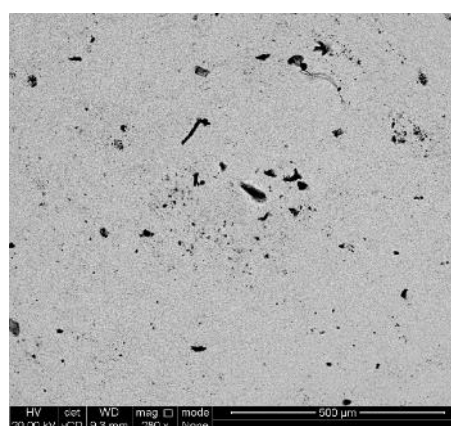
5.4.2 Post-mortem SEM characterisation of Ni-YSZ electrodes

5.4.2.1 Surface carbon

Scanning electron image (SE)



Back-scattered electron image (BSE)



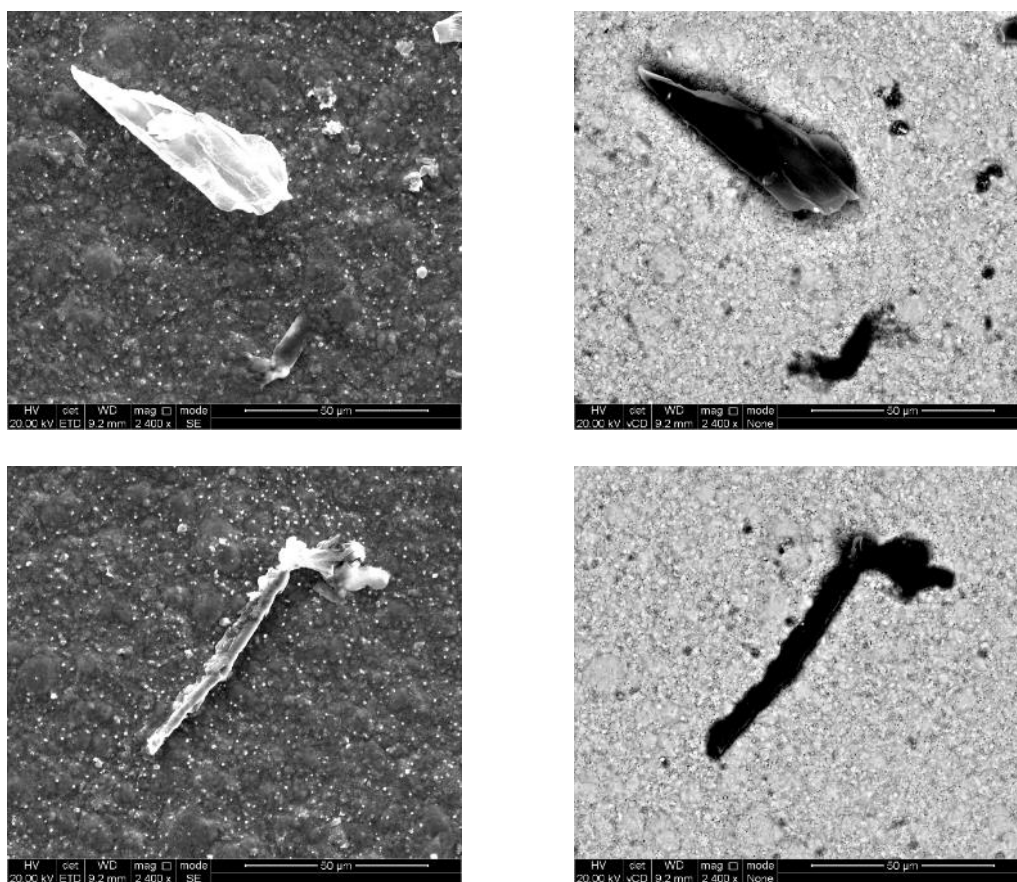


Figure 5-13. Scanning electron (SE) and backscattered electron (BSE) images of different carbon deposits at X2.4k magnification.

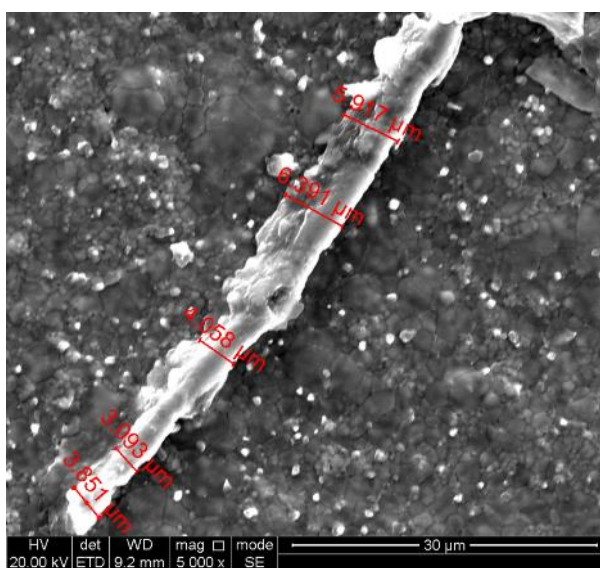


Figure 5-14. SEM image of carbon rod formed on Ni-YSZ surface (including approximate diameter measurements).

SEM results showed larger carbon deposits and rod-like structures distributed across the Ni-YSZ electrode. The contrast in the backscattered spectrum confirms that these are lighter in weight compared to the Ni-YSZ.

The diameter of the carbon rod formed on the surface was ca. 4.5 μm. The magnified images of the Ni-YSZ matrix are shown in Figure 5-15.

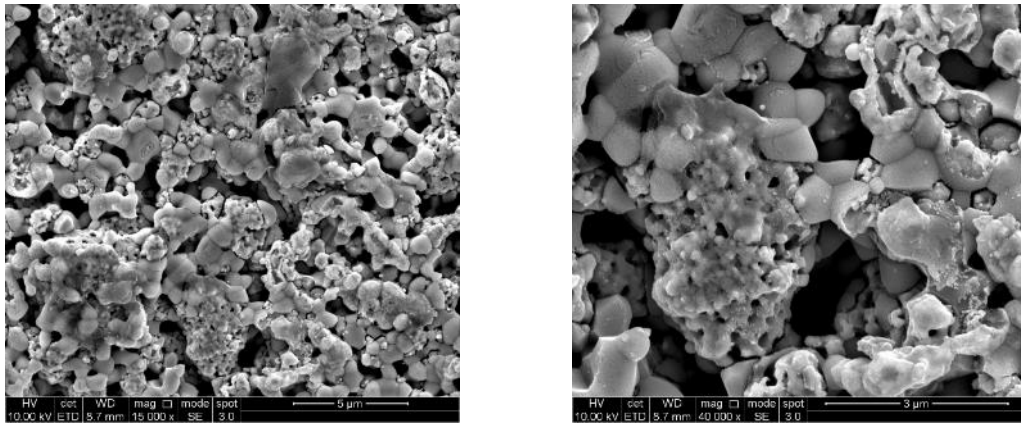


Figure 5-15. SEM images of Ni-YSZ surface after 3h CO₂ electrolysis under 100 mA cm⁻² bias at X15k (left) and X40k(right) magnification (cell 1).

Upon further investigation more carbon nanofibers were found close to the electrode/electrolyte interface. The fibres encapsulate Ni grains and can have a detrimental effect on the cell microstructure that could later lead to cell failure by electrode delamination (Tao et al., 2014).

The SEM images below show the extent of C formation during CO₂ electrolysis at 700°C. As expected, cell 2 (Figure 5-17) that has been run for 2 hours longer than cell 1 (Figure 5-16), showed more carbon formation in the electrode/electrolyte region. These observations are in line with the finding by Duboviks et al. (2015).

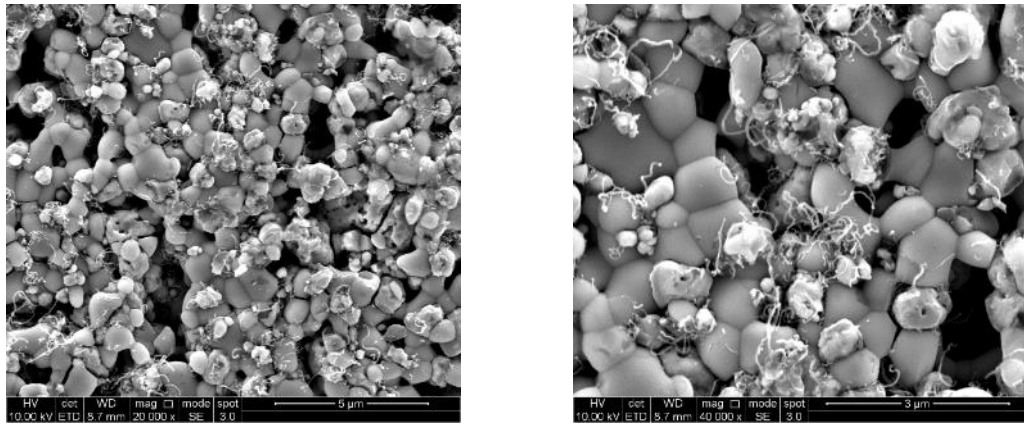


Figure 5-16. SEM images of Ni-YSZ at the electrode/electrolyte interface after 3h CO₂ electrolysis operation under 100 mA cm⁻² bias at X20k (left) and X40k(right) magnification (cell 1).

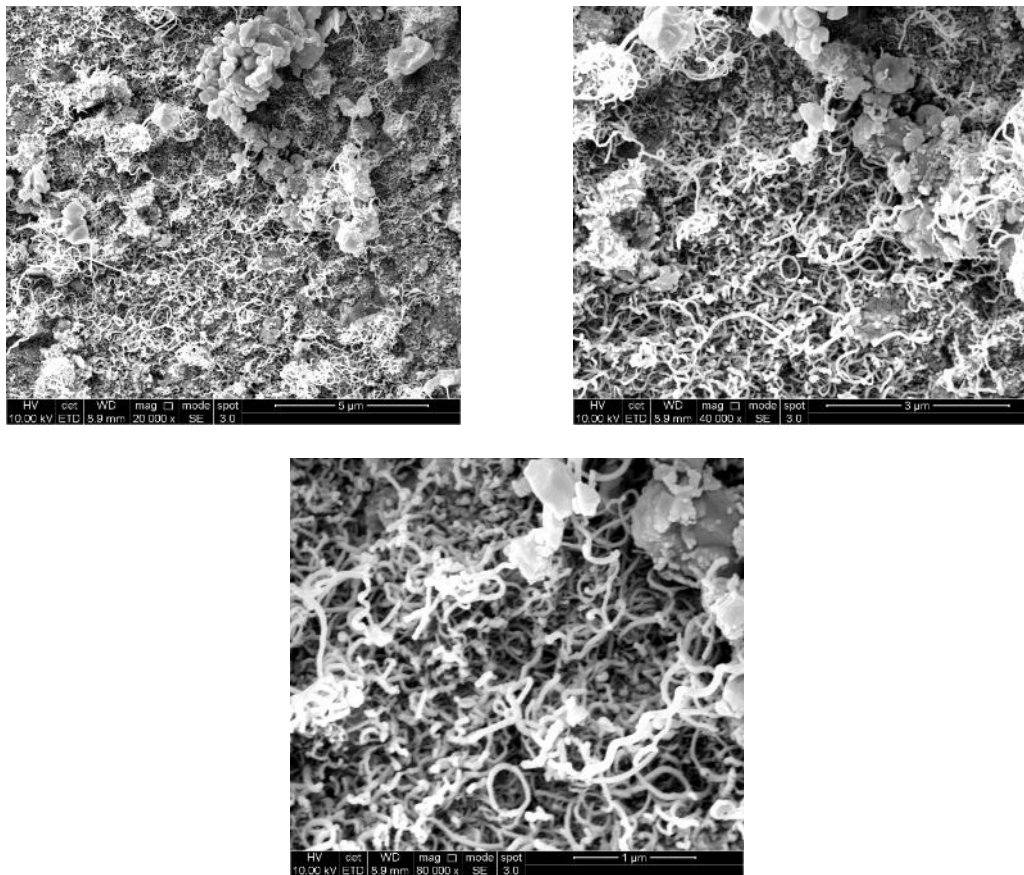


Figure 5-17. SEM images of Ni-YSZ at the electrode/electrolyte interface after 5h CO₂ electrolysis operation under 100 mA cm⁻² bias at X20k (top left), X40k(top right) and X80k magnification (cell 2).

5.5 Summary

Carbon deposition on the Ni-YSZ electrodes during CO₂ electrolysis has been investigated using a newly developed *operando* reactor to collect simultaneous Raman spectroscopy and electrochemical measurements. The carbon formations of disordered structure were observed on the surface of the electrode, however, the majority of it was found at the electrode/electrolyte interface (Duboviks et al., 2015). The formation of carbon deposits is believed to be due to the shift in the Boudouard reaction equilibrium ($2\text{CO} \rightarrow \text{C} + \text{CO}_2$) to the carbon deposition region, caused by the endothermic CO₂ electrolysis reaction.

6 Investigation into oxygen deficient CoFe_2O_4 -based ceramic electrode materials

A vast amount of effort is being devoted to the development of novel, high performance ceramic materials for SOC electrode applications to improve the economics of electrolysis. Mixed ionic-electronic conductors (MIEC) are widely used in energy conversion and storage devices, such as fuel cells and batteries. These materials conduct both ion and electronic charge carriers, namely electrons and/or holes, and can be single or multi-phase. The ionic and electronic conductivities of MIEC materials can be enhanced by controlling material composition, oxygen nonstoichiometry and defects (Lu, 2014).

The above properties make MIECs highly desirable materials for solid oxide electrolyzers. Dual-phase MIECs based on spinel of iron ferrite (Co, Ni or Mn) and gadolinium-doped ceria offer reasonable oxygen permeation, as well as electronic conductivity, and high tolerance to CO_2 , make them a good candidate for SOC fuel electrodes (Lin et al., 2015).

This chapter presents a material synthesis and characterisation study of CoFe_2O_4 (CFO) spinels, to assess its suitability for use as part of a dual-phase mixed ionic-electronic conductors for solid oxide electrolysis cell cathodes. Oxygen-deficient CFO and $\text{Ce}_{0.80}\text{Sm}_{0.2}\text{O}_{2-\delta}$ (SDC) were used as electron-conducting and oxygen-ion conducting phases, respectively. CFO material was prepared by solid-state reaction and sintered into

pellets at different temperatures and atmospheres. Following this the structural and thermal compatibility of the synthesised CFO and SDC nanoparticles were evaluated to select the most suitable condition for producing a symmetric cell that was tested for potential application as a SOC electrode for CO_2/CO reduction/oxidation.

6.1 Structural and morphological characterisation of CoFe_2O_4 powder

The initial characterisation of the starting reagents was performed using XRD ($\text{Cu K}\alpha$ $\lambda = 1.5405 \text{ \AA}$) radiation to confirm the structure of the materials and absence of phases. The XRD patterns of Fe_2O_3 and Co_3O_4 were in good agreement with the Powder Diffraction Files (PDF) cards no. 01-077-9926 and 01-078-1969 from the International Centre for Diffraction Data (ICDD) of a rhombohedral $\alpha\text{-Fe}_2\text{O}_3$ and cubic Co_3O_4 , respectively. The XRD patterns labelled with Miller indices (h k l) are shown in Figure 6-1.

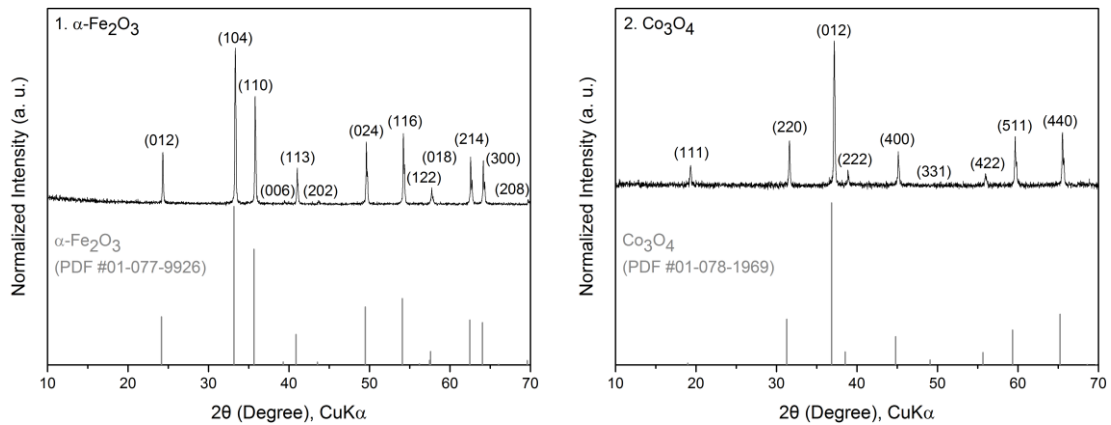


Figure 6-1. XRD patterns of (1) $\alpha\text{-Fe}_2\text{O}_3$ and (2) Co_3O_4 starting materials.

CoFe_2O_4 (CFO) powder was synthesised using the solid-state method, combining stoichiometric amounts of $\alpha\text{-Fe}_2\text{O}_4$ and Co_3O_4 precursors. The detailed synthesis method used for preparation of the CFO powder was described earlier in Section 3.1.1. To ensure the correct stoichiometry and material properties (e.g. electrical) of the product, the raw materials were dried prior to weighing to eliminate the contribution of adsorbed water vapour, CO_2 and other volatile organic residues to the solid state reaction (Boston et al., 2017). According to the phase diagram in Figure 6-2, the cubic spinel structure of CFO can be obtained at temperatures as low as $740 \text{ }^\circ\text{C}$ but not necessarily achieving a 100% reaction yield.

Galizia (2017) studied the effect of particle size of the starting materials on the reaction yield for the production of CFO; the results showed that nano-sized oxide precursors required a shorter calcination time as well as a lower temperature to form a single phase material. Despite this, the effect of temperature, described by the Arrhenius equation (6.1), remains the most important parameter influencing the reaction kinetics.

$$k = Ae^{-\frac{E_a}{RT}} \quad (6.1)$$

Here, k is the rate constant, A the pre-exponential constant for each chemical reaction, E_a is the reaction activation energy, R is the universal gas constant ($8.314 \text{ J K}^{-1} \text{ mol}^{-1}$) and T is the absolute temperature.

Calcination temperatures of 800, 900 and 1000 °C were investigated. The XRD pattern of powder calcined at 800°C showed more than one phase present (unreacted precursors) and both 900 and 1000°C temperatures resulted in single phase CFO. The calcination temperature of 900 °C was chosen as the optimum temperature for preparation of the CFO powder to keep the particle size as small as possible.

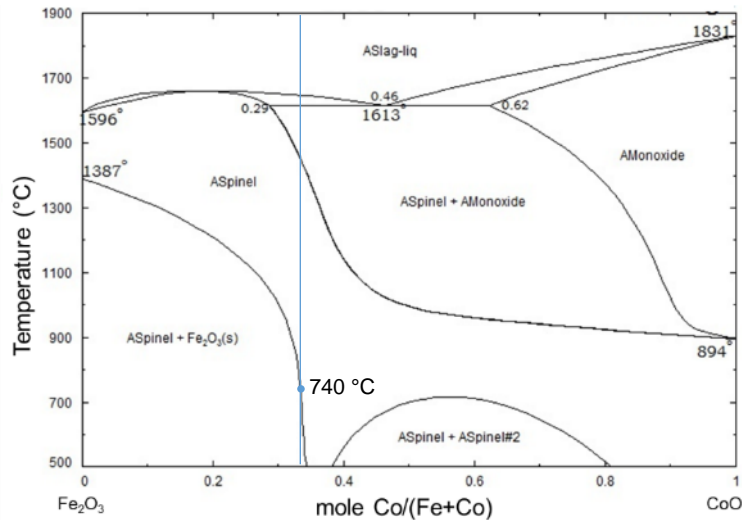


Figure 6-2. Fe-Co-O₂ oxide phase diagram at atmospheric pO_2 . Adapted from FactSage™ (2010).

The XRD pattern of the synthesised CFO material presented in Figure 6-3 closely matched ICDD PDF card no. 00-066-0244 (Kumar et al., 2014). The crystallite size of the CFO powder was determined from the XRD line-broadening of the most intense diffraction peak (311) using the Scherrer formula:

$$D = \frac{0.9 \lambda}{\beta \cos \theta} \quad (6.2)$$

where λ is the radiation wavelength, β is the full width at half maximum (FWHM) and θ is the Bragg diffraction angle. The calculated crystallite size was 33.4 ± 0.99 nm.

The lattice microstrain estimation was obtained from Williamson-Hall's plot using full width at half maximum (FWHM) of the XRD peaks and their corresponding diffraction angles using the following equation:

$$\varepsilon_{str} = \frac{\beta}{4 \tan \theta} \quad (6.3)$$

where ε_{str} is the lattice strain. The results suggested an average lattice strain of $1.77\text{E}-04 \pm 8.53\text{E}-05$ for freshly prepared powders.

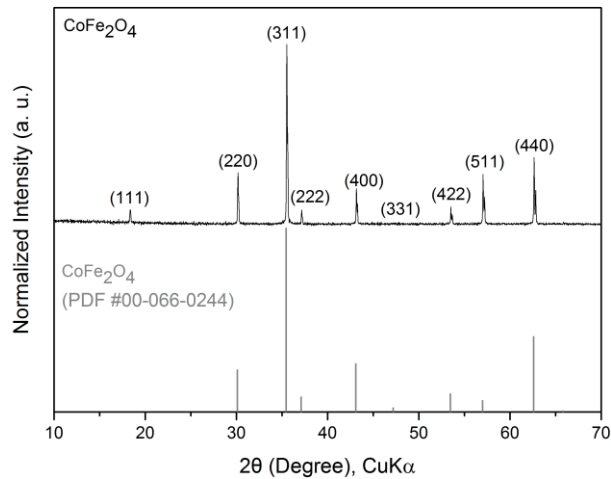


Figure 6-3. XRD pattern of synthesised CoFe_2O_4 material.

The density of the calcined CFO powder was measured using a AccuPyc II 1340 Series Pycnometer and was found to be 5.20 ± 0.01 g cm^{-3} , which is 98.3% of the theoretical density, taken as 5.29 g cm^{-3} (Thang et al., 2005).

The particle size analysis was performed using a Mastersizer 3000 (Malvern Instruments Ltd), based on the dynamic light scattering effect. A volume mean of 12.13 ± 1.25 μm (from D [4,3]) was obtained for the CFO powder prepared by solid state reaction. D [4,3] is sensitive to the presence of larger particles/agglomerates in the distribution, hence is often reported alongside D_x (10), D_x (50), the median, and D_x (90) values. In this case, 10%, 50% and 90% of the population lies below 3.70 ± 0.11 , 8.34 ± 0.38 and 26.40 ± 4.20 μm , respectively. The obtained result is presented in Figure 6-4.

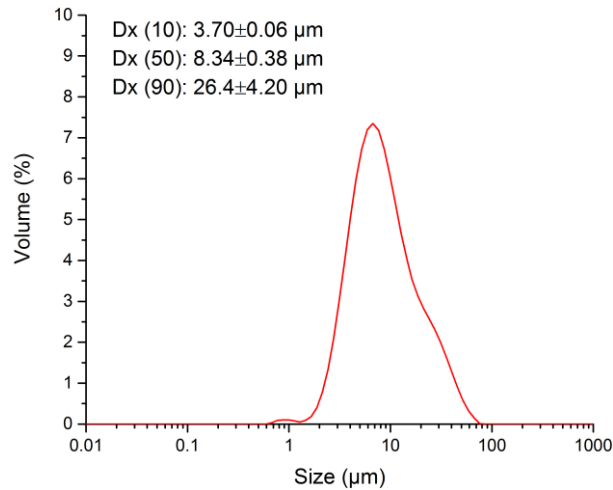


Figure 6-4. Particle size distribution of CFO powders calcined at 900 °C for 2 h.

Further investigation of the powder morphology revealed the presence of CFO aggregates and agglomerates with highly porous surface morphology, and primary particles of less than 1 μm (Figure 6-5). The magnetic nature of CFO and the van der Waals surface interactions often cause aggregation and agglomeration of the particles (Kurian et al., 2015). Therefore, the particle size analyser results mainly consist of the size distribution of the particle aggregates rather than the primary particles.

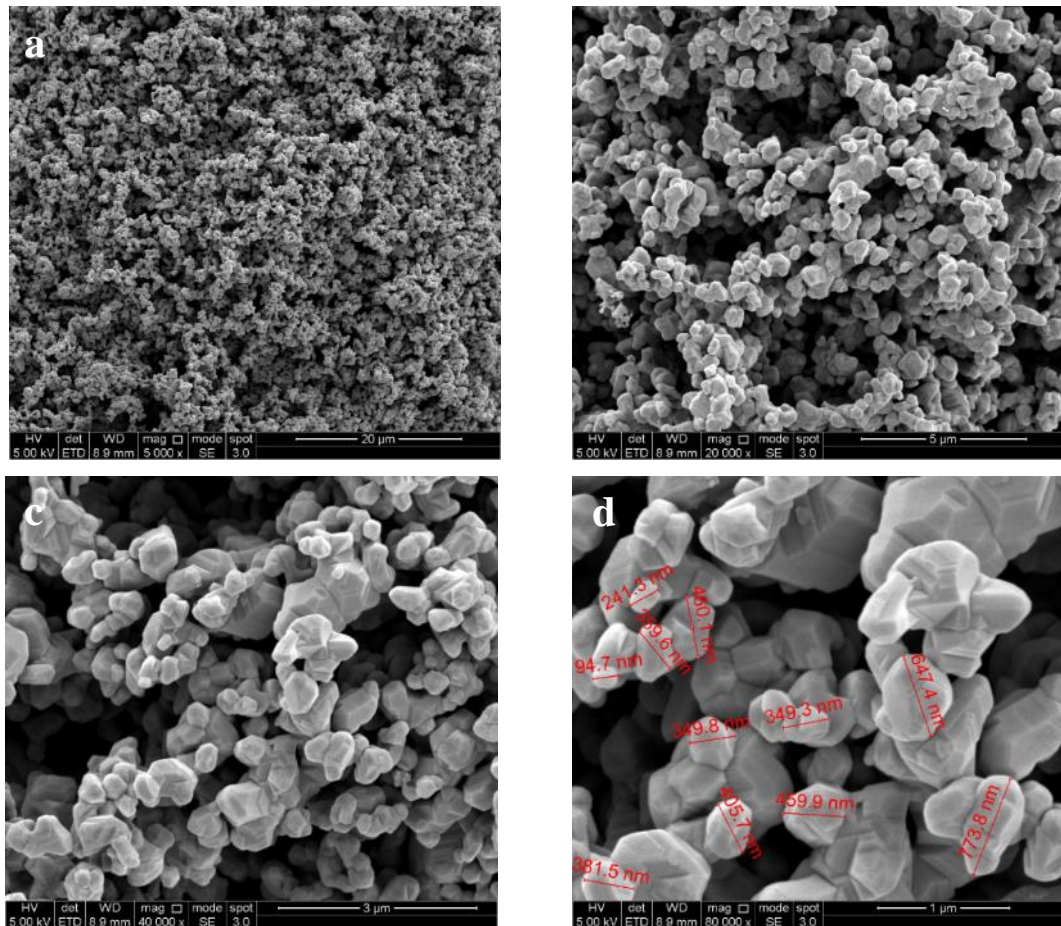


Figure 6-5. SEM images of CFO powder calcined at 900 °C for 2h at (a) 5,000, (b) 20,000, (c) 40,000 and (d) 80,000 magnification.

6.1.1 Thermal analysis

To understand the thermal decomposition behaviour of the CFO powder during sintering, thermogravimetric analyses (TGA) were performed under different atmospheres: air and nitrogen, at 10°C/min from ambient temperature to 1400°C. Cooling of the sample was also monitored. The results obtained are presented in Figure 6-6.

The thermograms of CFO powders revealed a total weight loss of 0.24 and 1.01% under air and N_2 flow, respectively. Both samples have lost a negligible amount adsorbed moisture; however, under nitrogen flow, the CFO material lost weight at a faster rate on heating compared to the sample under air flux. The onset of the rapid weight loss started at 1120°C. Loss continued up to the maximum temperature of 1400°C and continued to losing weight on the cooling cycle until approximately 1300°C. Between 1300 – 200°C the sample regained a small percentage of mass.

On the contrary, the CFO powder analysed under air flow only lost weight on heating until 1040°C when it started to gain weight continuously until the cooling cycle reached approximately 980°C , when it began to lose weight again.

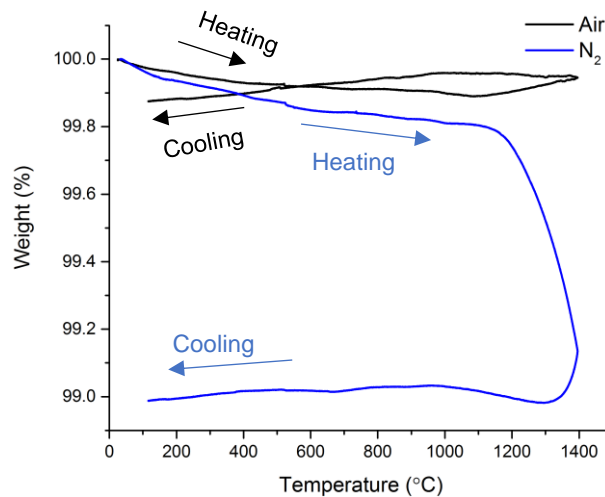


Figure 6-6. TGA curves for CFO powder under air and nitrogen atmospheres.

Many oxides lose oxygen at higher temperatures, creating oxygen vacancies, some of which may reabsorb depending on the cooling rate and oxygen availability (Gutiérrez-López et al., 2016). The TGA results suggest that CFO will lose oxygen under both atmospheres to create oxygen-deficient $\text{CoFe}_2\text{O}_{4-\delta}$; however, sintering samples in nitrogen would result in more prominent oxygen loss at lower temperatures, compared to the traditional method of sintering in air, achieving higher electrical conductivity.

6.2 CFO pellet sintering and characterisation

To investigate the properties of CoFe_2O_4 , the calcined powder was pressed into pellets that were sintered at three different temperatures, either in static air or under a flow of N_2 . The pellets were sintered at 1200, 1300, and 1400°C for 2 hours without the use of a binder. The density of the pellets was measured using Archimedes' principle (Section 3.2.1) and increased with increasing temperature (Figure 6-7), achieving a maximum (theoretical) density of 97.8 and 99.4% in air and N_2 , respectively. The theoretical density of the CoFe_2O_4 was taken as 5.23 g cm^{-3} (Fiorillo and Mayergoyz, 2004, Neelakanta, 1995).

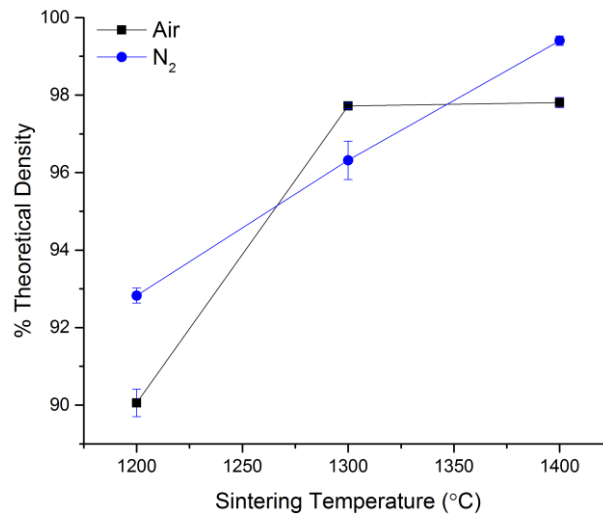


Figure 6-7. The effect of sintering temperature on the theoretical density of the CFO pellets.

6.2.1 X-ray Powder Diffraction

6.2.1.1 Phase analysis

The powder XRD patterns of crushed CFO pellets, measured at room temperature using molybdenum radiation (0.7093 \AA), are shown in Figure 6-8 and Figure 6-9. The main diffraction peaks of the CoFe_2O_4 crystal structure were present in all samples. The observed Bragg's reflections from (220), (311), (222), (400), (422), (511) and (440) planes confirm a well-crystallized cubic spinel structure with the $Fd\bar{3}m$ space group symmetry. No impurity phases were detected in any of the samples sintered in air, or in the sample sintered at 1200°C in N_2 . Additional diffraction peaks were detected for the 1300 and 1400°C pellets sintered in N_2 (Figure 6-9). The ICDD PDF-4+ database was used to identify the secondary phase. The patterns that matched closely were all metal monoxides: CoO (PDF #01-071-1178) (Sasaki et al., 1979), $\text{Fe}_{0.1}\text{Co}_{0.9}\text{O}$ (PDF #04-019-5918) (Proskurina et al., 2004) and $\text{Fe}_{0.5}\text{Co}_{0.5}\text{O}$ (PDF #04-02-6420) (Schmidt, 2008). Figure 6-10 shows the comparison of these spectra against CFO 1400°C N_2 sample.

All three patterns are based on the Wüstite structure crystal structure, $Fm\bar{3}m$ space group, and the lattice parameters very close to each other: $a = 4.263 \text{ \AA}$ for CoO , $a = 4.250 \text{ \AA}$ for $\text{Fe}_{0.1}\text{Co}_{0.9}\text{O}$ and $a = 4.278 \text{ \AA}$ for $\text{Fe}_{0.5}\text{Co}_{0.5}\text{O}$. According to the $\text{Fe}_3\text{O}_4\text{-Co}_3\text{O}_4$ phase diagram, the coexistence of a spinel and monoxide phases above 950°C is permitted (Le Trong et al., 2015), so it is possible that the phase is a mixed Co-Fe monoxide ($\text{Co}_y\text{Fe}_{1-y}\text{O}$).

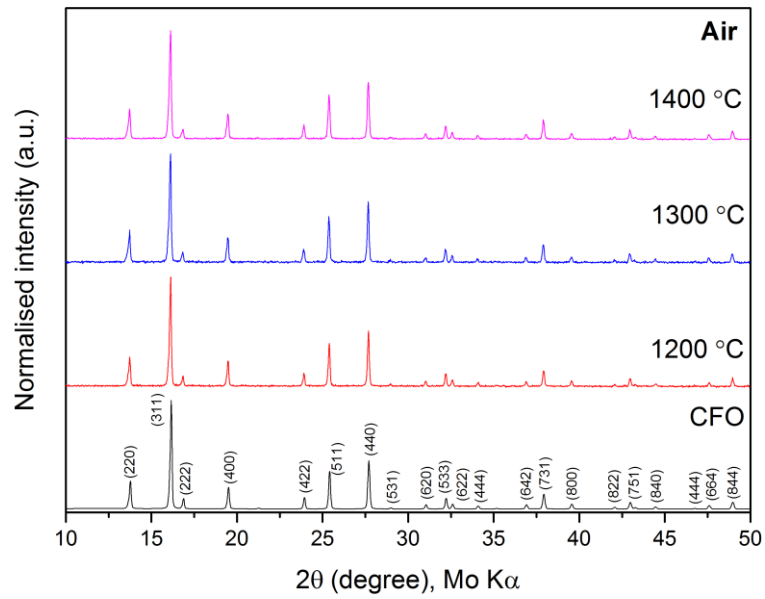


Figure 6-8. XRD patterns of CFO calcined powder and crushed pellets sintered at 1200, 1300 and 1400 °C in air.

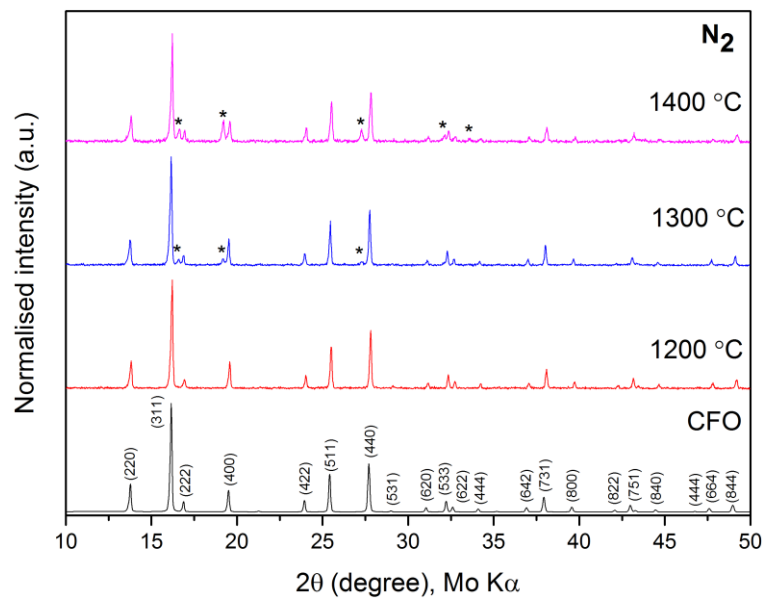


Figure 6-9. XRD patterns of CFO calcined powder and crushed pellets sintered at 1200, 1300 and 1400 °C under a flow of N₂. Extra peaks marked by the asterisks indicate secondary phase.

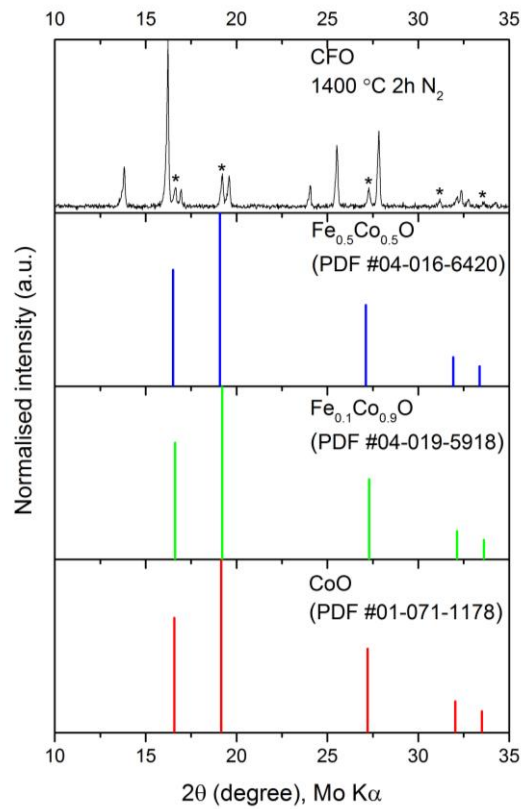


Figure 6-10. Comparison of XRD patterns of CFO 1400°C N_2 against CoO, $\text{Fe}_{0.1}\text{Co}_{0.9}\text{O}$ and $\text{Fe}_{0.5}\text{Co}_{0.5}\text{O}$ patterns from ICDD PDF-4+ database.

The crystallite size of the CFO powders from crushed pellets was estimated from the FWHM of the strongest diffraction peak using Scherrer's formula in equation (6.2).

Table 6-1 shows the crystallite size and microstrain for the sintered pellets. The microstrain was obtained from the Williamson-Hall plots as a slope of the linear fit (equation (6.3)).

Table 6-1. CFO crystallite size and lattice strain estimation using Scherrer's equation and Williamson-Hall plots.

		Crystallite size and lattice strain from XRD	
Atmosphere	Sintering temperature (°C)	D (nm)	ϵ_{str}
Air	1200	28	0.000446
	1300	26	0.000579
	1400	25	0.000615
N ₂	1200	26	0.000504
	1300	25	0.000585
	1400	26	0.000276

There was very little difference in the crystallite size between the samples sintered at different temperatures and atmospheres. The estimated crystallite size was calculated to be within the range of 25-30 nm, however, this is too low for the ceramics prepared by solid-state reaction.

The lattice microstrain, on the other hand, increased with increasing temperature, apart from the CFO 1400°C N₂ pellet, which has a notable amount of monoxide phase present, potentially inducing microstrain relaxation.

6.2.1.2 Rietveld refinement

The XRD pattern of CFO calcined powder was analysed by Rietveld Refinement using GSAS/EXPGUI software (Toby, 2001, Larson, 2000). The obtained CFO pattern together with the background, calculated and difference fits from the refinement are shown in Figure 6-11.

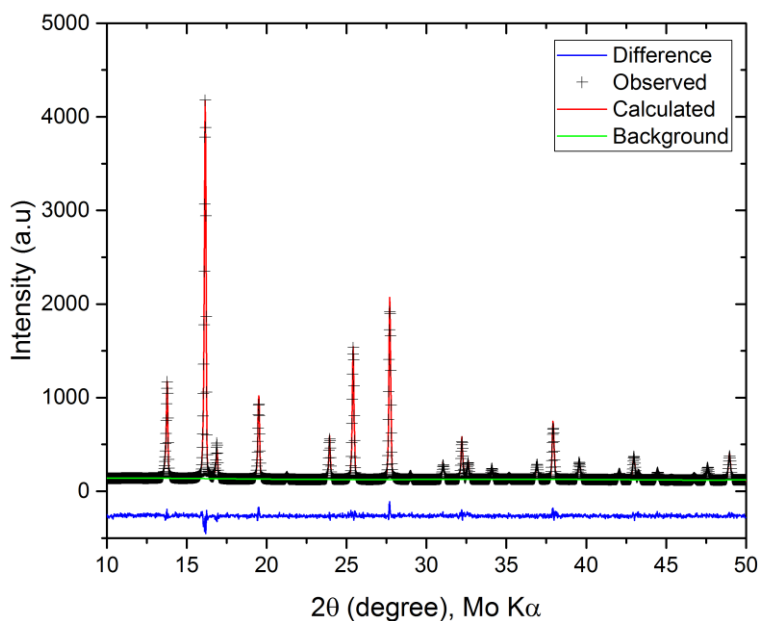


Figure 6-11. Rietveld refinement profile of the powder XRD pattern obtained for CoFe_2O_4 synthesised via solid state reaction.

The Rietveld structural refinement of XRD data can be a useful technique for determining the cation distribution at crystallographically distinct tetrahedral and octahedral sites of spinel materials (8a and 16d, respectively). During the refinement, the constraints were set for cations' x , y , z -positional coordinates, isotropic thermal parameters (U_{iso}) and site occupancy fractions to obtain reasonable results. The occupancy of O atoms was fixed to 1 and excluded from the refinement due to XRD's lower sensitivity to oxygen (Sahu and Panigrahi, 2011, Yaremchenko et al., 2017).

The refinement confirmed a mixed spinel structure with Co^{2+} predominantly occupying T_d sites. The parameters obtained from the Rietveld refinement of the calcined CFO powder are summarised in Table 6-2.

The cation distribution gives an overall formula of $\text{Co}_{0.58}\text{Fe}_{0.9}\text{O}_4$ which would mean that the spinel structure is closer to normal than inverse. However, due to the X-ray scattering factor of Co being very close to that of Fe, it is difficult to determine the Co^{2+} and Fe^{3+} cation distribution across T_d and O_h sites using XRD (Skolnick et al., 1958).

Table 6-2. The structural parameters of CoFe_2O_4 inverse spinel material obtained from Rietveld refinement of XRD pattern in Figure 6-11.

CoFe₂O₄, space group: $Fd\bar{3}m$ (cubic), $a = 8.3933 \pm 0.00012 \text{ \AA}$, Density = 5.251 g cm^{-3}

Atom	Wyckoff	X	Y	Z	Occupancy	$U_{\text{iso}} (\text{\AA}^2)$
$\text{Fe}_{\text{tet}}^{3+}$	8a	0.125	0.125	0.125	0.1971	0.00905
$\text{Co}_{\text{tet}}^{2+}$	8a	0.125	0.125	0.125	0.8029	0.00905
$\text{Fe}_{\text{oct}}^{3+}$	16d	0.5	0.5	0.5	0.2539	0.01056
$\text{Co}_{\text{oct}}^{2+}$	16d	0.5	0.5	0.5	0.7461	0.01056
O	32e	0.25654	0.25654	0.25654	1.00	0.00895

The quality indicators were $R_{\text{wp}} = 7.87\%$, $R_p = 6.14\%$ and $\chi^2 = 1.09$. The tetrahedral ($\text{Fe}_{\text{tet}}\text{-O}$) and octahedral ($\text{Fe}_{\text{oct}}\text{-O}$ and $\text{Co}_{\text{oct}}\text{-O}$) bond lengths were 1.9123 and 2.0448 \AA , respectively.

The same refinement strategy was used for powder XRD analysis of crushed pellet samples. The XRD refinement was continuous until convergence with a refinement quality factor, χ^2 , close to 1 was achieved. The results are presented in Table 6-3.

The refinement of the Co and Fe cation distribution over the A and B sites in the spinel CFO was performed; however, distinguishing between two neighbouring atoms, like Co ($Z=27$) and Fe ($Z=26$), is usually difficult due to the small contrast of X-ray scattering among these atoms (Mackay and Henderson, 2017, Cheetham and Wilkinson, 2003, Gomes et al., 2005). Therefore, it is even more challenging to differentiate between the oxidation states of adjacent cations. X-ray photoelectron spectroscopy was used as a complimentary technique to XRD to understand the cation distribution of the CFO compounds.

The lattice volume was calculated from the lattice parameter, a , see Table 6-3. The refinement results showed a small, non-linear change in the lattice volume of the CFO samples. It initially increased with increasing temperature (1200 to 1300°C) and then began to decrease for the 1400°C samples. These volumetric changes often occur in oxides with variable-valence cations in response to a compositional change, such as oxygen non-stoichiometry.

Since spinel materials are prone to losing oxygen at higher sintering temperatures, the results were expected to show the expansion of the cell volume as the processing temperature increased. On the contrary, the samples sintered at 1400°C (both air and N_2) had lower cell volume than those from 1300°C. The tetrahedral and octahedral hopping distances, d_A and d_B , followed the same trend. The changes in the bond lengths, however, could explain these variations. For 1400°C Air samples there was a noticeable decrease in the tetrahedral (d_{Ax}) and an increase in octahedral (d_{Bx}) bond lengths. For the

corresponding N_2 sample, bond lengths changed in reverse; possibly due to the effect of the lower oxygen partial pressure ($p\text{O}_2$) and secondary phase formation. A small amount of secondary phase is also present in 1300°C N_2 samples, previously shown in Figure 6-9. Moreover, these results suggest that the effect of the sintering atmosphere on the unit cell volume was greater than the effect of the temperature. Unexpectedly, the unit cell parameters were lower for the samples prepared in low $p\text{O}_2$ than in air. The cause of this is not fully understood and requires further, more in-depth investigation, preferably using neutron diffraction, to explain these variations and provide more sensitive information about the cation distribution and oxygen non-stoichiometry.

Since an inverse spinel is defined as containing 100% of its Co in Oh sites ($\gamma=1$) whereas a normal spinel has 100% in Td sites ($\gamma=0$), the spinel inversion parameter, γ , can be obtained from the occupation of the cobalt octahedral sites, in this case Co^{2+} $16d$ (Aghavnian et al., 2015). From the Rietveld refinement data the percentage of Co^{2+} in Oh sites across the three temperatures (1200 , 1300 and 1400°C) was found to be 87.7%, 77.2% and 32.9%, and 38.0%, 36.0% and 42.0% for air and N_2 sintering atmospheres, respectively.

Table 6-3. Crystallographic data obtained from Rietveld structural analysis of the powder XRD data of CFO crushed pellet samples.

	CoFe ₂ O ₄					
	Air			N ₂		
Sintering temperature (°C)	1200	1300	1400	1200	1300*	1400*
a (Å)	8.3832 ±0.00012	8.3846 ±0.00014	8.3840 ±0.000092	8.3548 ±0.0013	8.3567 ±0.00014	8.3469 ±0.00024
Cell volume (Å ³)	589.16 ±0.025	589.45 ±0.030	589.32 ±0.019	583.19 ±0.027	583.59 ±0.030	581.53 ±0.050
u (Å)	0.25732	0.25721	0.25649	0.25617	0.25548	0.25877
Site occupancy						
Co ²⁺ 8a	0.5764	0.6625	0.1137	0.1223	0.1154	0.2582
Fe ³⁺ 8a	0.4237	0.3375	0.8863	0.877	0.8846	0.7418
Co ²⁺ 16d	0.8770	0.7721	0.3291	0.3795	0.3599	0.4200
Fe ³⁺ 16d	0.1230	0.2279	0.6709	0.6205	0.6401	0.5800
U _{iso} 8a	0.01033	0.00694	0.01203	0.01184	0.01289	0.01081
U _{iso} 16d	0.01045	0.00783	0.01291	0.00961	0.01294	0.01198
U _{iso} 32e	0.01050	0.00904	0.01288	0.01041	0.01359	0.01070
Density (g cm ⁻³)	5.383	5.372	5.273	5.336	5.329	5.367
d_A (Å)	3.6300	3.6306	3.6304	3.6177	3.6186	3.6143
d_B (Å)	2.9639	2.9644	2.9642	2.9539	2.9545	2.9511
d_{Ax} (Å)	1.9212	1.9201	1.9094	1.8981	1.8886	1.9340
d_{Bx} (Å)	2.0363	2.0375	2.0431	2.0385	2.0444	2.0162
R _p (%)	9.1	10.37	6.35	8.72	9.51	13.24
R _{wp} (%)	12.02	13.37	8.19	11.26	12.24	17.07
χ^2	0.9586	0.9520	0.9687	0.891	0.983	1.004

* Non-single-phase materials; refined using Spinel ($Fd\bar{3}m$) and Wüstite ($Fm\bar{3}m$) structures. d_A is the hopping length for tetrahedral site ($d_A = 0.25a\sqrt{3}$) and d_B ($d_B = 0.25a\sqrt{3}$) is the hopping distances for octahedral site, and d_{Ax} and d_{Bx} are the tetrahedral and octahedral bond lengths, respectively.

6.2.2 X-ray photoelectron spectroscopy

X-ray photoelectron spectroscopy (XPS) spectra were obtained for the six CFO samples mentioned previously in XRD and Raman (see later) in sections 6.2.1 and 6.2.3, respectively. The wide-scan surveys were obtained for all samples up to 1000 eV to

reveal the presence of any impurities (Figure 6-12 (a))⁵. Apart from carbon, there were negligible amounts of Na and Mg impurities present on the surface of some of the samples.

The ratios of Co/Fe were calculated from the Co2p and Fe2p peak areas after subtracting Shirley-type background from the wide-scan spectra. The peak areas were corrected using corresponding Scofield factors (19.16 for Co and 16.42 for Fe). Across the 1200-1400 °C sintering temperature range the Co:Fe ratios were 0.50, 0.50, 0.49 for air samples, and 0.50, 0.49, 0.50 for N₂.

The high resolution spectra measured for Co2p, Fe2p and O1s are presented in Figure 6-12 (b-d). Co and Fe spectra contained four main components: two peaks associated with the 2p_{1/2} and 2p_{3/2} spin-orbit splits and two corresponding satellite shake-up peaks for both metals. The satellite peaks are the result of photoionisation of a 3d electron into an unoccupied 3d or 4s level above the Fermi level (Freund et al., 1983)

XPS data was used to provide stoichiometric information about the cation distribution in the CFO samples sintered at different temperatures. Because the XPS peaks of the cobalt and iron overlap significantly, deconvolution of the spectra must be performed to separate the 2p_{1/2} and 2p_{3/2} peaks and their corresponding satellites, as shown in the Figure 6-12 (b and c).

The Shirley-type background was fitted to all spectra and the Fe 2p, Co 2p and O 1s spectral line shapes were fitted to the combined Gaussian–Lorentzian (70/30%) functions. All parameters were taken into account when performing the XPS analysis – background, spin-orbit components (2p_{1/2} and 2p_{3/2}) and shake-up satellites, as suggested by Aghavnian et al. (2015).

⁵ The XPS spectra for the 1200 °C air sample is shown in Figure 6-12 to show the absence of other elements in the wide scan and the success of fitting. The spectra of other samples were fitted using same parameters.

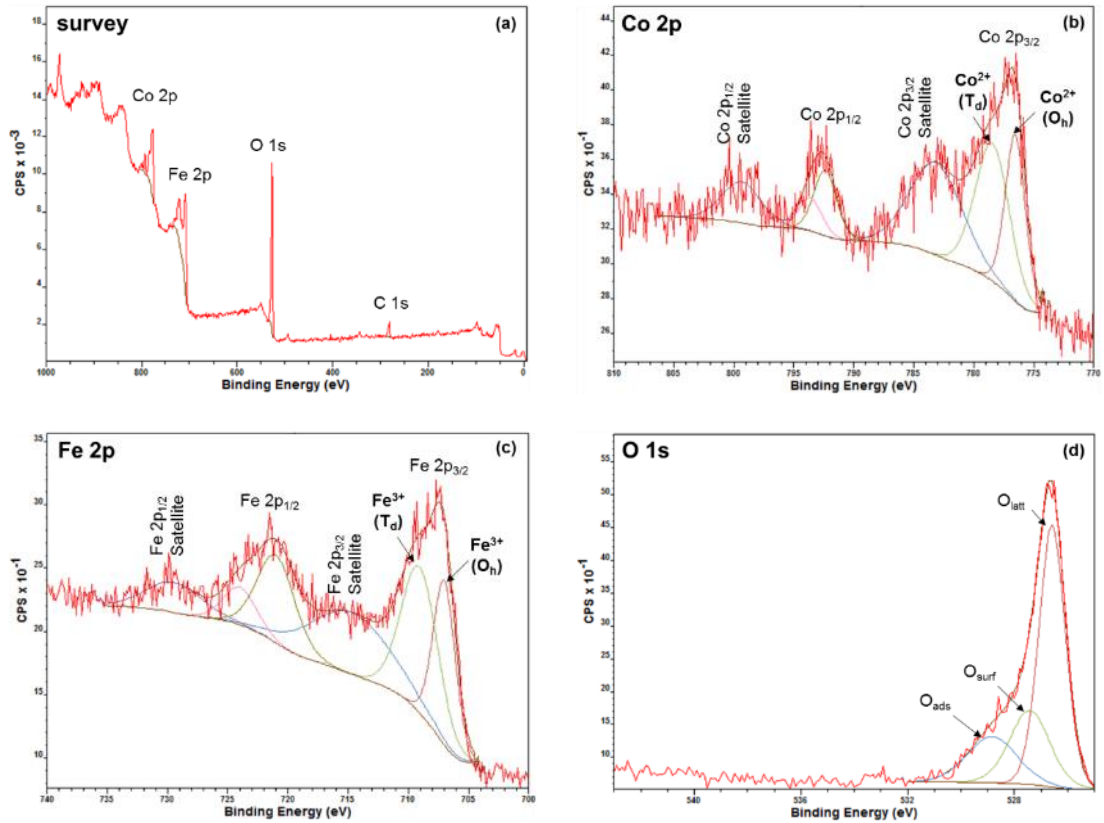


Figure 6-12. XPS spectra of CoFe_2O_4 sintered at 1200°C for 2 hours in air in different regions: (a) survey, (b) Co 2p, (c) Fe 2p and (d) O 1s.

XPS results confirmed that the samples were mixed spinels with Co^{2+} and Fe^{3+} occupying both the tetrahedral A-sites and the octahedral B-sites. The main $\text{Co}2p_{3/2}$ peak was fitted with two peaks corresponding to $\text{Co}2p_{3/2} \text{Oh}$ (776.52 eV) and $\text{Co}2p_{3/2} \text{Td}$ (778.43 eV). Similarly, the $\text{Fe}2p_{3/2}$ was decomposed to $\text{Fe}2p_{3/2} \text{Oh}$ (707.01 eV) and $\text{Fe}2p_{3/2} \text{Td}$ (709.06 eV). The Co/Fe ratio was recalculated from the deconvoluted spectra and gave slightly higher ratios than from the ones obtained from the wide scan:

- 0.56, 0.49 and 0.58 for 1200, 1300 & 1400 $^\circ\text{C}$ air samples, respectively
- 0.68, 0.55 and 0.56 for 1200, 1300 & 1400 $^\circ\text{C}$ N_2 samples, respectively

The occupation percentage of the Co^{2+} in Oh sites was used to determine the inversion parameter of the spinel (γ), the same as in Section 6.2.1.2. The $\text{Co}2p_{3/2}$ spin-orbital regions were chosen over the $\text{Co}2p_{1/2}$ because of the higher signal intensity resulting in better fitted Gaussian/Lorentzian functions. The same analysis methodology was used by Aghavnian et al. (2015).

The γ percentage values were found to be 41.9, 66.7, 66.7%, and 49.4, 38.1 and 21.0% for air and N_2 samples, respectively (1200, 1300 & 1400 $^\circ\text{C}$). These values are different

to the ones obtained from the XRD refinement (apart from the 1300 °C N_2 sample that is within 6% error region).

The peak areas of $\text{Co}2\text{p}_{3/2}$ and $\text{Fe}2\text{p}_{3/2}$ from the Co and Fe spectra were used to calculate the Co and Fe atomic percentage in O_h and T_d sites. The binding energy positions of fitted peaks and the corresponding atomic percentages are summarised in Table 6-4.

Table 6-4. XPS binding energy positions and atomic percentages of Co and Fe for CFO samples.

Sintering temperature (°C)	Spectrum	Assignment	Air		N_2	
			BE (eV)	Atomic percentage (%)	BE (eV)	Atomic percentage (%)
1200	Co $2\text{p}_{3/2}$	$O_h \text{Co}^{2+}$	776.52	42%	776.68	49%
		$T_d \text{Co}^{2+}$	778.43	58%	778.94	51%
	Fe $2\text{p}_{3/2}$	$O_h \text{Fe}^{3+}$	707.01	41%	707.00	44%
		$T_d \text{Fe}^{3+}$	709.06	59%	709.21	56%
1300	Co $2\text{p}_{3/2}$	$O_h \text{Co}^{2+}$	776.88	67%	779.26	38%
		$T_d \text{Co}^{2+}$	779.11	33%	780.92	62%
	Fe $2\text{p}_{3/2}$	$O_h \text{Fe}^{3+}$	706.98	35%	709.83	46%
		$T_d \text{Fe}^{3+}$	709.02	65%	711.96	54%
1400	Co $2\text{p}_{3/2}$	$O_h \text{Co}^{2+}$	777.15	67%	779.38	21%
		$T_d \text{Co}^{2+}$	779.53	33%	780.74	79%
	Fe $2\text{p}_{3/2}$	$O_h \text{Fe}^{3+}$	707.31	39%	709.86	31%
		$T_d \text{Fe}^{3+}$	709.26	61%	711.44	69%

The oxygen 1s core photoelectron region contained three peaks, corresponding to the lattice, surface and adsorbed oxygen (Zhou et al., 2008).

6.2.3 Raman spectroscopy

Raman spectroscopy (RS) is a useful, non-destructive technique that can provide information about the structure of spinel compounds. It is a highly sensitive tool for analysis of lattice effects, such as phase transition, distortion, magnetic ordering and local cation distribution (Chandramohan et al., 2011). The effect of cation distribution on Raman spectra of spinels is well documented in literature (Ivanov, 2010). However, Raman spectra can be complicated by the cation exchange between tetrahedral and octahedral sites that has been linked to the sample treatment conditions (Laguna-Bercero et al., 2007).

The cubic inverse/mixed spinel structure of cobalt ferrite with space group $Fd\bar{3}m$ and O_h^7 symmetry presents 42 degrees of freedom, consisting of 39 optical modes and three acoustic modes. The phonon modes of a spinel structure are: A_{1g} , E_g , $3T_{2g}$, $4T_{1u}$, T_{1g} , $2A_{2u}$, $2E_u$ and $2T_{2u}$ (White and DeAngelis, 1967), of which only five are Raman active, namely A_{1g} , E_g and $3T_{2g}$. The cation redistribution in the T_d and O_h sites lowers the symmetry of the crystal structure and exhibits additional phonon modes. Figure 6-13 shows the Raman spectra of the pellet samples sintered in air and under nitrogen. Deconvolution of the Raman spectra of the samples treated in air showed six peak maxima at 186.3, 300.6, 459.8, 533, 606.0 and 681.9 cm^{-1} , respectively (Table 6-5). These peaks were assigned to the corresponding phonon modes: $T_{1g}(1)$, E_g , $T_{1g}(2)$, $T_{1g}(2)$, $A_{1g}(1)$ and $A_{1g}(2)$ in accordance with the literature (Chandramohan et al., 2011). The deconvolved Raman spectra of the 1200°C N_2 sample appeared similar to the previously described ones. The two remaining samples sintered in N_2 (1300 and 1400°C) had three additional peaks at 218.2, 311.4 and 402.3 cm^{-1} (see Figure 6-13). These peaks are consistent with the Raman peaks characteristic to $\alpha\text{-Fe}_2\text{O}_3$ (hematite), suggesting an iron-rich shell formation (Chandramohan et al., 2011). The presence of hematite features only in the passivated cobalt ferrite Raman spectra suggests that the passivation process allows the formation of an iron rich shell around the nanoparticles (Chandramohan et al., 2011, Melo et al., 2006).

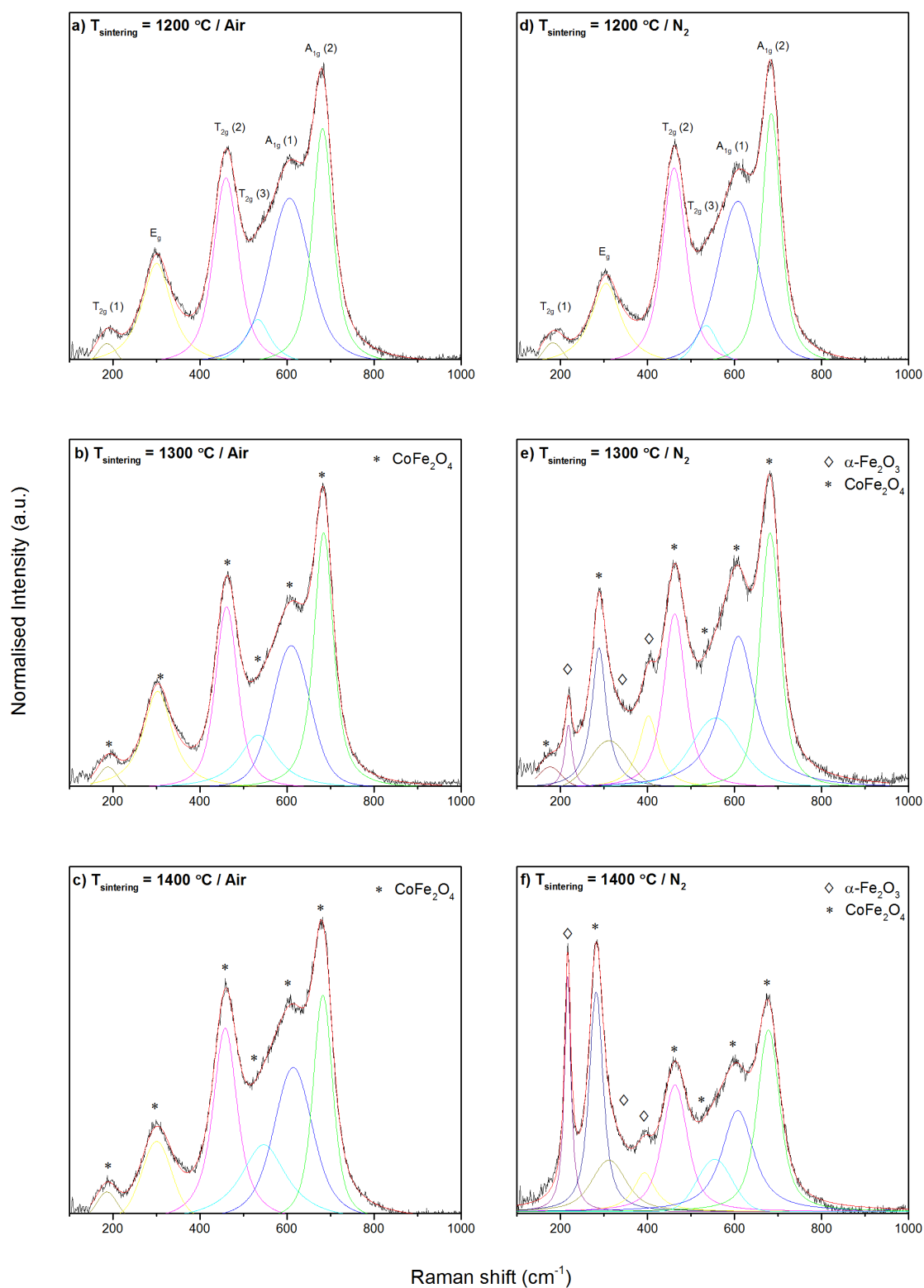


Figure 6-13. Raman spectra of CoFe_2O_4 sintered at different temperatures and atmospheres.

Table 6-5. Raman phonon modes of CoFe_2O_4 sintered at different temperatures and atmospheres.

		Raman shift (cm^{-1})											
		CoFe ₂ O ₄						α-Fe ₂ O ₃			Goodness of fit		
Atmosphere	Sintering temperature (°C)	T _{1g} (1)	E _g	T _{1g} (2)	T _{1g} (2)	A _{1g} (1)	A _{1g} (2)	A _{1g}	E _g (1)	E _g (2)	χ ²	R ²	
Air	1200	186.3	300.6	459.8	533	606	681.9	-	-	-	1.15	0.998	
	1300	188.6	303.1	461.2	533.7	609.8	684.3	-	-	-	1.01	0.998	
	1400	186.4	300.8	458.00	546.55	614.4	682.6	-	-	-	1.27	0.998	
N ₂	1200	182.0	304.7	461.1	534.5	607.8	684.4	-	-	-	1.08	0.998	
	1300	176.0	288.58	462.5	556.6	608.6	681.8	218.2	311.4	402.3	1.95	0.997	
	1400	-	282.00	463.1	554.3	607.5	678.00	216.6	311.4	393.00	2.80	0.994	

6.2.4 Scanning electron microscopy (SEM)

Figure 6-14 to Figure 6-17 show the surfaces of the CFO samples annealed at 1200, 1300 and 1400 °C in air and 1300°C in N_2 . The grain size of the samples sintered in air increases with an increase in temperature. This is clearly visible in Figure 6-14(b), Figure 6-15(b) and Figure 6-17(b), with a grain size of less than 4 μm diameter for the 1200 °C sample, reaching approximately 20 μm for 1400 °C. The concentration of the oxygen ion vacancies is often responsible for the grain growth kinetics and the magnetic properties of the spinel materials (Honig, 2012). Both the grain size and pore distribution are highly important for achieving the desired material properties.

Ceramic oxides, particularly transition metal oxides such as CFO, the sintering temperature and oxygen partial pressure ($p\text{O}_2$) can have an effect on the type and concentration of lattice defects and, therefore, the overall stoichiometry of the material (Somiya et al., 2003). A study by Rahaman (2017) showed that the $p\text{O}_2$ has a significant effect on the grain growth: smaller grain sizes were obtained at high $p\text{O}_2$, whereas low $p\text{O}_2$ results in a larger grains. The exact mechanism of the grain growth is not fully understood; however, it was suggested that pore mobility is controlled by oxygen lattice diffusion. Here, the interaction between the pores and grain boundaries controls the kinetics of the grain growth (Brook, 1969, Liu et al., 2010).

The grain size of CFO sintered in nitrogen at 1300 °C is between the two air samples and hence consistent with the previous statements. At low $p\text{O}_2$ the lattice oxygen ions are easily released from the oxides, forming oxygen vacancies and enhancing sintering of the material (Somiya et al., 2003). Moreover, oxygen vacancy formation affects the solid-state transport of oxygen ions and electrons within the metal oxide, resulting in higher ionic and electronic conductivities (Ajroudi et al., 2014).

Figure 6-17 and Figure 6-18 show the same sample (1300 °C N_2) before and after a thermal etching procedure described in Section 3.2.8.1. Thermally etched samples showed the presence of small growths across the whole sample, suggesting the formation of a secondary phase, most likely a rock-salt of FeO or CoO. The formation of $\text{Fe}_x\text{Co}_{1-x}\text{O}$ is not excluded.

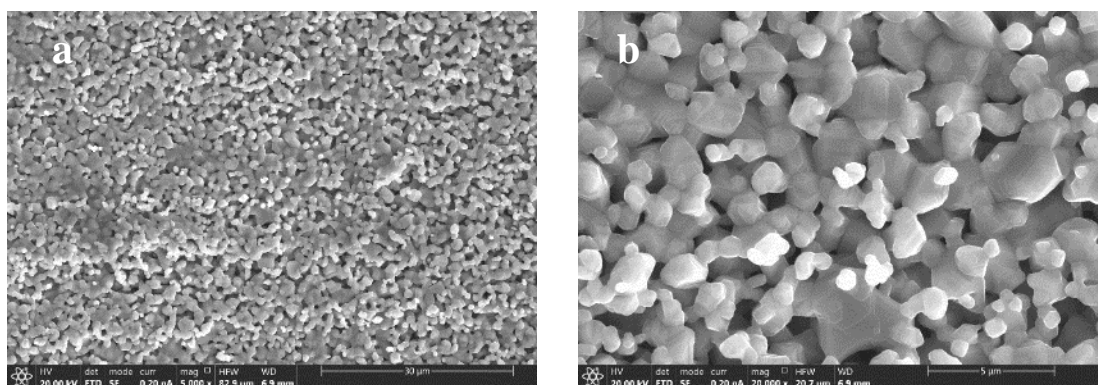


Figure 6-14. SEM images of CFO sintered at 1200°C for 2h in air at x5,000 (a) and x20,000 (b) magnification.

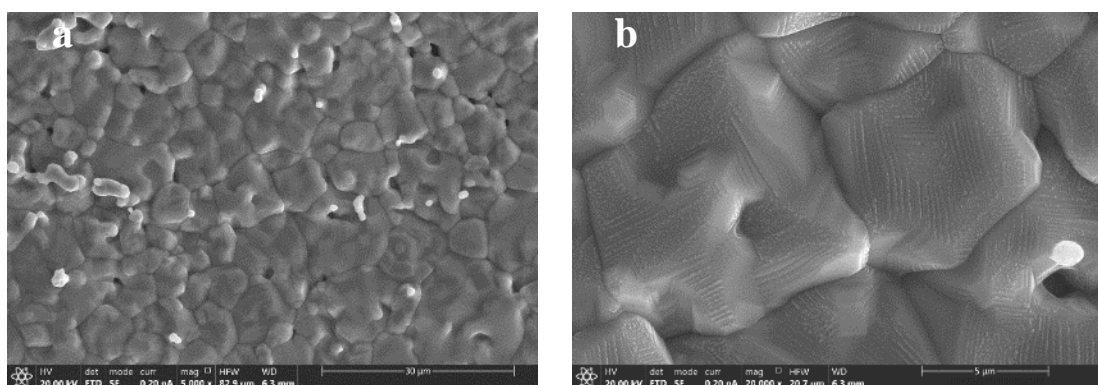


Figure 6-15. SEM images of CFO sintered at 1300°C for 2h in air at x5,000 (a) and x20,000 (b) magnification.

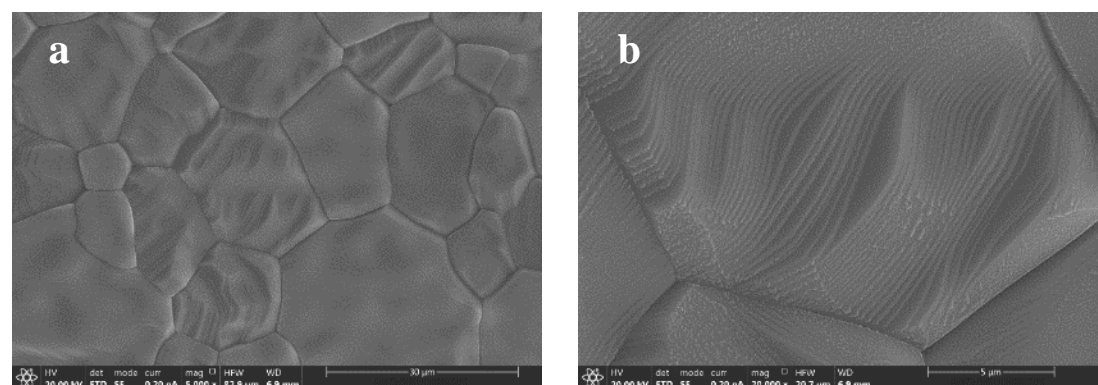


Figure 6-16. SEM images of CFO sintered at 1400°C for 2h in air at x5,000 (a) and x20,000 (b) magnification.

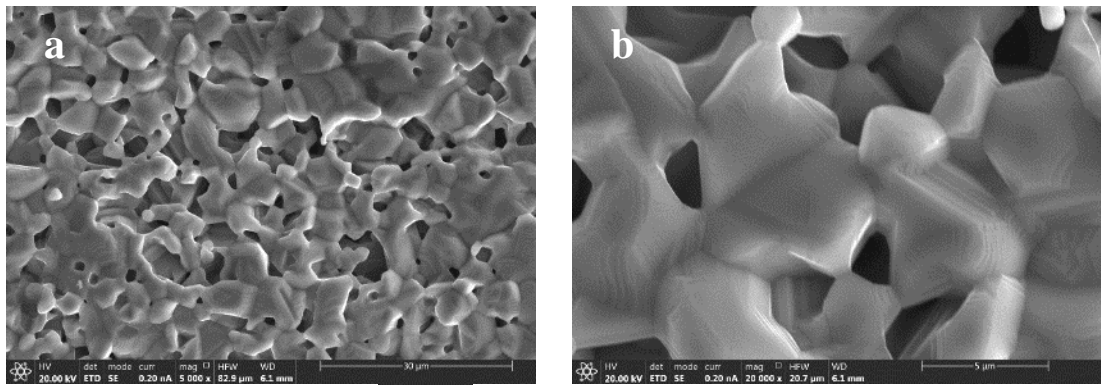


Figure 6-17. SEM images of CFO sintered at 1300°C for 2h under flow of N_2 at x5,000 (a) and x20,000 (b) magnification.

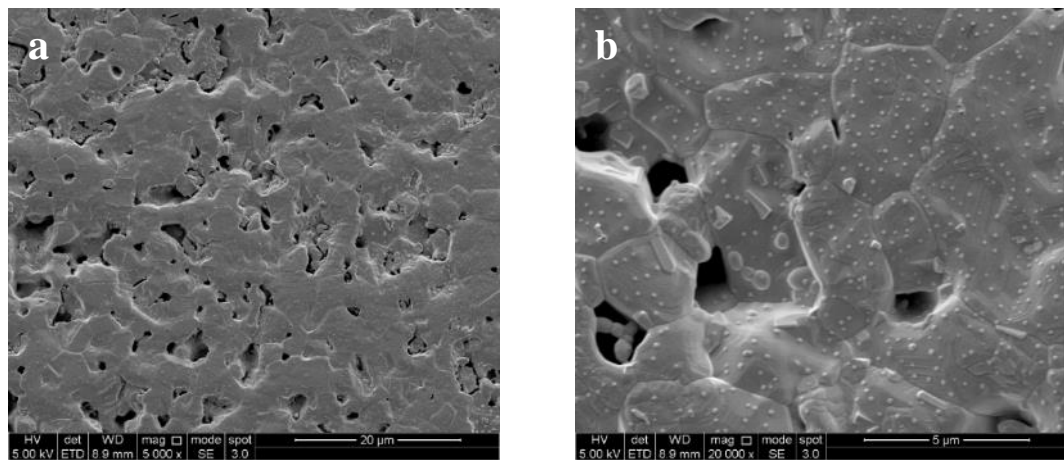


Figure 6-18. SEM images of CFO sintered at 1300°C for 2h under flow of N_2 at x5,000 (a) and x20,000 (b) magnification with additional features appearing after thermal etching.

6.3 Electrical properties

6.3.1 Conductivity

Electrical conductivity is the ability of a material to carry a flow of an electric current and is the reciprocal of the electrical resistivity and is an important parameter for the development of the SOC components.

4 probe dc conductivity and Seebeck coefficient measurements were carried out simultaneously on the series of CFO samples sintered in different atmospheres – in air

and under a flow of N_2 at 1200⁶, 1300 and 1400 °C. The obtained results are shown in Figure 6-19.

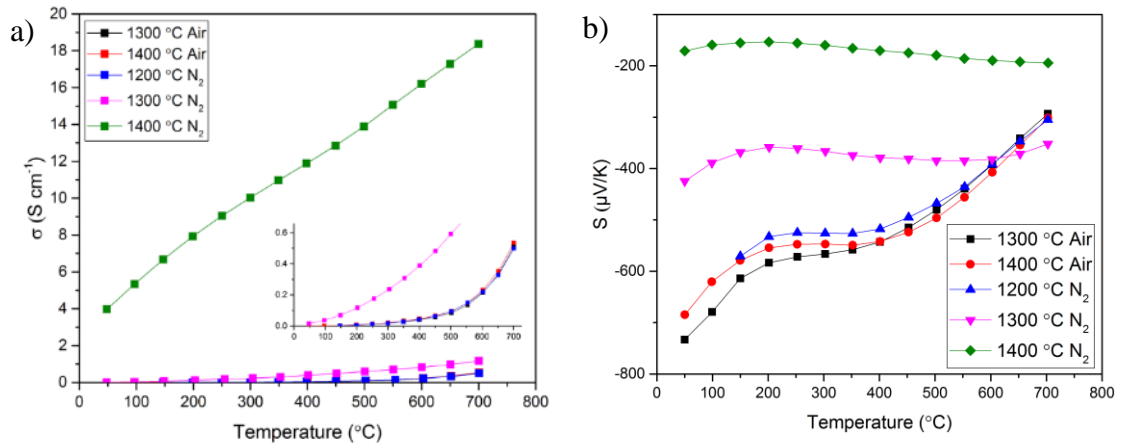


Figure 6-19. Plots of electrical conductivity (a) and Seebeck coefficient (b) against temperature for CFO samples measured in Ar.

All samples showed a trend of increasing dc conductivity with an increase in sintering temperature. As expected, the samples sintered in low pO_2 showed significantly higher conductivity compared to the samples sintered in air at the same temperatures: from 0.509 to 0.535 S cm^{-1} and from 0.499 to 18.37 S cm^{-1} for air and N_2 , respectively. 1400 °C N_2 sample was *c.a.* 34 times more conductive than the same temperature sample sintered in air. This increase in conductivity may be attributed to the oxygen-loss from the spinel phase and/or to the presence of the secondary rock-salt phase formation previously identified during XRD measurements.

Figure 6-20 shows electrical conductivities plotted as an Arrhenius plot: the natural logarithm of σ versus $1000/T$. The activation energy, E_a , is determined using the relation below:

$$\sigma = \sigma_0 e^{-\frac{E_a}{kT}} \quad (6.4)$$

⁶ The 1200 °C air sample showed very low conductivity, close to the detection limit of the equipment, therefore, the result was not repeatable hence was excluded from the overall trend.

where E_a is the activation energy, σ is the conductivity at temperature T , σ_0 a temperature independent constant, and k the Boltzmann constant ($1.38 \times 10^{-23} \text{ m}^2 \text{ kg s}^{-2} \text{ K}^{-1}$). The obtained value is then divided by $1.602 \times 10^{-19} \text{ J}$ to convert Joules (J) to electron-volts (eV).

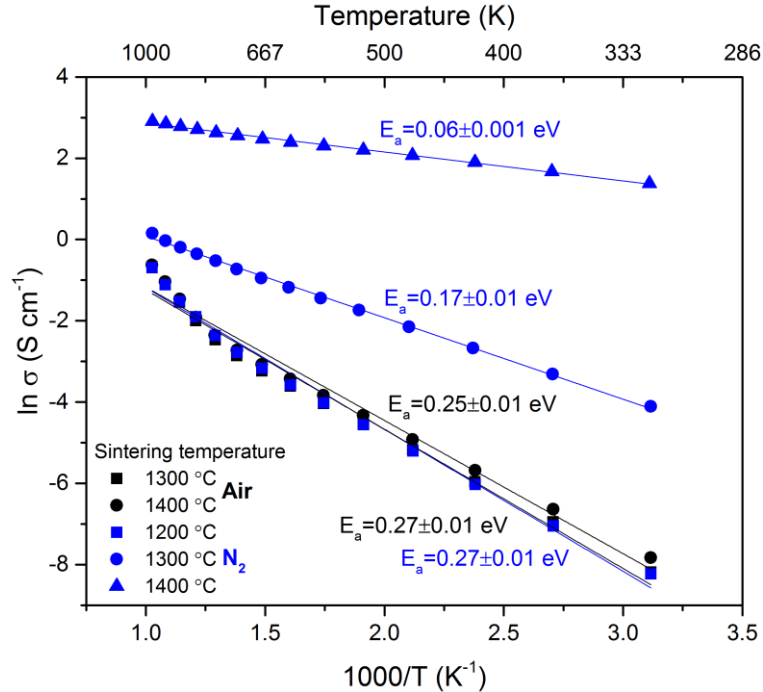


Figure 6-20. The temperature dependence of the DC electrical conductivities for CFO samples under different sintering atmospheres.

There was a minimal change (within errors) in the activation energy between the two air samples with increasing temperature. The E_a appeared almost the same for 1300 °C air and 1200 °C N_2 samples, equal to 0.27 ± 0.01 for both. The changes in E_a of N_2 sintered samples, however, were more significant: 0.27, 0.17 and 0.06 eV for 1200, 1300 and 1400 °C samples, respectively.

The data in Figure 6-20 were fitted with linear trend lines, showing a good fit for the higher conductivity samples, however, it is more evident that the lower temperature samples have a change in slope around a Curie temperature of 793 K (Ajroudi et al., 2014). This change in slope is not accompanied by the inverse of Seebeck coefficient, therefore, is most likely undergoing a magnetic transition from ferromagnetic to paramagnetic (Shinde, 2013).

Due to the lower pO_2 in N_2 atmosphere, the samples sintered in N_2 are believed to have lost some lattice oxygen to create oxygen vacancies, resulting in a nonstoichiometric and

highly conducting CFO material. To maintain the charge neutrality of the sample, some of the Fe^{3+} ions have to reduce to Fe^{2+} ($\text{Fe}^{3+} + e^- \rightleftharpoons \text{Fe}^{2+}$) to maintain the overall charge neutrality. The Fe^{2+} ions occupy predominantly the O_h B-sites, leading to the increase in hopping of the electrons and the electrical conductivity of the CFO (Kumar et al., 2017).

It is apparent that the higher E_a values were associated with lower electronic conductivity of CFO. The density and porosity of the samples play an important role in conductivity of the spinels. A lower number of pores improves the diffusion resistance of the charge carriers transfer in the solid phase of CFO, therefore, higher densities give larger electrical conductivities (Mangalaraja et al., 2002). The overall trends in dc conductivity of samples sintered in air and N_2 atmospheres are in agreement with the results obtained by Liu et al. (2010) for NiFe_2O_4 spinels.

6.3.1.1 Seebeck coefficient

The temperature dependent Seebeck coefficient was measured to identify the electronic conduction mechanism in CFO. The results are presented in Figure 6-19 (b). Negative Seebeck coefficients were obtained for all CFO samples measured in this work apart from 1200 °C air sample, where a sign inversion in Seebeck voltage occurred. This sample was the least conductive out of the six samples tested. Poor conductivity can be explained by the low density of the sample (Figure 6-7) and higher porosity, as seen in the SEM images (Figure 6-14).

The negative Seebeck coefficient suggests that the dominating conduction mechanism is through the hopping of electron from Fe^{2+} to Fe^{3+} , giving rise to n-type semiconducting behaviour of CFO samples (Kumar et al., 2017).

6.4 CFO-SDC ceramic membranes for SOC application

In the previous section it was identified that CFO samples sintered in N_2 had the highest electronic conductivity. The 1200 °C N_2 sample had the lowest conductivity of the three sintering temperatures and 1400 °C N_2 contained a measurable amount of secondary rock-salt phase, therefore, the middle range temperature was chosen to be used for producing a symmetric CFO-SDC|SDC SOCs.

6.4.1 Phase analysis

CFO powder and SDC nanopowder in ratio 50/50 wt% were ball milled together for 6 hours in PIA to ensure homogeneous distribution of the two materials. After drying, the samples were calcined at different temperatures and analysed using XRD to examine for any secondary phase formation. The obtained XRD spectra obtained are presented in Figure 6-21.

The uncalcined CFO-SDC powder contained some very broad diffraction patterns that could be attributed to the nanosized material, in this case, SDC (Petkov and Shastri, 2010). No new phases were observed in the spectra. As the calcination temperature increased, crystallite growth was thermally promoted, resulting in narrower XRD peaks, particularly for SDC.

Figure 6-22 shows a higher resolution spectrum of the 1200 °C air sample that has both CFO and SDC phases indexed with Miller indices. Although no other phases were detected, the formation of a small amount of mixed CFO-SDC phase, similar to the one described by Harris et al. (2014) for CFO-GDC MIEC, could have gone unnoticed. Harris et al. (2014) used scanning transmission electron microscopy (STEM) coupled with electron energy loss spectroscopy (EELS) to simultaneously map the atomic/electronic structure of the elements at the grain boundaries to detect presence of the new phases of CFO-GDC.

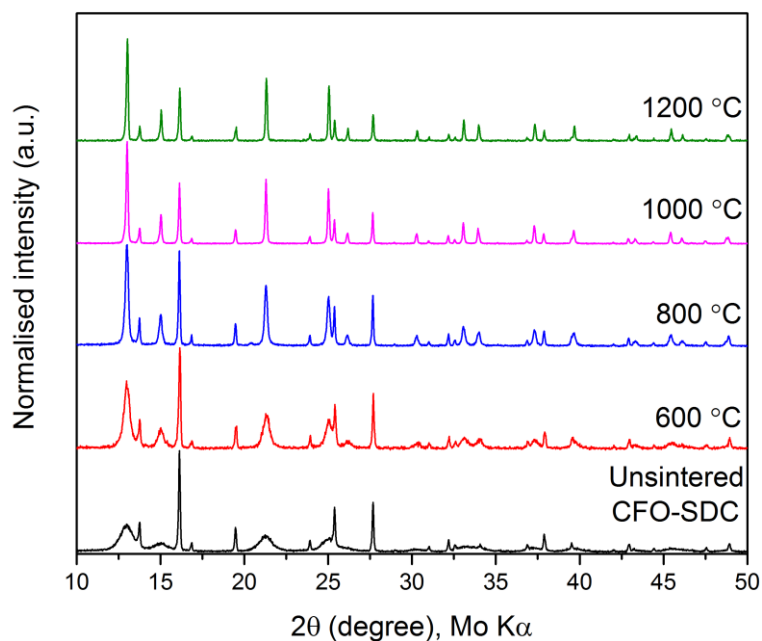


Figure 6-21. XRD spectra of 50/50 wt. % CFO-SDC powder calcined at different temperatures.

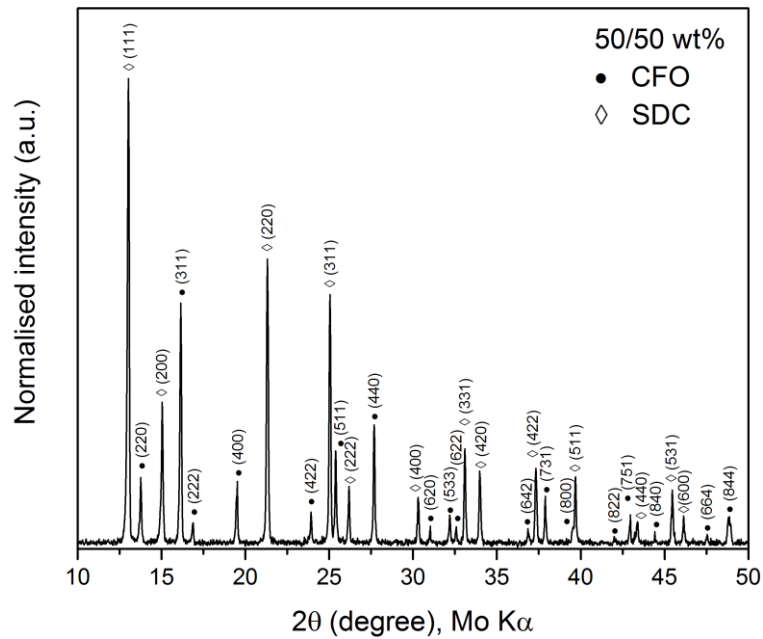


Figure 6-22. XRD spectra of 50/50 wt. % CFO/SDC precursor calcined at 1200 °C.

6.4.2 Thermal analysis

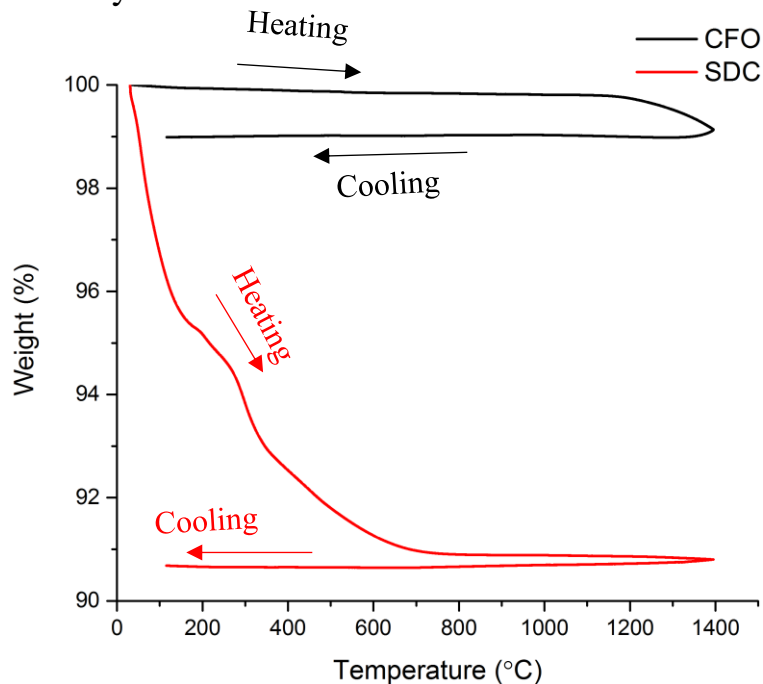


Figure 6-23. TGA curves for CFO powder and SDC nanopowder in N_2 .

The TGA curves of CFO and SDC heated in N_2 are shown in Figure 6-23. The CFO powder loses approximately 1% of the sample weight unlike SDC, which reduced in weight by almost 10%. The difference in the weight loss rate did not seem to affect the sintering of the sample, resulting in strong, dense MIEC pellets.

6.4.3 Electrical properties

The trends in electrical conductivity remain the same, compared with CFO samples, when SDC nanoparticles are added to the CFO and sintered in N_2 . The data were obtained by four probe dc conductivity measurement using Netzsch SBA 458 analyser. A significant discrepancy between the samples was observed for a sintering temperature of 1300 °C, as shown in Figure 6-24 (1300A & 1300B). The main cause could be the dispersion of the two phases, leading to larger or smaller interconnection between the electron-conducting CFO phases. All in all, the E_a reduced from 0.62 to 0.22 eV from 1200 to 1400 °C, respectively.

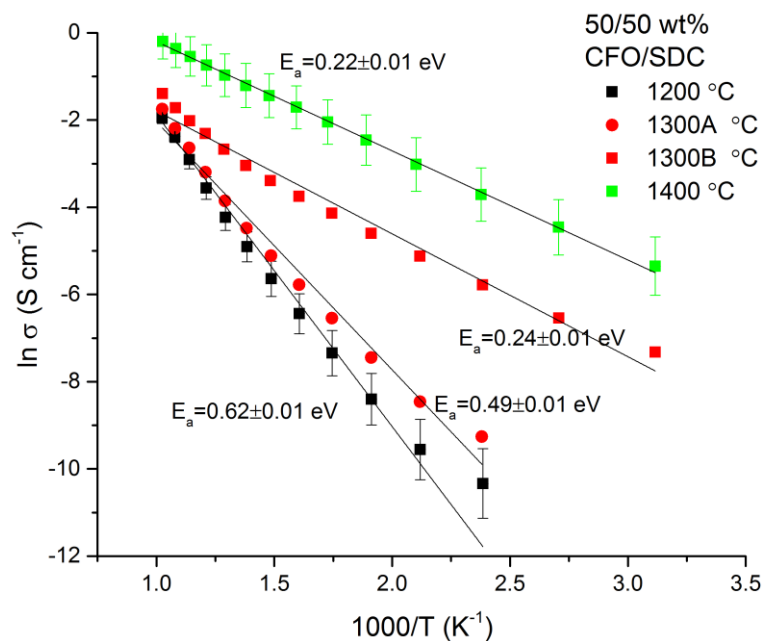


Figure 6-24. The Arrhenius plot of 50/50 wt. % CFO-SDC samples sintered in N_2 .

6.4.4 SEM analysis

SEM/EDX analysis in Figure 6-25 showed a uniform distribution of the two phases. The elemental maps of cerium and samarium (Figure 6-25 (e-d)) showed that some isolated “islands” of SDC were present. This can potentially be addressed through improved mixing and the addition of a dispersant. Alternatively, the materials could be measured by volume percent (50 vol% CFO / 50 vol% SDC).

The SEM micrograph with overlaid EDX maps is a good demonstration of how the two phases are interlinked and supports the reasoning for the variation in electronic conductivity of the CFO-SDC MIEC in Section 6.4.3.

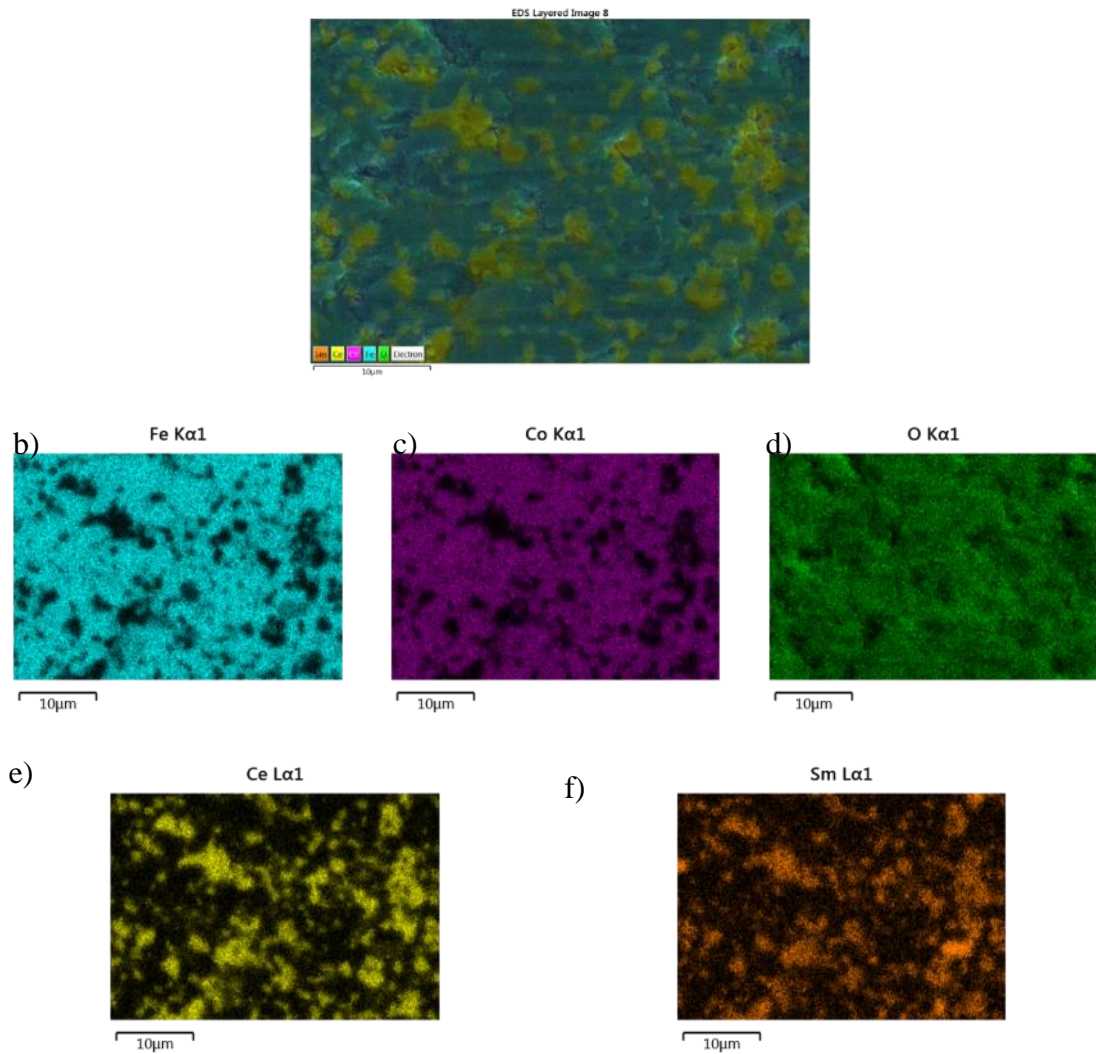


Figure 6-25. (a) SEM micrograph of 50/50 wt. % CFO/SDC sample sintered at 1300 °C in N_2 for 2 h and overlapped with elemental maps of Fe(b), Co(c), O(d), Ce and Sm(f).

6.4.5 Activity for CO_2/CO reduction

6.4.5.1 Current-voltage measurements

The potential sweeps, also known as i - V curves, were measured in the temperature range of 500–850 °C for a symmetrical cell with CFO-SDC electrodes sintered onto an SDC electrolyte at 1300 °C in N_2 . The cell preparation method and measurement parameters are described in detail in Section 3.3.2.

The i - V and EIS measurements collected between 50/50 and 70/30 CO_2/CO gas compositions, are shown in Figure 6-26 (a, b). The cell performed similarly in fuel cell and electrolysis modes. The graphs of the area specific resistance (ASR) in Figure 6-27 show lower values in fuel cell operation mode across the different atmospheres.

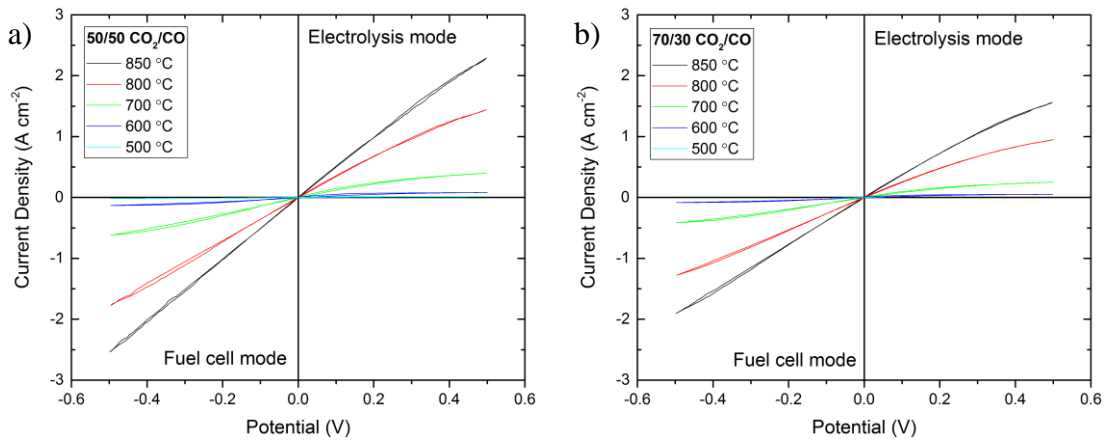


Figure 6-26. Potential sweep on the CFO-SDC|SDC|CFO-SDC symmetric cell at 850 °C in 50% CO_2/CO . The sweep was repeated 3 times and showed good reproducibility.

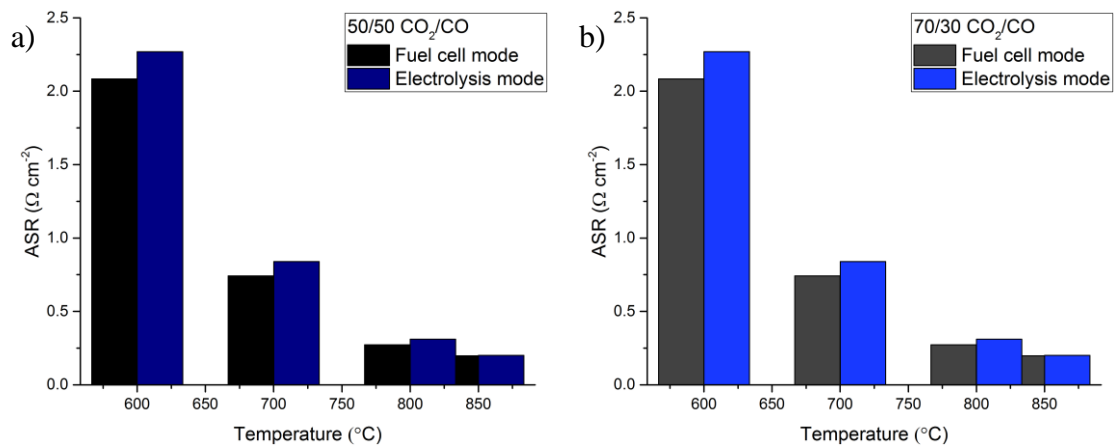


Figure 6-27 Comparison of the electrochemical performance the CFO-SDC|SDC|CFO-SDC symmetric SOC in terms of the ASR in fuel cell and electrolysis modes, and 50/50 (a) and 70/30 (b) CO_2/CO atmospheres.

ASRs of 0.20 and 0.29 $\Omega \text{ cm}^2$ were found for the reduction of CO_2 in CO_2/CO mixtures with a ratio of 50/50 and 70/30, respectively, at 850 °C. Similar ASR values were obtained for the CO oxidation activity (0.20 and 0.26 $\Omega \text{ cm}^2$).

Larger resistances were observed for the 70/30 CO_2/CO atmosphere compared to 50/50 across all measurements. A comparison of the ASR for different atmospheres is shown in Figure 6-28. One of the reasons for such behaviour may be partial oxidation of the oxygen deficient CFO by CO_2 , leading to higher electrode resistances.

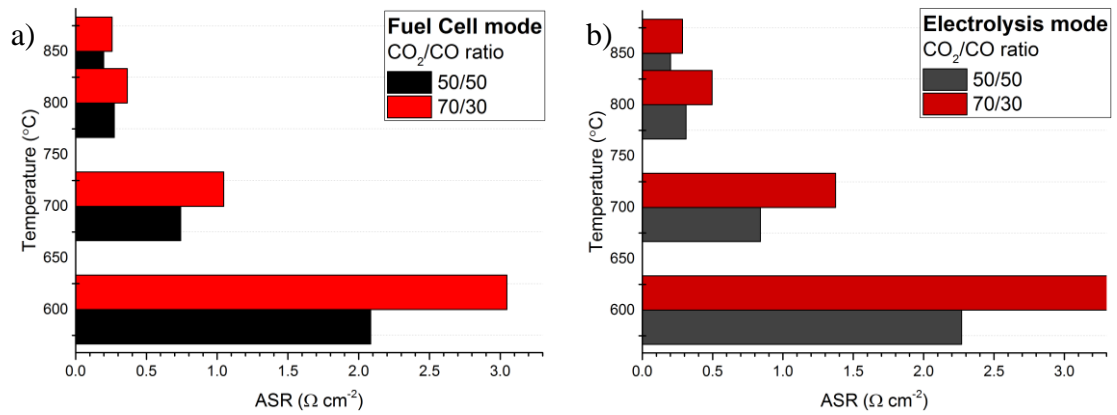


Figure 6-28. Comparison of the electrochemical performance the CFO-SDC|SDC|CFO-SDC symmetric SOC in terms of the ASR in 50/50 and 70/30 CO_2/CO atmospheres, and fuel cell (a) and electrolysis (b) testing modes.

The material has the potential to operate at lower temperatures; however, this would require reducing the thickness of the electrolyte to reduce the ASR. Thinner electrolytes can be made by tape casting and laminated into a thick film or onto the porous electrode support.

6.4.5.2 EIS measurements

Impedance data were collected prior to the current-voltage sweeps, across 500–850 °C temperature range, and are shown in Figure 6-29 (50/50 CO_2/CO) and Figure 6-30 (70/30 CO_2/CO). The EIS spectra were fitted with equivalent circuits to extract the resistance and capacitance values associated with the SOC electrode and electrolyte components. The equivalent circuits are also shown in Figure 1-29.

The EIS spectra at 800 and 850 °C showed only one arc and were fitted with a resistor in series with a parallel R-CPE element ($R_0-(R_2\text{-CPE}2)$), where R_0 was used to model the electrolyte and $R_1\text{-CPE}1$ and $R_2\text{-CPE}2$ to model possible electrode contributions to EIS data. At 700 °C and below, another arc was measured in the high frequency region and fitted using an additional R-CPE element.

At 600 °C, the capacitance values of the high frequency arc were obtained using the peak of the arc, where $\omega RC=1$, and were equal to $9.84\text{E-}05$ and $9.46\text{E-}05$ F cm^{-2} for 50/50 and 70/30 CO_2/CO ratios, respectively. Such high capacitance values imply that the arc is associated with electrode processes (Irvine et al., 2004). The resistance and capacitance values obtained from EIS fitting are summarised in Table 6-6 and Table 6-7. As the

temperature increases the resistances R_0 , R_1 and R_2 decrease and capacitances C_1 and C_2 increase, where 1 refers to high frequency region and 2 to low frequency arc.

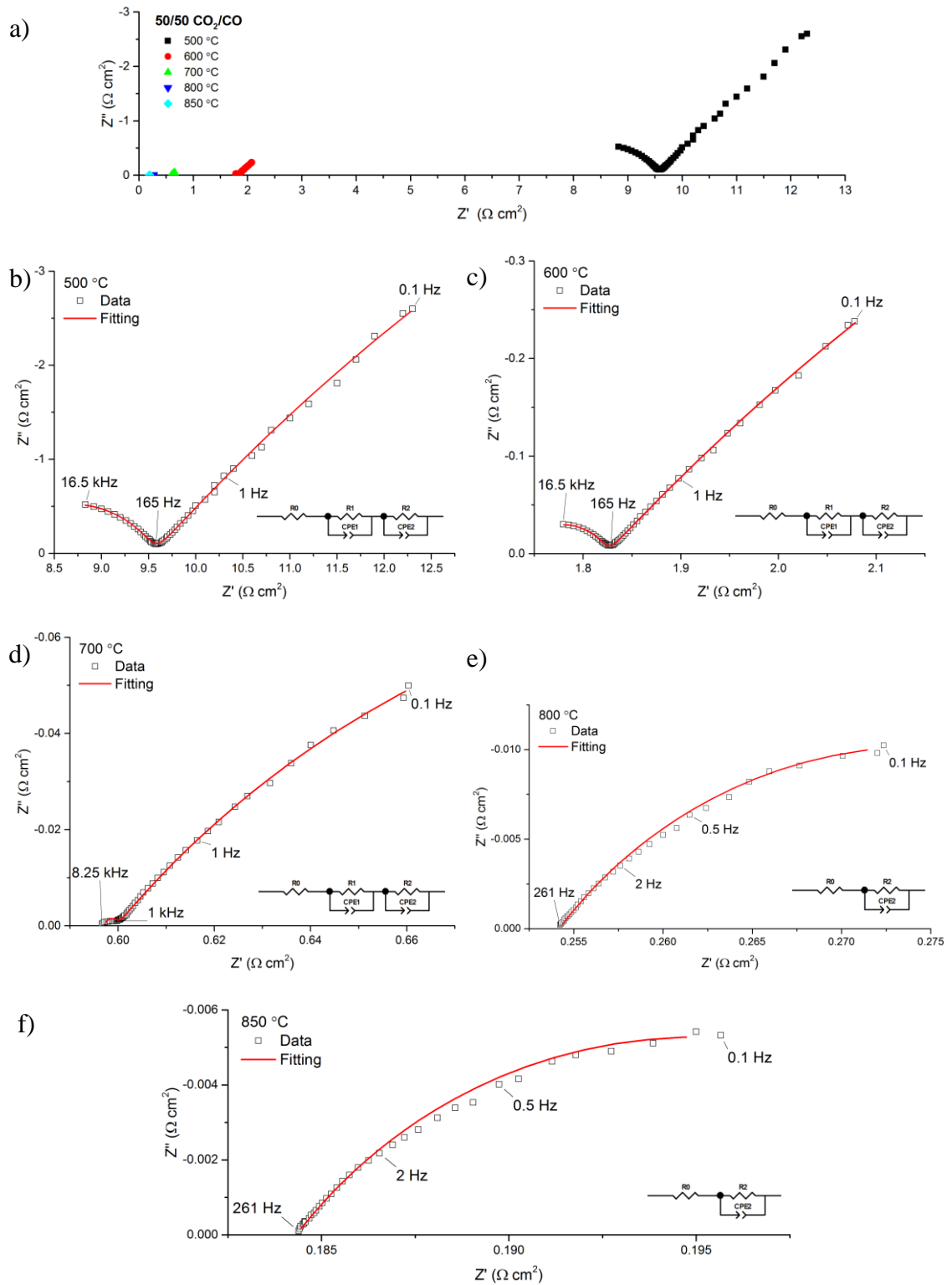


Figure 6-29. Impedance spectra of the CFO-SDC/CFO symmetrical cell tested in 50/50 CO_2/CO atmosphere in the temperature range 500–850 °C.

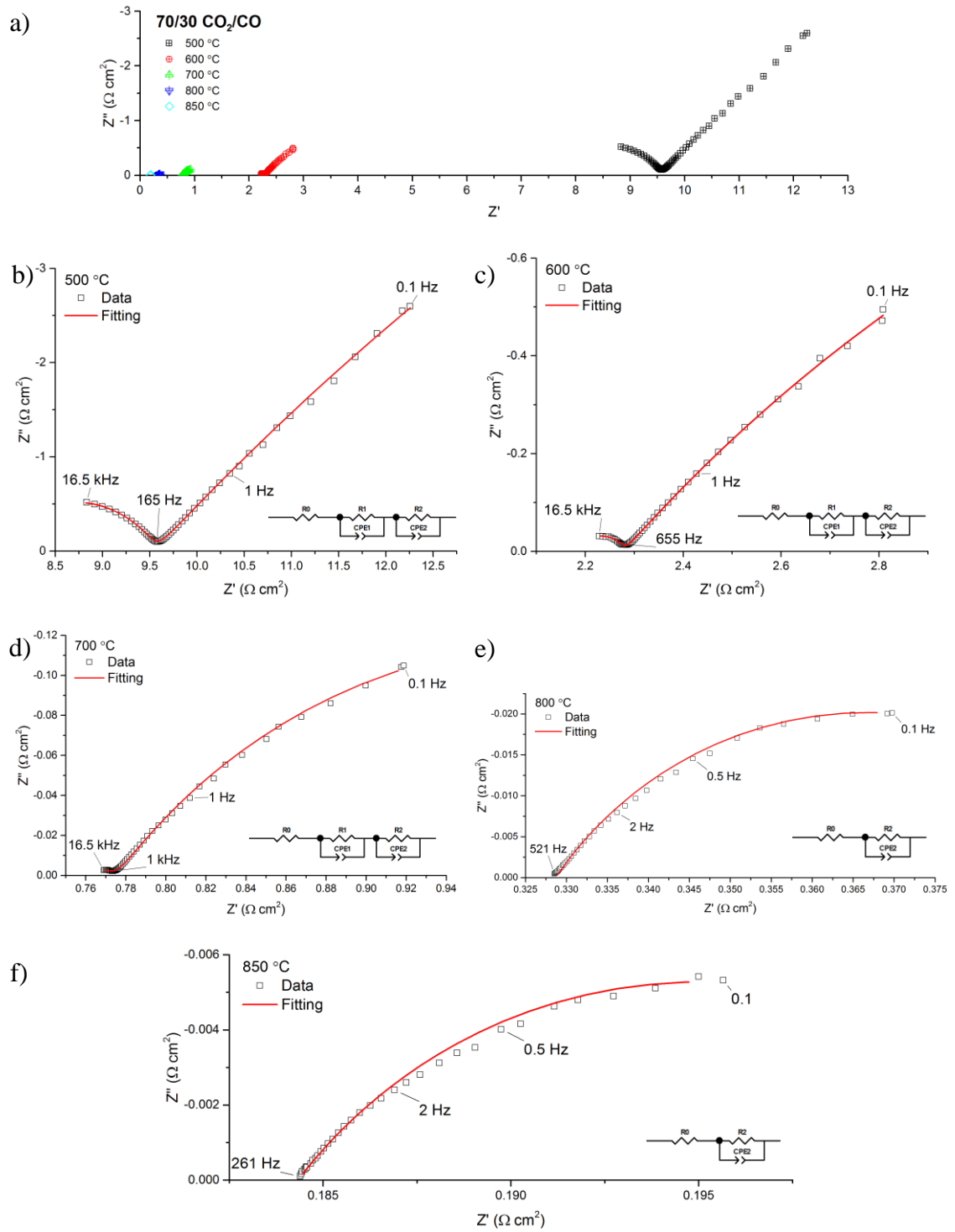


Figure 6-30. Impedance spectra of the CFO-SDC/CFO symmetrical cell tested in 50/50 CO_2/CO atmosphere in the temperature range 500–850 °C.

Table 6-6. Summary of the resistances obtained by fitting CFO-SDC|SDC|CFO-SDC EIS data with equivalent circuit models.

Temperature (°C)	R1 ($\Omega \text{ cm}^2$)		R2 ($\Omega \text{ cm}^2$)	
	50/50	35/15	50/50	35/15
500	1.802	1.834	25.572	54.894
600	0.098	0.102	3.499	4.256
700	-	0.016	0.268	0.521
800	-	-	0.045	0.082
850	-	-	0.023	0.041

Table 6-7. Summary of the capacitances obtained by fitting CFO-SDC|SDC|CFO-SDC EIS data with equivalent circuit models.

Temperature (°C)	C1 (F cm^2)		C2 (F cm^2)	
	50/50	35/15	50/50	35/15
500	5.35E-06	5.26E-06	-	-
600	9.84E-05	9.46E-05	-	-
700	-	5.61E-04	49.383	13.638
800	-	-	56.916	19.432
850	-	-	75.378	30.065

The estimated resistances (R2) of the low frequency arc were plotted on an Arrhenius plot to measure the activation energy. E_a values for gas compositions of 50/50 and 70/30 CO_2/CO were equal to 3.56 and 3.57 eV, respectively. Little variation in the low frequency arc's capacitance suggests that it may be associated with the gold current collector applied on top of the CFO-SDC electrode.

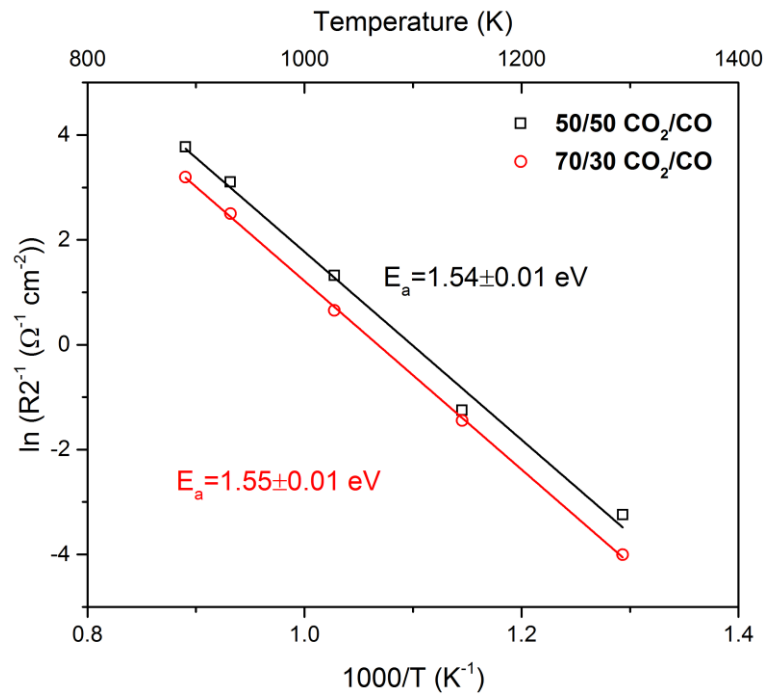


Figure 6-31. The Arrhenius plot of CFO-SDC|SDC symmetric cell in analysed in CO_2/CO atmospheres.

6.5 Summary

In this chapter, CoFe_2O_4 spinel materials were prepared by solid-state reaction in air and nitrogen atmospheres. Their fundamental properties of phase, microstructure and electronic conductivity were studied, and it was then tested as a MIEC electrode for solid oxide cell application. The results show that as the sintering temperature increases, the electronic conductivity of the samples increases. The materials exhibited n-type conductivity in both atmospheres, suggesting that conduction occurs through the hopping of electrons from Fe^{2+} to Fe^{3+} .

SEM micrographs showed the CFO pellets sintered in nitrogen to have larger grain sizes as well as increased density, compared to those sintered in air.

XRD results showed secondary phase formation in the samples at 1300 °C and above in N_2 . Using Rietveld refinement, the formed phase was identified as a rock salt of either Fe, Co or a combination of both; this was confirmed using Raman spectroscopy. Both XRD and XPS results suggest that Co^{2+} and Fe^{3+} occupy both O_h and T_d sites of CFO spinel and result in a random spinel structure.

The MIEC SOC electrodes were prepared by mixing CFO powder with an equal weight percentage of SDC nanoparticles. Although TGA results showed much a larger weight loss for SDC, both materials sintered together well. The powders were used to make a CFO-SDC compound that was deposited and sintered onto SDC electrolyte at 1300 °C in N_2 .

The samples sintered in N_2 showed high electronic conductivity and good electrochemical performance during CO_2 electrolysis and CO oxidation in a symmetrical cell, tested in the temperature range of 500 – 850 °C. With some structural tailoring and better dispersion with the ionic conductor, CFO is therefore a promising ceramic for SOC electrodes, offering mixed ionic-electronic conductivity via oxygen vacancies.

7 Conclusions and Future Work

7.1 Conclusions

As part of this thesis, an experimental rig capable of *operando* electrochemical measurements and Raman spectroscopy characterisation of the SOCs and can be used for characterisation of other ceramic materials. Ability to obtain structural and molecular information during the operation of the SOCs was the motivation for this work. The design constraints and material requirements, such as low temperature sealing, presented some challenges. The reactor was fully commissioned and tested for leak tightness and repeatability of the electrochemical data acquisition.

The data validity was tested against Kramers-Kronig relations and was found to be within 0.5% error region, meaning the data could be used for further analysis, such as DRT. Due to the length of the reactor being ca.50 cm the electrical leads had to be long, resulting in high inductance values in the high frequency region of the EIS spectrum. The inductance of the reactor was measured and compared to the values calculated by the DRTTools software. The data correction showed that the experimentally obtained values overcompensated the inductance, unlike the mathematically calculated values. The parasitic inductance affects the imaginary component of the EIS spectra, sometimes hiding an entire electrochemical processes occurring in the SOC form being measured.

The reactor was the first prototype built in the research group and the development of it was a continuous process throughout the years.

The reactor was then used to characterise in-house produced Ni-YSZ|YScSZ|LSM-YSZ|LSM button cells in CO₂/CO atmospheres at 700 °C using *operando* Raman spectroscopy. Negative bias was applied to the cell (CO₂ electrolysis mode) to study carbon deposition on the Ni-YSZ electrodes. Raman spectroscopy showed formation of carbon deposits on the surfaces of the fuel electrode likely as a result of decrease in the temperature of the electrode, shifting the Boudouard reaction equilibrium ($2\text{CO} \rightarrow \text{C} + \text{CO}_2$) to the region of carbon formation.

Post-mortem SEM analysis revealed different geometries of the carbon growths on the Ni-YSZ electrode, with some growing lengthwise. This could explain the initial increase of the carbon peaks' intensities that were stabilised in the first hour of operation. The majority of the carbon, however, was formed close to electrode/electrolyte interface, consistent with findings by Duboviks et al. (2015). The formed carbon nanofibers encapsulated the Ni particles. As expected, longer operation of the cell resulted in more carbon formation. The polarisation resistance of the EIS data, however, reduced after operation. The most likely cause for that for is the activation of the LSM oxygen electrode, however, some of the formed carbon fibres, if conductive, could potentially improve the interconnectivity of the Ni grains, thereby enhancing the electronic conductivity.

Further studies concentrated on development of an oxygen-deficient spinel (CFO) material to be used in a mixed ionic-electronic conductors for SOC electrode. The samples were sintered in two different environments – air and N₂. The dc conductivity measurements showed higher electronic conductivity for the samples sintered under reducing atmospheres. Overall, N₂-sintered samples showed higher sample weight loss during TGA analysis and did not pick up oxygen on cooling unlike samples sintered in air. The activation energies for 1300 °C samples were 0.25 and 0.17 eV for air and N₂, respectively. SEM images, showed less pores and higher grain size for the samples sintered in N₂, which was expected.

The CFO powder was then mixed with equal weight percent ration of SDC nanopowder and sintered to form MIEC pellets. The polished surface of the pellet was analysed with SEM-EDX and showed good distribution of the two materials. 1300 °C N₂ sintering conditions were chosen to make a symmetric SOCs to be tested in CO₂/CO atmospheres at 500 – 850 °C temperatures. The cell performed similarly in both electrolysis and fuel cell mode that would be beneficial for the reversible cell operation.

7.2 Future work

The research presented in this thesis laid the foundation for the future experimental work for development and improvement of SOCs electrodes. The following directions for future work are suggested:

- The results obtained and discussed in Chapter 5 showed limitations of the Raman spectroscopy technique to only detect the changes occurring on the surface of SOCs. To develop a further understanding the reaction mechanisms, particularly with novel materials and different fuels, patterned electrodes should be used for future investigations.
- Use high resolution infrared thermal imaging to monitor the temperature of the cell during the operation.
- *Operando* Raman experiments are limited to hours rather than days, so longer duration experiments could provide more information about cell deterioration and poisoning mechanisms.
- Reducing the length of the experimental apparatus to minimise the parasitic induction effects. For longer experimental durations, a water or coolant circulating microscope objective accessory should be designed and fitted.
- Neutron diffraction experiments are needed to understand the cation distribution and oxygen non-stoichiometry in CFO materials. Microstructural transformation (e.g. reducing CFO particle size) could yield higher conductivities and hence better conversion rates.
- Conduct trials using volume percentage for measuring CFO and SDC instead of weight percentage.

Studies have shown new, targeted phase formations to enhance grain bound in dual phase MIEC materials (such as $\text{Gd}_{0.374}\text{Ce}_{0.079}\text{Co}_{0.077}\text{Fe}_{0.47}\text{O}_x$ in CFO and $\text{Ce}_{0.8}\text{Gd}_{0.2}\text{O}_{2-\delta}$ (CGO) network (Lin et al., 2015, Harris et al., 2014). Transmission electron microscopy coupled with X-ray nanotomography imaging and computational modelling could be used for determining the 3D microstructures of the bulk phases and identifying emergent phase formation (Harris et al., 2014).

7.3 Dissemination

7.3.1 Conference Proceedings

- 1 MANEROVA, J., CALL, A. V., SINCLAIR, D. C. & ELDER, R. H. 2015. Methodology for Analysis of Solid Oxide Cells via Raman Spectroscopy. *ECS Transactions*, 68, 2083-2029.
- 2 CUMMING, D. J., TAYLOR, R., MANEROVA, J., SINCLAIR, D. C., HARDACRE, C. & ELDER, R. H. 2013. In-Situ Monitoring of Solid Oxide Electrolysis Cells. *ECS Transactions*, 58, 207-216.

7.3.2 Oral Presentations

- 1 MANEROVA, J., CALL, A. V., SINCLAIR, D. C. & ELDER, R. H. Methodology for Analysis of Solid Oxide Cells via Raman Spectroscopy. *ECS Conference on Electrochemical Energy Conversion & Storage with SOFC-XIV*, 26-31 July 2015, Glasgow, UK.
- 2 MANEROVA, J., CUMMING, D. J., SINCLAIR, D. C. & ELDER, R. H. In-Situ Raman Spectroscopy Probing of Solid Oxide Electrolysis Cells. *ECS and SMEQ Joint International Meeting*, 5-10 October 2014, Cancun, Mexico.

7.3.3 Poster Presentations

- 1 MANEROVA, J., REEPING, K. W., CALL, A. V., SINCLAIR, D. C., WALKER, R. A. & ELDER, R. H. In situ Raman Spectroscopy monitoring for Solid Oxide Cells. *Solid Oxide Electrolysis: Fuels and Feedstock from Water and Air: Faraday Discussion*, 16 July 2015, Sheffield, UK.
- 2 MANEROVA, J., REEPING, K. W., CALL, A. V., SINCLAIR, D. C., WALKER, R. A. & ELDER, R. H. In situ Raman Spectroscopy monitoring for Solid Oxide Cells. *Solid Oxide Electrolysis: Fuels and Feedstock from Water and Air: Faraday Discussion*, 13 - 15 July 2015, York, UK.
- 3 MANEROVA, J., CALL, A. V., SINCLAIR, D. C. & ELDER, R. H. In situ Raman Spectroscopic Characterisation of Solid Oxide Cells. *ChemEngDay UK*, 8-9th April 2015, Sheffield, UK.

- 4 MANEROVA, J., CUMMING, D. J., SINCLAIR, D. C. & ELDER, R. H. CeO₂-infiltrated LSM electrode for Solid Oxide Cells. *Supergen H₂FC Researchers Conference*, 15-17 December 2014, Birmingham, UK.
- 5 MANEROVA, J., CUMMING, D. J., SINCLAIR, D. C. & ELDER, R. H. Studies of Solid Oxide Electrolysis Cells using in-situ Raman Spectroscopy. *DTU Energy Conversion's 2nd International PhD Summer School – IMAGINE: Methods in Imaging of Energy Material Microstructure*, 25-29 August 2014, Risø, Denmark.
- 6 MANEROVA, J., CUMMING, D. J., SINCLAIR, D. C. & ELDER, R. H. In situ Raman Spectroscopy for Solid Oxide Electrolysis Cells. *ChemEngDay UK*, 7-8 April 2014, Manchester, UK.
- 7 MANEROVA, J., CUMMING, D. J., SINCLAIR, D. C. & ELDER, R. H. Carbon Dioxide Utilisation using Solid Oxide Electrolysis Cells. *Climate-KIC PhD Summer School: Carbon-free Frankfurt am Main by 2050*, 16-27 September 2013, Frankfurt am Main, Germany.

Awards

- 1 MANEROVA, J. STFC Futures/MDC Early Career Award (£2,000). Research visit to Montana State University. Awarded on 19th August 2014.
- 2 GÖLLNER-VÖLKER, L., MAZUR, C., GOLNAR, M., VAN DOREN, D. & MANEROVA, J. Climate-KIC PhD Summer School. Project 2013 Winner: Passive Mobility: A centrally coordinated mobility system for Frankfurt. *Climate-KIC PhD Summer School: Carbon-free Frankfurt am Main by 2050*, 16-27 September 2013, Frankfurt am Main, Germany.

Bibliography

<1330.full.pdf>.

- AGHAVNIAN, T., MOUSSY, J. B., STANESCU, D., BELKHOUE, R., JEDRECY, N., MAGNAN, H., OHRESSER, P., ARRIO, M. A., SAINCTAVIT, P. & BARBIER, A. 2015. Determination of the cation site distribution of the spinel in multiferroic CoFe₂O₄/BaTiO₃ layers by X-ray photoelectron spectroscopy. *Journal of Electron Spectroscopy and Related Phenomena*, 202, 16-21.
- AJROUDI, L., MLIKI, N., BESSAIS, L., MADIGOU, V., VILLAIN, S. & LEROUX, C. 2014. Magnetic, electric and thermal properties of cobalt ferrite nanoparticles. *Materials Research Bulletin*, 59, 49-58.
- ARESTA, M. 2010. Carbon Dioxide: Utilization Options to Reduce its Accumulation in the Atmosphere. *Carbon Dioxide as Chemical Feedstock*. Wiley-VCH Verlag GmbH & Co. KGaA.
- BBC. 2015. *UK government carbon capture £1bn grant dropped* [Online]. Available: <http://www.bbc.co.uk/news/uk-scotland-scotland-business-34357804>.
- BERNARD, S., BEYSSAC, O., BENZERARA, K., FINDLING, N., TZVETKOV, G. & BROWN, G. E. 2010. XANES, Raman and XRD study of anthracene-based cokes and saccharose-based chars submitted to high-temperature pyrolysis. *Carbon*, 48, 2506-2516.
- BINDOFF, N. L., STOTT, P. A., ACHUTARAO, K. M., ALLEN, M. R., GILLETT, N., GUTZLER, D., HANSINGO, K., HEGERL, G., HU, Y., JAIN, S., MOKHOV, I. I., OVERLAND, J., PERLWITZ, J., SEBBARI, R. & ZHANG, X. 2013. Detection and Attribution of Climate Change: from Global to Regional. In: STOCKER, T. F., QIN, D., PLATTNER, G.-K., TIGNOR, M., ALLEN, S. K., BOSCHUNG, J., NAUELS, A., XIA, Y., BEX, V. & MIDGLEY, P. M. (eds.) *Climate Change 2013: The Physical Science Basis. Contribution of Working Group I to the Fifth Assessment Report of the Intergovernmental Panel on Climate Change*. Cambridge, United Kingdom and New York, NY, USA: Cambridge University Press.
- BLINN, K. S., ABERNATHY, H., LI, X. X., LIU, M. F., BOTTOMLEY, L. A. & LIU, M. L. 2012. Raman spectroscopic monitoring of carbon deposition on hydrocarbon-fed solid oxide fuel cell anodes. *Energy & Environmental Science*, 5, 7913-7917.
- BOSTON, R., SCHMIDT, W. L., LEWIN, G. D., IYASARA, A. C., LU, Z., ZHANG, H., SINCLAIR, D. C. & REANEY, I. M. 2017. Protocols for the Fabrication, Characterization, and Optimization of n-Type Thermoelectric Ceramic Oxides. *Chemistry of Materials*, 29, 265-280.

- BOUKAMP, B. A. 1995. A Linear Kronig-Kramers Transform Test for Immittance Data Validation. *Journal of the Electrochemical Society*, 142, 1885-1894.
- BRIGHTMAN, E., MAHER, R., OFFER, G. J., DUBOVIKS, V., HECK, C., COHEN, L. F. & BRANDON, N. P. 2012a. Designing a miniaturised heated stage for in situ optical measurements of solid oxide fuel cell electrode surfaces, and probing the oxidation of solid oxide fuel cell anodes using in situ Raman spectroscopy. *Review of Scientific Instruments*, 83.
- BRIGHTMAN, E., MAHER, R., OFFER, G. J., DUBOVIKS, V., HECK, C., COHEN, L. F. & BRANDON, N. P. 2012b. Designing a miniaturised heated stage for in situ optical measurements of solid oxide fuel cell electrode surfaces, and probing the oxidation of solid oxide fuel cell anodes using in situ Raman spectroscopy. *Review of Scientific Instruments*, 83, 053707.
- BROOK, R. J. 1969. Pore-Grain Boundary Interactions and Grain Growth. *Journal of the American Ceramic Society*, 52, 56-57.
- BROWN, M., PRIMDAHL, S. & MOGENSEN, M. 2000. Structure/Performance Relations for Ni/Yttria-Stabilized Zirconia Anodes for Solid Oxide Fuel Cells. *Journal of The Electrochemical Society*, 147, 475-485.
- CHANDRAMOHAN, P., SRINIVASAN, M. P., VELMURUGAN, S. & NARASIMHAN, S. V. 2011. Cation distribution and particle size effect on Raman spectrum of CoFe₂O₄. *Journal of Solid State Chemistry*, 184, 89-96.
- CHEETHAM, A. K. & WILKINSON, A. P. 2003. Synchrotron X-ray and Neutron Diffraction Studies in Solid-State Chemistry. *Angewandte Chemie International Edition in English*, 31, 1557-1570.
- CHENG, Z., ABERNATHY, H. & LIU, M. L. 2007. Raman spectroscopy of nickel sulfide Ni₃S₂. *Journal of Physical Chemistry C*, 111, 17997-18000.
- CHENG, Z., WANG, J.-H., CHOI, Y., YANG, L., LIN, M. C. & LIU, M. 2011. From Ni-YSZ to sulfur-tolerant anode materials for SOFCs: electrochemical behavior, in situ characterization, modeling, and future perspectives. *Energy & Environmental Science*, 4, 4380-4409.
- CUMMING, D. J., TUMILSON, C., TAYLOR, S. F., CHANSAI, S., CALL, A. V., JACQUEMIN, J., HARDACRE, C. & ELDER, R. H. 2015. Development of a diffuse reflectance infrared Fourier transform spectroscopy (DRIFTS) cell for the in situ analysis of co-electrolysis in a solid oxide cell. *Faraday Discuss*, 182, 97-111.
- DAVIS, S. J., CALDEIRA, K. & MATTHEWS, H. D. 2010. Future CO₂ Emissions and Climate Change from Existing Energy Infrastructure. *Science*, 329, 1330-1333.
- DIARD, J.-P., LE GORREC, B. & MONTELLA, C. 2013. Electrical circuits containing CPEs. *Handbook of Electrochemical Impedance Spectroscopy*. Bio-Logic.
- DUBOVIKS, V., LOMBERG, M., MAHER, R. C., COHEN, L. F., BRANDON, N. P. & OFFER, G. J. 2015. Carbon deposition behaviour in metal-infiltrated gadolinia doped ceria electrodes for simulated biogas upgrading in solid oxide electrolysis cells. *Journal of Power Sources*, 293, 912-921.
- DUBOVIKS, V., MAHER, R. C., KISHIMOTO, M., COHEN, L. F., BRANDON, N. P. & OFFER, G. J. 2014. A Raman spectroscopic study of the carbon deposition mechanism on Ni/CGO electrodes during CO/CO₂ electrolysis. *Phys Chem Chem Phys*, 16, 13063-8.

- EDGAR. 2016. *CO2 time series 1990-2015 per region/country* [Online]. Available: <http://edgar.jrc.ec.europa.eu/overview.php?v=CO2ts1990-2015>.
- EIGENBRODT, B. C., POMFRET, M. B., STEINHURST, D. A., OWRUTSKY, J. C. & WALKER, R. A. 2011. Direct, In Situ Optical Studies of Ni-YSZ Anodes in Solid Oxide Fuel Cells Operating with Methanol and Methane. *Journal of Physical Chemistry C*, 115, 2895-2903.
- ELDER, R., CUMMING, D. & MOGENSEN, M. B. 2015. Chapter 11 - High Temperature Electrolysis A2 - Styring, Peter. In: QUADRELLI, E. A. & ARMSTRONG, K. (eds.) *Carbon Dioxide Utilisation*. Amsterdam: Elsevier.
- ELSEVIER 2016. Ceres, Cummins win DOE award for SOFC power in data centres. *Fuel Cells Bulletin*, 2016, 6.
- EPA. 2016. *Understanding Global Warming Potentials* [Online]. Online. Available: <https://www.epa.gov/ghgemissions/understanding-global-warming-potentials>.
- EUROPEAN COMMISSION. 2016. *International action on climate change: Climate negotiations (Paris Agreement)* [Online]. Available: https://ec.europa.eu/clima/policies/international/negotiations/paris_en.
- EUROPEAN EXPERT GROUP 2011. Future Transport Fuels.
- FACTSAGETM. 2010. *FToxid. Online database* [Online]. Available: http://www.crct.polymtl.ca/fact/documentation/FToxid/FToxid_Figs.htm [Accessed 19 Oct 2017].
- FARMER, G. T. & COOK, J. 2013. *Climate Change Science: A Modern Synthesis: Volume 1 - The Physical Climate*, Springer Netherlands.
- FERRARI, A. C. & ROBERTSON, J. 2000. Interpretation of Raman spectra of disordered and amorphous carbon. *Physical Review B*, 61, 14095-14107.
- FERRARO, J. R., NAKAMOTO, K. & BROWN, C. W. 2003. Chapter 1 - Basic Theory. *Introductory Raman Spectroscopy (Second Edition)*. San Diego: Academic Press.
- FIORILLO, F. & MAYERGOYZ, I. D. 2004. *Characterization and Measurement of Magnetic Materials*, Elsevier Science.
- FONSECA, F. C., DE FLORIO, D. Z., ESPOSITO, V., TRAVERSA, E., MUCCILLO, E. N. S. & MUCCILLO, R. 2006. Mixed Ionic–Electronic YSZ/Ni Composite for SOFC Anodes with High Electrical Conductivity. *Journal of The Electrochemical Society*, 153, A354.
- FREUND, H. J., GREUTER, F., HESKETT, D. & PLUMMER, E. W. 1983. Chemisorption of CO on Co(0001). II. Multielectron excitations. *Physical Review B*, 28, 1727-1733.
- FUELCELLMATERIALS.COM. 2007. *Hionic™ Electrolyte Supports* [Online]. Available: [http://www.fuelcellmarkets.com/content/images/articles/Hionic%205-21-2007\(2\).pdf](http://www.fuelcellmarkets.com/content/images/articles/Hionic%205-21-2007(2).pdf) [Accessed 11 Dec 2016].
- GALIZIA, P. 2017. *Production and morphological and microstructural characterization of bulk composites or thick films for the study of multiphysics interactions*. PhD thesis, Polytechnic University of Turin, Turin, Italy.
- GAMRY. 2015. *Basics of Electrochemical Impedance Spectroscopy* [Online]. Available: <https://www.gamry.com/application-notes/EIS/basics-of-electrochemical-impedance-spectroscopy/> [Accessed Nov 2017].

- GOMES, J. A., SOUSA, M. H., TOURINHO, F. A., MESTNIK-FILHO, J., ITRI, R. & DEPEYROT, J. 2005. Rietveld structure refinement of the cation distribution in ferrite fine particles studied by X-ray powder diffraction. *Journal of Magnetism and Magnetic Materials*, 184-187.
- GÓMEZ SANZ, S. 2014. *Exploiting carbon in enhancing the performance of catalytic materials*. Doctor of Philosophy, University of Cambridge.
- GORTE, R. J. & VOHS, J. M. 2003. Novel SOFC anodes for the direct electrochemical oxidation of hydrocarbons. *Journal of Catalysis*, 216, 477-486.
- GRAVES, C., EBBESEN, S. D., MOGENSEN, M. & LACKNER, K. S. 2011. Sustainable hydrocarbon fuels by recycling CO₂ and H₂O with renewable or nuclear energy. *Renewable and Sustainable Energy Reviews*, 15, 1-23.
- GUTIÉRREZ-LÓPEZ, J., MASÓ, N., LEVENFELD, B., VÁREZ, A., WEST ANTHONY, R. & BELIK, A. 2016. Electrical and Magnetic Properties of NiZn Ferrite Prepared by Conventional and Solar Sintering. *Journal of the American Ceramic Society*, 99, 2327-2333.
- HAIDER, M. A. & MCINTOSH, S. 2009. Evidence for Two Activation Mechanisms in LSM SOFC Cathodes. *Journal of The Electrochemical Society*, 156, B1369-B1375.
- HALL-SPENCER, J. M., RODOLFO-METALPA, R., MARTIN, S., RANSOME, E., FINE, M., TURNER, S. M., ROWLEY, S. J., TEDESCO, D. & BUIA, M.-C. 2008. Volcanic carbon dioxide vents show ecosystem effects of ocean acidification. *Nature*, 454, 96.
- HARRICK SCIENTIFIC PRODUCTS INC. 2012. *Raman High Temperature Reaction Chamber* [Online]. Available: <http://www.harricksci.com/ftir/accessories/group/Raman-High-Temperature-Reaction-Chamber>.
- HARRIS, W. M., BRINKMAN, K. S., LIN, Y., SU, D., COCCO, A. P., NAKAJO, A., DEGOSTIN, M. B., CHEN-WIEGART, Y.-C. K., WANG, J., CHEN, F., CHU, Y. S. & CHIU, W. K. S. 2014. Characterization of 3D interconnected microstructural network in mixed ionic and electronic conducting ceramic composites. *Nanoscale*, 6, 4480-4485.
- HONIG, J. 2012. *Preparation and Characterization of Materials*, Elsevier Science.
- HUANG, K. & GOODENOUGH, J. B. 2009. *Solid Oxide Fuel Cell Technology: Principles, Performance and Operations*, Woodhead Publishing.
- IRVINE, J. T. S., SINCLAIR, D. C. & WEST, A. R. 2004. Electroceramics: Characterization by Impedance Spectroscopy. *Advanced Materials*, 2, 132-138.
- IVANOV, V. G., ABRASHEV, M. V., ILIEV, M. N., GOSPODINOV, M. M., MEEN, J., AROYO, M. I. 2010. Short-range B -site ordering in the inverse spinel ferrite NiFe₂O₄. *Physical Review B*, 82, 024104.
- JIANG, S. P. 2007. Activation, microstructure, and polarization of solid oxide fuel cell cathodes. *Journal of Solid State Electrochemistry*, 11, 93-102.
- JIANG, S. P., ZHANG, J. P., APATEANU, L. & FOGER, K. 2000. Deposition of Chromium Species at Sr-Doped LaMnO₃ Electrodes in Solid Oxide Fuel Cells. I. Mechanism and Kinetics. *Journal of The Electrochemical Society*, 147, 4013-4022.

- JIANG, S. P., ZHANG, J. P. & ZHENG, X. G. 2002. A comparative investigation of chromium deposition at air electrodes of solid oxide fuel cells. *Journal of the European Ceramic Society*, 22, 361-373.
- JOO, J. H. & CHOI, G. M. 2008. Thick-film electrolyte (thickness <20 μ m)-supported solid oxide fuel cells. *Journal of Power Sources*, 180, 195-198.
- KAUR, G. 2015. *Solid Oxide Fuel Cell Components: Interfacial Compatibility of SOFC Glass Seals*, Springer International Publishing.
- KIRTLEY, J., SINGH, A., HALAT, D., OSWELL, T., HILL, J. M. & WALKER, R. A. 2013. In Situ Raman Studies of Carbon Removal from High Temperature Ni-YSZ Cermet Anodes by Gas Phase Reforming Agents. *Journal of Physical Chemistry C*, 117, 25908-25916.
- KIRTLEY, J. D., STEINHURST, D. A., OWRUTSKY, J. C., POMFRET, M. B. & WALKER, R. A. 2014. In situ optical studies of methane and simulated biogas oxidation on high temperature solid oxide fuel cell anodes. *Phys Chem Chem Phys*, 16, 227-36.
- KOUKETSU, Y., MIZUKAMI, T., MORI, H., ENDO, S., AOYA, M., HARA, H., NAKAMURA, D. & WALLIS, S. 2013. A new approach to develop the Raman carbonaceous material geothermometer for low-grade metamorphism using peak width. *Island Arc*, 23, 33-50.
- KUMAR, A., SHARMA, P. & VARSHNEY, D. 2014. Structural, vibrational and dielectric study of Ni doped spinel Co ferrites: $\text{Co}_{1-x}\text{Ni}_x\text{Fe}_2\text{O}_4$ ($x=0.0, 0.5, 1.0$). *Ceramics International*, 40, 12855-12860.
- KUMAR, S., MUNJAL, S. & KHARE, N. 2017. Metal-semiconductor transition and Seebeck inversion in CoFe_2O_4 nanoparticles. *Journal of Physics and Chemistry of Solids*, 105, 86-89.
- KURIAN, M., THANKACHAN, S., NAIR, D. S., E. K, A., BABU, A., THOMAS, A. & KRISHNA K. T, B. 2015. Structural, magnetic, and acidic properties of cobalt ferrite nanoparticles synthesised by wet chemical methods. *Journal of Advanced Ceramics*, 4, 199-205.
- LAGUNA-BERCERO, M. A., SANJUÁN, M. L. & MERINO, R. I. 2007. Raman spectroscopic study of cation disorder in poly- and single crystals of the nickel aluminate spinel. *Journal of Physics: Condensed Matter*, 19, 186217.
- LANDSBERG, G., MANDELSTAM, L. 1928. Eine neue Erscheinung bei der Lichtzerstreuung in Krystallen. *Naturwissenschaften*, 16, 557-558.
- LARSON, A. C. V. D., R. B. 2000. General Structure Analysis System (GSAS). Los Alamos National Laboratory, Report LAUR 86-748.
- LE TRONG, H., BUI, T. M. A., PRESMANES, L., BARNABÉ, A., PASQUET, I., BONNINGUE, C. & TAILHADES, P. 2015. Preparation of iron cobaltite thin films by RF magnetron sputtering. *Thin Solid Films*, 589, 292-297.
- LIN, Y., FANG, S. M., SU, D., BRINKMAN, K. S. & CHEN, F. L. 2015. Enhancing grain boundary ionic conductivity in mixed ionic-electronic conductors. *Nature Communications*, 6.
- LIU, B., ZHOU, K., LI, Z., ZHANG, D. & ZHANG, L. 2010. Microstructure and DC electrical conductivity of spinel nickel ferrite sintered in air and nitrogen atmospheres. *Materials Research Bulletin*, 45, 1668-1671.

- LIU, R.-R., TANIGUCHI, S., SHIRATORI, Y., ITO, K. & SASAKI, K. 2011. Influence of SO₂ on the Long-Term Durability of SOFC Cathodes. *ECS Transactions*, 35, 2255-2260.
- LU, K. 2014. *Materials in Energy Conversion, Harvesting, and Storage*, Wiley.
- MACKAY, R. A. & HENDERSON, W. 2017. *Introduction to Modern Inorganic Chemistry, 6th edition*, CRC Press.
- MAHER, R. C., BRIGHTMAN, E., HECK, C., OFFER, G. P., BRANDON, N. P. & COHEN, L. F. 2010. Monitoring Solid Oxide Fuel Cell Processes Using In-Situ Raman Spectroscopy. *XXII International Conference on Raman Spectroscopy*, 1267, 550-550.
- MAHER, R. C., DUBOVIKS, V., OFFER, G. J., KISHIMOTO, M., BRANDON, N. P. & COHEN, L. F. 2013. Raman Spectroscopy of Solid Oxide Fuel Cells: Technique Overview and Application to Carbon Deposition Analysis. *Fuel Cells*, 13, 455-469.
- MANEROVA, J., CALL, A. V., SINCLAIR, D. C. & ELDER, R. H. 2015. Methodology for Analysis of Solid Oxide Cells via Raman Spectroscopy. *ECS Trans.*, 68, 2083-2092.
- MANGALARAJA, R. V., ANANTHAKUMAR, S., MANOHAR, P. & GNANAM, F. D. 2002. Magnetic, electrical and dielectric behaviour of Ni_{0.8}Zn_{0.2}Fe₂O₄ prepared through flash combustion technique. *Journal of Magnetism and Magnetic Materials*, 253, 56-64.
- MCCREERY, R. L. 2005. *Raman Spectroscopy for Chemical Analysis*, Wiley.
- MELO, T. F. O., DA SILVA, S. W., SOLER, M. A. G., LIMA, E. C. D. & MORAIS, P. C. 2006. Investigation of surface passivation process on magnetic nanoparticles by Raman spectroscopy. *Surface Science*, 600, 3642-3645.
- METZGER, M. J., GLASSER, B. J., PATEL, B., FOX, J., SEMPUGA, B. C., HILDEBRANDT, D. & GLASSER, D. 2013. Liquid Fuels from Alternative Carbon Sources Minimizing Carbon Dioxide Emissions. *AIChE Journal*, 59, 2062-2078.
- NAGAI, M., IGUCHI, F., ONODERA, S., SATA, N., KAWADA, T. & YUGAMI, H. 2011. Evaluation of Stress Conditions in Operated Anode Supported Type Cells Based on In-Situ Raman Scattering Spectroscopy. *ECS Transactions*, 35, 519-525.
- NEELAKANTA, P. S. 1995. *Handbook of Electromagnetic Materials: Monolithic and Composite Versions and Their Applications*, Taylor & Francis.
- NEHRIR, M. & WANG, C. 2009. *Modeling and control of fuel cells : distributed generation applications*, Hoboken, N.J., Wiley.
- NETZSCH. n.d. *Simultaneous Determination of the Seebeck Coefficient and Electrical Conductivity – SBA 458 Nemesis®* [Online]. Available: <https://www.netzsch-thermal-analysis.com/en/products-solutions/seebeck-coefficient-electrical-conductivity/sba-458-nemesis/> [Accessed 22 Jan 2017].
- NEXCERIS LLC. 2015. *Hionic™ Substrate Safety Data Sheet* [Online]. Available: https://www.fuelcellmaterials.com/wp-content/uploads/2015/12/Hionic-US.SDS_.pdf [Accessed 11 Dec 2016].

- NOAAA. 2017. *Trends in Atmospheric Carbon Dioxide: Up-to-date weekly average CO₂ at Mauna Loa* [Online]. Online. Available: <https://www.esrl.noaa.gov/gmd/ccgg/trends/weekly.html>.
- ONODERA, S., NAGAI, M., IGUCHI, F., SATA, N., KAWADA, T. & YUGAMI, H. 2013. Evaluation of Stress Condition of Operated Anode Supported-Type SOFC under Operating Conditions Based on Raman Scattering Spectroscopy. *ECS Transactions*, 50, 83-88.
- ONUKE, S., ONODERA, S., IGUCHI, F., SHIMIZU, M., KAWADA, T. & YUGAMI, H. 2013. Evaluation of Stress Condition of Operated Anode Supported-Type SOFC under Operating Conditions Based on Raman Scattering Spectroscopy. *ECS Transactions*, 57, 951-957.
- PETKOV, V. & SHASTRI, S. D. 2010. Element-specific structure of materials with intrinsic disorder by high-energy resonant x-ray diffraction and differential atomic pair-distribution functions: A study of PtPd nanosized catalysts. *Physical Review B*, 81, 165428.
- POMFRET, M. B., MARDA, J., JACKSON, G. S., EICHHORN, B. W., DEAN, A. M. & WALKER, R. A. 2008a. Hydrocarbon fuels in solid oxide fuel cells: In situ Raman studies of graphite formation and oxidation. *Journal of Physical Chemistry C*, 112, 5232-5240.
- POMFRET, M. B., MARDA, J., JACKSON, G. S., EICHHORN, B. W., DEAN, A. M. & WALKER, R. A. 2008b. Hydrocarbon Fuels in Solid Oxide Fuel Cells: In Situ Raman Studies of Graphite Formation and Oxidation. *The Journal of Physical Chemistry C*, 112, 5232-5240.
- POMFRET, M. B., OWRUTSKY, J. C. & WALKER, R. A. 2006. High-temperature Raman spectroscopy of solid oxide fuel cell materials and processes. *Journal of Physical Chemistry B*, 110, 17305-17308.
- POMFRET, M. B., OWRUTSKY, J. C. & WALKER, R. A. 2010a. In Situ Optical Studies of Solid-Oxide Fuel Cells. *Annual Review of Analytical Chemistry*, Vol 3, 3, 151-174.
- POMFRET, M. B., OWRUTSKY, J. C. & WALKER, R. A. 2010b. In Situ Optical Studies of Solid-Oxide Fuel Cells. *Annual Review of Analytical Chemistry*, 3, 151-174.
- POMFRET, M. B., WALKER, R. A. & OWRUTSKY, J. C. 2012. High-Temperature Chemistry in Solid Oxide Fuel Cells: In Situ Optical Studies. *Journal of Physical Chemistry Letters*, 3, 3053-3064.
- PROSKURINA, N. V., CHEREPANOV, V. A., GOLYNETS, O. S. & VORONIN, V. I. 2004. Phase Equilibria and Structure of Solid Solutions in the La-Co-Fe-O System at 1100°C. *Inorganic Materials*, 40, 955-959.
- RAHAMAN, M. N. 2017. *Ceramic Processing and Sintering*, CRC Press.
- RAIKOVA, G., CARPANESE, P., Z., S., VLADIKOVA, D., VIVIANI, M. & BARBUCCI, A. 2009. Inductance correction in impedance studies of solid oxide fuel cells *Bulgarian Chem Comms*, 41, 199-206.
- RAMAN, C. V. & KRISHNAN, K. S. 1928. A New Type of Secondary Radiation. *Nature*, 121, 501.
- REICHENBÄCHER, M. & POPP, J. 2012. *Challenges in Molecular Structure Determination*, Springer Berlin Heidelberg.

- RIBEIRO, D. V., SOUZA, C. A. C. & ABRANTES, J. C. C. 2015. Use of Electrochemical Impedance Spectroscopy (EIS) to monitoring the corrosion of reinforced concrete. *Revista IBRACON de Estruturas e Materiais*, 8, 529-546.
- ROSSMEISL, J. & BESSLER, W. G. 2008. Trends in catalytic activity for SOFC anode materials. *Solid State Ionics*, 178, 1694-1700.
- SADEZKY, A., MUCKENHUBER, H., GROTHE, H., NIESSNER, R. & PÖSCHL, U. 2005. Raman microspectroscopy of soot and related carbonaceous materials: Spectral analysis and structural information. *Carbon*, 43, 1731-1742.
- SAHU, N. & PANIGRAHI, S. 2011. Mathematical aspects of Rietveld refinement and crystal structure studies on PbTiO₃ ceramics. *Bulletin of Materials Science*, 34, 1495-1500.
- SASAKI, S., FUJINO, K., TAK, EACUTE & UCHI, Y. 1979. X-Ray Determination of Electron-Density Distributions in Oxides, MgO, MnO, CoO, and NiO, and Atomic Scattering Factors of their Constituent Atoms. *Proceedings of the Japan Academy, Series B*, 55, 43-48.
- SCHMIDT, P. 2008. How to Get Ternary Solid Solutions Fe_{1-x}M'_xO (M = Co, Ni)? A Thermodynamic Concept. *European Journal of Inorganic Chemistry*, 2008, 2847-2855.
- SCHÖNLEBER, M. 2014. *Kramers-Kronig Validity Test Lin-KK for Impedance Spectra* [Online]. Available: <http://www.iwe.kit.edu/Lin-KK.php> [Accessed 16 Jan 2017].
- SCHONLEBER, M., KLOTZ, D. & IVERS-TIFFEE, E. 2014. A Method for Improving the Robustness of linear Kramers-Kronig Validity Tests. *Electrochimica Acta*, 131, 20-27.
- SEONG, H. J. & BOEHMAN, A. L. 2013. Evaluation of Raman Parameters Using Visible Raman Microscopy for Soot Oxidative Reactivity. *Energy & Fuels*, 27, 1613-1624.
- SERWAY, R. A. & VUILLE, C. 2011. *College Physics*, Cengage Learning.
- SHINDE, A. B. 2013. Structural and Electrical Properties of Cobalt Ferrite Nanoparticles *Int J Innov Technol Explor Eng*, 3, 64-67.
- SINGH, P., BANSAL, N. P., OHJI, T. & WERESZCZAK, A. 2009. *Advances in Solid Oxide Fuel Cells IV*, Wiley.
- SINGHAL, S. C. & KENDALL, K. 2003. Chapter 1 - Introduction to SOFCs. *High Temperature and Solid Oxide Fuel Cells*. Amsterdam: Elsevier Science.
- SKOLNICK, L. P., KONDO, S. & LAVINE, L. R. 1958. An Improved X-Ray Method for Determining Cation Distribution in Ferrites. *Journal of Applied Physics*, 29, 198-203.
- SMEKAL, A. 1923. Zur Quantentheorie der Dispersion. *Naturwissenschaften*, 11, 873-875.
- SMITH, D. K., FIALA, J. & RYBA, E. 2013. Book Reviews - The Rietveld Method, Young R. A., Editor, IUCr Monographs in Crystallography, 5, International Union of Crystallography, Oxford University Press, New York, NY, pp. 298. The Rietveld Method, Young R. A., Editor, Oxford University Press, Oxford, England 1993. ISBN 0198555776, x + 298 pp., 87 figures, 32 tables Metal & Alloys Indexes, International Centre for Diffraction Data, Swarthmore, PA, \$5.00. *Powder Diffraction*, 8, 252-254.

- SOLIDPOWER 2017. SOLIDpower SOFC units commissioned at Microsoft data centre. *Fuel Cells Bulletin*, 2017, 6.
- SOMIYA, S., ALDINGER, F., SPRIGGS, R. M., UCHINO, K., KOUMOTO, K. & KANENO, M. 2003. *Handbook of Advanced Ceramics: Materials, Applications, Processing and Properties*, Elsevier Science.
- STOLTEN, D. 2010. *Hydrogen and Fuel Cells: Fundamentals, Technologies and Applications*, John Wiley & Sons.
- STYRING, P., QUADRELLI, E. A. & ARMSTRONG, K. 2014. *Carbon Dioxide Utilisation: Closing the Carbon Cycle*, Elsevier Science.
- TAO, Y., EBBESEN, S. D. & MOGENSEN, M. B. 2014. Carbon Deposition in Solid Oxide Cells during Co-Electrolysis of H₂O and CO₂. *Journal of The Electrochemical Society*, 161, F337-F343.
- THANG, P. D., RIJNDERS, G. & BLANK, D. H. A. 2005. Spinel cobalt ferrite by complexometric synthesis. *Journal of Magnetism and Magnetic Materials*, 295, 251-256.
- THOMPSON, A. R., CALL, A. V., CUMMING, D. J., SINCLAIR, D. C. & ELDER, R. H. 2015. Electrochemical Impedance Spectroscopy Data from Solid Oxide Cells Undergoing Co-Electrolysis: The Influence of Rig Inductance. *ECS Trans.*, 68, 3417-3427.
- TOBY, B. 2001. EXPGUI, a graphical user interface for GSAS. *Journal of Applied Crystallography*, 34, 210-213.
- TULLER, H. L., LITZELMAN, S. J. & JUNG, W. 2009. Micro-ionics: next generation power sources. *Physical Chemistry Chemical Physics*, 11, 3023-3034.
- WACHSMAN, E. D., MARLOWE, C. A. & LEE, K. T. 2012. Role of solid oxide fuel cells in a balanced energy strategy. *Energy & Environmental Science*, 5, 5498-5509.
- WAN, T. H., SACCOCCIO, M., CHEN, C. & CIUCCI, F. 2015. Influence of the Discretization Methods on the Distribution of Relaxation Times Deconvolution: Implementing Radial Basis Functions with DRTtools. *Electrochimica Acta*, 184, 483-499.
- WANG, C. C., O'DONNELL, K., JIAN, L. & JIANG, S. P. 2015. Co-Deposition and Poisoning of Chromium and Sulfur Contaminants on La_{0.6}Sr_{0.4}Co_{0.2}Fe_{0.8}O_{3-δ} Cathodes of Solid Oxide Fuel Cells. *Journal of The Electrochemical Society*, 162, F507-F512.
- WEI, B., CHEN, K., ZHAO, L., LU, Z. & PING JIANG, S. 2015. Chromium deposition and poisoning at La_{0.6}Sr_{0.4}Co_{0.2}Fe_{0.8}O_{3-δ} oxygen electrodes of solid oxide electrolysis cells. *Physical Chemistry Chemical Physics*, 17, 1601-1609.
- WEST, A. R. 1987. *Solid State Chemistry and Its Applications*, Wiley.
- WHITE, W. B. & DEANGELIS, B. A. 1967. Interpretation of the vibrational spectra of spinels. *Spectrochimica Acta Part A: Molecular Spectroscopy*, 23, 985-995.
- WILL, J., MITTERDORFER, A., KLEINLOGEL, C., PEREDNIS, D. & GAUCKLER, L. J. 2000. Fabrication of thin electrolytes for second-generation solid oxide fuel cells. *Solid State Ionics*, 131, 79-96.

- XIANG, M., YE, L., PENG, C., ZHONG, L., BAI, H., SU, C. & GUO, J. 2014. Study on the electrochemical performance of high-cycle $\text{LiMg}_{0.08}\text{Mn}_{1.92}\text{O}_4$ cathode material prepared by a solid-state combustion synthesis. *Ceramics International*, 40, 10839-10845.
- YANG, H., XU, Z., FAN, M., GUPTA, R., SLIMANE, R. B., BLAND, A. E. & WRIGHT, I. 2008. Progress in carbon dioxide separation and capture: A review. *Journal of Environmental Sciences*, 20, 14-27.
- YAREMCHENKO, A. A., KHALYAVIN, D. D. & PATRAKEEV, M. V. 2017. Uncertainty of oxygen content in highly nonstoichiometric oxides from neutron diffraction data: example of perovskite-type $\text{Ba}_{0.5}\text{Sr}_{0.5}\text{Co}_{0.8}\text{Fe}_{0.2}\text{O}_{3-\delta}$. *Journal of Materials Chemistry A*, 5, 3456-3463.
- YU, C.-H., HUANG, C.-H. & TAN, C.-S. 2012. A Review of CO_2 Capture by Absorption and Adsorption. *Aerosol and Air Quality Research*, 12, 745-769.
- YUAN, X. Z., SONG, C., WANG, H. & ZHANG, J. 2009. *Electrochemical Impedance Spectroscopy in PEM Fuel Cells: Fundamentals and Applications*, Springer London.
- ZHA, S., CHENG, Z. & LIU, M. 2007. Sulfur Poisoning and Regeneration of Ni-Based Anodes in Solid Oxide Fuel Cells. *Journal of The Electrochemical Society*, 154, B201-B206.
- ZHOU, Z., ZHANG, Y., WANG, Z., WEI, W., TANG, W., SHI, J. & XIONG, R. 2008. Electronic structure studies of the spinel CoFe_2O_4 by X-ray photoelectron spectroscopy. *Applied Surface Science*, 254, 6972-6975.